

**REMAINING STRENGTH OF CORRODED GUSSET
PLATE CONNECTION IN STEEL TRUSS BRIDGE
AND ITS REPAIR USING CFRP SHEET**

(腐食した鋼トラス橋格点ガセット・プレートの残存耐荷力
と炭素繊維シートによる補修)

By

PHAM NGOC VINH

Supervisor

Assoc. Prof. **MIYASHITA TAKESHI**

A thesis submitted to the Department of Environmental and Civil Engineering
in partial fulfillment of the requirements for the degree of

Doctor of Engineering

Materials Science

Nagaoka University of Technology

Niigata, JAPAN

August, 2019

ABSTRACT

Numerous studies have shown that, in steel truss bridges, corrosion is frequently found on the gusset plates which connect members, particularly where the plate connects to the upper flange of the lower chord member. The corrosion of gusset plate connections has been confirmed to decrease load-carrying capacity, and it can lead to the collapse of an entire bridge. Besides, attachment of stiffening plate and member replacement are among the conventional methods often applied to repair corroded structures. However, these repair works lack efficacy because of the heavy machinery and welding facilities required. Therefore, a simpler and more effective repair method for the corroded gusset plate connection is urgently needed.

This study focuses on the following main objectives: 1) evaluating the remaining load-carrying capacity of the corroded gusset plate connection; 2) establishing a proper repair method for the corroded gusset plate connection; with main contents described as the following.

Firstly, laboratory loading tests and FEM analyses were conducted using approximately half-scale models of real bridges on two different forms of corrosion of a critical gusset plate: the corrosion loss of the lower chord flange-to-gusset weld and the corrosion loss of the gusset plate thickness. This study then implemented parametric FEM analyses of the effects of the degree of corrosion on the remaining load-carrying capacity of the gusset plate connection with the model of specimen and a full-scale model of an actual bridge. Additionally, based on the results of the parametric FEM analysis in the cases with the corrosion loss of the gusset plate thickness, an evaluation method for determining the local buckling strength of the corroded section was proposed.

Secondly, this study focused on investigating the effectiveness of repair method by using carbon fiber reinforced polymers (CFRP) for the corroded gusset plate connection. Loading tests were conducted with a model approximately 50% the size of an actual bridge and the degree of corrosion assumed to be approximately 50% of the gusset plate thickness. Further, the loading tests were carried out with three parameters of the repair method including the area of the bonded CFRP sheets, the direction ($\pm 45^\circ$, $\pm 56^\circ$, and 90°) of bonded CFRP sheets, and the location of bonded CFRP sheets (out-side bonding and both-sides bonding).

Thirdly, a nonlinear theoretical analysis method considering the peeling condition of CFRP sheets, and a nonlinear material condition of all members on the analytical model were established, for a steel plate bonding

a layer of CFRP sheet under uniaxial tensile loading. Moreover, after grasping the peeling mechanism of CFRP sheet from the proposed nonlinear theoretical analysis, FEM analyses were implemented on the repaired gusset plate connections to reproduce the obtained experimental results. Then, a parametric FEM analysis was carried out on the repaired connection by varying the number of bonding CFRP sheets, to clarify the appropriate number of CFRP sheets bonding into the corroded gusset plate.

Finally, this study proposed a design method to repair the corroded gusset plate connection, after the effectiveness of the repair method using CFRP sheets was investigated.

Key Words: Steel truss bridge, corroded gusset plate connection, FEA, remaining load-carrying capacity, repair method, CFRP sheets, design method, nonlinear theoretical analysis, FEA with CFRP sheets.

ACKNOWLEDGMENTS

This Ph.D. work had been, for me, a process of fruitful researching and learning. It would not have reached completion without the support of the people whom I thank below.

I am very fortunate to be advised by two outstanding Ph.D. supervisors. I owe profound gratitude to my supervisors, Associate Professor MIYASHITA Takeshi and Professor OHGAKI Kazuo for their academic backgrounds, critical minds, thoughtful guidance and insightful feedback throughout the years of my study.

I am vastly indebted to my primary supervisor, Associate Professor MIYASHITA Takeshi, of the Department of Environmental and Civil Engineering, Nagaoka University of Technology, whose ideas of research, academic advice, and support throughout this Ph.D. have aided me tremendously. I have learnt and developed immensely under his guidance. Without his assistance, this thesis would not have been possible. Equally, and no less important in any means, is my secondary supervisor, Professor OHGAKI Kazuo, of Institute of Technologists, whose care, attention and encouragement have helped me through all phases of this dissertation. He is an inspirational academic and visionary leader. I am thankful they have been with me from the start and have given me the confidence to finish the Ph.D. journey.

I acknowledge Nippon Expressway Research Institute Cooperation and Nippon Steel & Sumikin Material Cooperation as the research institutions and the participants, for their valuable insights and research funding, which are the hallmark of the thesis.

I would also like to express my heartfelt thanks to the academic supervisor committee, Professor IWASAKI Eiji, Professor TAKAHASHI Osamu, Professor SHIMOMURA Takumi, of Department of Environmental and Civil Engineering, together with my two Ph.D. supervisors, who participated in my mid-term and final dissertation defense for their generous time and trust. I truly treasured their advice and recommendation that made my thesis more thoroughly enhanced.

My sincere thanks go to Steel Structural Laboratory, Nagaoka University of Technology, for providing me with a friendly and professional research environment. I would also like to thank the administrators, teachers, and colleagues at both Nagaoka University of Technology, Japan and The University of Technology and Science, University of Da Nang, Vietnam for their cooperation and help during my Ph.D. journey. I would like to thank all the University Staff for the kindness and moral support they offered.

I am really grateful for the Japanese Government with Monbukagakusho, MEXT Scholarship fully sponsoring me with grants for my three-year PhD study in Japan.

Last but not least, I deeply thank my wife, Nguyen Thi Thanh Thuy, for her mind of science as a fellow Ph.D. student, along with me at Nagaoka University of Technology, and her continued understanding and patience, which in many ways, play a vital role in my research's progress. I particularly thank my twin brother, Pham Ngoc Quang, and his family for being with me throughout the years. I wish to express my appreciation to my parents, my parents-in-law and family members for encouraging me to pursue this Ph.D. study. I would like to dedicate this work to them for their unflinching love during the hard times and as always.

Sincerely, **PHAM NGOC VINH**

TABLE OF CONTENTS

ABSTRACT	i
ACKNOWLEDGEMENTS	iii
TABLE OF CONTENTS	iv
LIST OF FIGURES	vii
LIST OF TABLES	x
1. INTRODUCTION	1
1.1. Background and purposes	1
1.2. Objectives of study	3
1.3. Thesis outline	4
References	6
2. EVALUATION OF REMAINING LOAD-CARRYING CAPACITY OF CORRODED GUSSET PLATE CONNECTION	10
2.1. Introduction	10
2.2. Experimental overview	12
2.2.1. Specimen shape	12
2.2.2. Experimental parameters	13
2.2.3. Measured items	13
a) Strain gauge location	13
b) Displacement measurement	13
c) Loading method	14
2.3. Finite element analysis overview	15
2.3.1. Analysis model	16
2.3.2. Material and initial imperfection	17
a) Steel	17
b) Initial imperfection (Initial deflection and residual stress)	17
2.3.3. Analysis parameters	19
2.4. Analysis results and discussion	20
2.4.1. Intact model (Specimen N)	20
a) Influence of initial imperfection on maximum load	20
b) Load-vertical displacement relationship	22
c) Failure conditions	22
2.4.2. Corroded models (Specimens W, S, and L)	23
a) Load-vertical displacement relationship	23
b) Failure condition	24
2.5. Parametric analysis	27
2.5.1. Analysis parameters	28
2.5.2. Results of parametric analyses	29
a) Load and vertical displacement relationship	29
b) Remaining load-carrying capacity	29
c) Failure condition	30
2.5.3. Remaining load-carrying capacity under the full-scale model of a real bridge	34
2.6. Evaluation equation for local buckling strength	36
2.6.1. Proposed evaluation equation	36
2.6.2. Calculated result and discussion	38
2.7. Conclusion	40

References	43
3. EXPERIMENTAL STUDY ON REPAIR METHOD USING CFRP SHEETS	44
3.1. Introduction	44
3.2. Experimental overview	46
3.2.1. Specimen shape	46
3.2.2. Properties of the materials	46
a) Steel and CFRP sheet	46
b) Putty and resin	46
3.2.3. Experimental parameters	47
3.2.4. Determining the number of CFRP sheets	49
3.2.5. Process bonding CFRP sheets	51
3.2.6. Measured items	52
a) Strain gauge location	52
b) Displacement measurement	53
3.2.7. Loading method	53
3.3. Results and discussion	53
3.3.1. Improved effectiveness for maximum load	53
3.3.2. Improved effectiveness for deformation	56
a) Load and vertical displacement relation	56
b) Load and out-of-plane deformation relation	57
3.3.3. Improved effectiveness for eccentricity moment on the corroded section	57
3.3.4. Failure condition	58
3.4. Conclusion	62
Appendix: Calculating strength of gusset plate connection (AASHTO)	64
References	66
4. FINITE ELEMENT ANALYSIS OF GUSSET PLATE CONNECTION BONDING CFRP SHEETS	69
4.1. Introduction	69
4.2. Theoretical analysis	70
4.2.1. Differential equation	70
a) Analytical object	70
b) Modeling	71
c) Relationship between stress and strain	71
d) Differential equation	72
4.2.2. Calculation process	74
4.2.3. Example and discussion	92
a) Calculated model	92
b) Finite element analysis	92
c) Calculated results of proposed method	93
4.3. Finite element analysis	96
4.3.1. Analysis model	96
4.3.2. Material	97
4.3.3. Analysis results and discussion	101
4.4. Parametric analysis	102
4.5. Conclusion	103
References	105

5.	DESIGN METHOD FOR CORRODED GUSSET PLATE CONNECTION	108
5.1.	Introduction	108
5.2.	Design method	109
5.2.1.	Used materials	109
a)	Carbon fiber reinforced polymers (CFRP) sheet	109
b)	Primer	110
c)	Smoothing agent	110
d)	Impregnation adhesive resin	110
e)	Primer for highly expansive elastic putty	111
f)	Highly expansive elastic putty	111
5.2.2.	Design method	111
5.3.	Conclusion	112
	References	113
6.	CONCLUSION AND FURTHER RESEARCH	115
6.1.	Conclusion	115
6.2.	Further research	119
	LIST OF PUBLICATIONS	120

LIST OF FIGURES

Figure 1.1 Classification of the age of existing steel truss bridges in the world.	2
Figure 1.2 Frequently corroded locations on steel truss bridges.	2
Figure 2.1 Frequently corroded locations on steel truss bridges.	10
Figure 2.2 Specimen geometry.	11
Figure 2.3 Loading frame.	11
Figure 2.4 The specimens prior to the loading tests.	11
Figure 2.5 Measured items in the truss frame.	14
Figure 2.6 Measured items in the link frame.	14
Figure 2.7 Strain gauge locations in the gusset plate.	14
Figure 2.8 Loading test condition.	15
Figure 2.9 Finite element analysis model.	15
Figure 2.10 Initial deflection of the gusset plate .	18
Figure 2.11 Residual stress distribution.	18
Figure 2.12 Load-displacement relationship, subject to initial deflections of the gusset plate (Specimen N).	18
Figure 2.13 Contour drawing of the out-of-plane deformation of the Specimen N intact series (at maximum load).	19
Figure 2.14 Load-displacement relationship, subject to residual stress on the gusset plate connection (Specimen N).	21
Figure 2.15 Load-vertical displacement relationship, subject to the actual plate thickness (Specimen N).	21
Figure 2.16 Load-bending strain relationship (Specimen N).	21
Figure 2.17 Out-of-plane deformation of plate area underneath diagonal member (N).	21
Figure 2.18 Analytical contours of out-of-plane deformation and physical deformation of Specimen N (at maximum load).	22
Figure 2.19 Load-vertical displacement relationship (W, S, and L).	26
Figure 2.20 Maximum load between FEA and EXP.	26
Figure 2.21 Load-bending strain relationship (W).	26
Figure 2.22 Out-of-plane deformation in plate region underneath diagonal member (W).	26
Figure 2.23 Load-bending strain relationship of Specimen S.	26
Figure 2.24 Load-bending strain relation (S).	27
Figure 2.25 Out-of-plane deformation in plate region underneath diagonal member (S).	27

Figure 2.26 Analytical contours of out-of-plane deformation and physical deformation of the gusset plate (at maximum load).	27
Figure 2.27 Load-displacement relationship as the cross-sectional loss parameter is varied.	31
Figure 2.28 Load-displacement relationship as the flange-to-gusset weld loss parameter is varied.	32
Figure 2.29 Relationship between corrosion loss and remaining load-carrying capacity.	32
Figure 2.30 Analysis contours of out-of-plane deformation as the cross-sectional loss is varied (at maximum load).	33
Figure 2.31 Analysis contours of out-of-plane deformation as the length of the flange-to-gusset weld loss is varied (at maximum load).	34
Figure 2.32 Remaining load-carrying capacity curve, normalized to the horizontal shear yield strength of the intact gusset plate.	35
Figure 2.33 Local buckling underneath the compressive diagonal.	39
Figure 2.34 Flowchart of process for calculating the local buckling strength.	39
Figure 2.35 Calculated (CAL), analytical (FEM), and experimental (EXP) local buckling strengths.	40
Figure 2.36 Standard buckling strength curve.	40
Figure 2.37 Changed point of failure condition of the corroded section.	40
Figure 3.1 Specimen shape.	45
Figure 3.2 The specimens before loading test.	48
Figure 3.3 The CFRP bonding methods on the corroded gusset plate.	48
Figure 3.4 Process bonding CFRP sheets.	49
Figure 3.5 Measured items in the link frame.	49
Figure 3.6 Strain gauge locations in the gusset plate.	49
Figure 3.7 Load-Vertical displacement relation.	55
Figure 3.8 Load-Out-of-plane deformation relation.	56
Figure 3.9 Load-Strain relation on the inner surface of the Groove section in the diagonal direction.	59
Figure 3.10 Final shape of the specimens.	60
Figure 3.11 Load-bending strain relation at the plate area underneath the diagonal member.	61
Figure 3.12 Load-bending strain relationship of Specimen S.	61
Figure 3.13 Load-Von Mises stress on CFRP sheet.	62
Figure 3.14 Limit state of the gusset plate connection.	64
Figure 4.1 Analytical object (Steel plate bonding a layer of CFRP).	70
Figure 4.2 Modeling (1/4 model).	70

Figure 4.3 Constitutive models of materials.	70
Figure 4.4 The peeling mechanism of CFRP sheet.	73
Figure 4.5 Flowchart of calculation process.	73
Figure 4.6 Stress constitution in Case 1.	76
Figure 4.7 Stress constitution in Case 2.	77
Figure 4.8 Stress constitution in Case 3.	79
Figure 4.9 Stress constitution in Case 4.	80
Figure 4.10 Stress constitution in Case 5.	82
Figure 4.11 Stress constitution in Case 6.	85
Figure 4.12 Stress constitution in Case 7.	88
Figure 4.13 Calculated model of example.	90
Figure 4.14 Finite element analysis model of steel plate bonding a CFRP sheet.	90
Figure 4.15 Load –relative displacement relationship.	90
Figure 4.16 Comparison of stress distribution between FEA and CAL.	91
Figure 4.17 Finite element analysis model of corroded gusset plate connection bonding CFRP sheets.	94
Figure 4.18 Element types used for simulation.	94
Figure 4.19 Constitutive model of material for interface element (Polyurea putty layer).	95
Figure 4.20 Load-Vertical displacement relationship.	98
Figure 4.21 Analytical contours of out-of-plane deformation and physical deformation of the corroded gusset plate connection bonding CFRP sheets.	99
Figure 4.22 Maximum load-the number of bonding CFRP sheets relationship.	101
Figure 5.1 Design method for corroded gusset plate connection.	111

LIST OF TABLES

Table 2.1 Experimental parameters.	11
Table 2.2 Analysis parameters.	18
Table 2.3 Parametric analysis parameters for cross-sectional corrosion loss cases.	28
Table 2.4 Parametric analysis parameters for flange-to-gusset weld loss cases.	28
Table 2.5 Parametric analysis parameters for cross-sectional corrosion loss cases under the full scale model of a real bridge.	35
Table 2.6 Calculating the local buckling strength of the three component columns of the gusset.	39
Table 2.7 Calculating the local buckling strength of the plate region underneath the compressive diagonal member.	39
Table 3.1 Properties of CFRP sheet and steel.	45
Table 3.2 Properties of putty and resin.	45
Table 3.3 Experimental parameters.	45
Table 3.4 Maximum load and improvement rate.	55
Table 3.5 Strength of gusset plate connections (AASHTO).	55
Table 3.6 Summary of failure conditions on the gusset plate.	61
Table 3.7 Calculating the strength of the gusset plate connection (AASHTO).	65
Table 4.1 Cases implemented in calculated program.	73
Table 4.2 Material properties of steel, CFRP sheet, and adhesion layer.	90
Table 4.3 Element types and material types used for simulation.	95
Table 4.4 Material properties of steel, and adhesion layer for simulation.	95
Table 4.5 Material properties (orthotropic) of CFRP sheet for simulation.	95
Table 5.1 Material properties of CFRP sheets.	108
Table 5.2 Primer quality standards.	108
Table 5.3 Smoothing agent quality standard.	109
Table 5.4 Impregnation adhesive resin.	109
Table 5.5 Primer for highly expansive elastic putty.	109
Table 5.6 Highly expansive elastic putty.	109

CHAPTER 1

INTRODUCTION

1.1. BACKGROUND AND PURPOSES

The truss bridge is a popular type of bridges which primarily consists of a truss system with main members connected by gusset plates. The truss structure has been widely used nowadays; mainly because it is light in weight with large load-carrying capacity, and it owns a high in-plane-stiffness. Steel truss bridges have been applied early in the developed history of modern bridges worldwide as their efficient use of materials enabled lower construction costs. In the world, compared to the application of steel truss bridges to railroad / railway systems, the one applied to highway systems was generally not as early, quick, or crucial. According to statistics from International Database for Civil and Structural Engineering (IDCSE)^{1,1)}, most of steel truss bridges in the world were built in North America (46%). Plus, the growth of truss bridge amount focused on the period 1890s and 1940s. This is understood that the first period (1890s) coincides with the development of railway networks in North America and Europe, whereas the second period (1940s) is closely linked to the introduction of welding technology for steel bridge construction. Further, the existing steel truss bridges are classified according to construction time as shown in **Fig. 1.1**^{1,1)}. When looking at **Fig. 1.1**, it can be seen that the existing steel truss bridges are considered extremely “old”, the ranges of ages are between 50 to over 100 years, most of which were built in the period before 1950 (65.71%), and from 1950 to 1970 (13.78%). Moreover, numerous 100-year-old truss bridges remain in service today^{1,2), 1,3)}, and the number of over 50 - year- old steel truss bridges are predicted to increase significantly in the coming years.

With such a considerable increase in old steel truss bridges, severe damage due to corrosion has become a serious problem. Many reports and researches have indicated that potential corrosion locations in steel truss bridges are frequently found on the gusset plate which connects main members of the steel truss bridge. The gusset plate connections of a truss bridge are considered to be a structurally critical component of the truss bridge system because they connect all main members. It has been clarified that the reduction in the load-carrying capacity of a corroded gusset plate connection can lead to the collapse of the entire truss bridge.

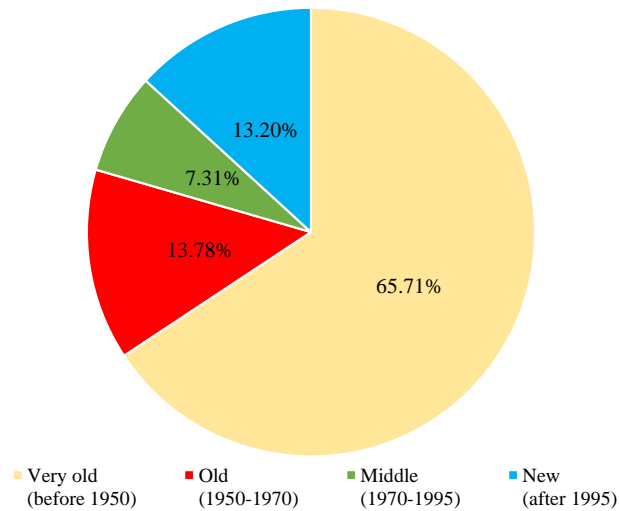


Fig. 1.1 Classification of the age of existing steel truss bridges in the world^{1.1)}.



Fig. 1.2 Frequently corroded locations on steel truss bridges.

A typical example of this problem occurred in the USA in 2007, when the I-35W steel truss bridge^{1.4)-1.6)} collapsed because of insufficient gusset plate thickness, resulting in a connection having a lower load-carrying capacity than necessary. In addition to this example, the Choshi truss bridge in Japan, which crossed the Tone River to connect between Chiba prefecture and Ibaraki prefecture, was dismantled completely in 2009 after nearly 50 years of service^{1.7), 1.8)}. This was because of a serious level of the corrosion damage found at its gusset plate connections, lower chord members, and diagonal members; even though several of Choshi truss bridge's members were reinforced and replaced during its service life. From 2009 to 2012, a research cooperated by three main members of Tokyo Metropolitan University, Waseda University, and Public Works Research Institute (PWRI) in Japan was implemented to investigate the remaining load-carrying capacity of the corroded gusset plate connections, which were cut out from the aforementioned Choshi truss bridge^{1.7), 1.8)}. As a result, with an average-corroded-thickness of 23% pitting damage distributing evenly over the surface of its gusset plate, by using the loading test and FEM analysis, it was confirmed that the gusset plate connection reduced significantly in the load-carrying capacity by 25%^{1.7), 1.8)}. However, statistics inspected on real steel truss

bridges indicated that corrosion is frequently found on the locations connecting the gusset plate to the upper flange of the lower chord member under the fatal forms (see **Fig. 1.2**) rather than the forms of evenly-distributing corrosion. This fatal corrosion is simply because of the complex shape in this region, which readily accumulate debris and water. Therefore, evaluation of the effects of corrosion on the remaining load-carrying capacity of the gusset plate connection, with the corrosion location being between the gusset plate and the upper flange of the lower chord member, has become a critical subject of research.

1.2. OBJECTIVES OF STUDY

In this study, laboratory loading tests and FEM analyses were conducted using an approximately half-scale models of real bridges on two different forms of corrosion of a critical gusset plate: the corrosion loss of the welded connection between the gusset plate and the upper flange of the lower chord member in the compressive direction, and the corrosion loss of the gusset plate thickness. Both of the loading tests and the FEM analyses were carried out with the objectives of determining the deformation performance, failure behaviors, and the reduction rate in load-carrying capacity of the corroded gusset plate connection. Besides, this study conducted parametric analyses of the effects of the size of the corroded sections on the gusset plate using FEM, in order to determine the relationship between remaining capacity and the extent of dimensional reduction due to corrosion. Additionally, based on the results of the parametric FEM analysis of the cases with the corrosion loss of the gusset plate thickness, an evaluation method for determining the local buckling strength of the corroded section was proposed.

On the other hand, the applicability of carbon fiber reinforced polymers (CFRP) as a material for repairing and strengthening aging or damaged structures is being intensively investigated worldwide, such as in the USA from the 1970s^{1.9)} and Japan and China from the 1980s^{1.10)}. CFRP in sheet form is usually applied to repair and strengthen steel structures which reduce load-carrying capacity due to natural hazards, human errors, accidents, corrosion damages, and fatigue damage. Furthermore, CFRP sheet is also used to improve structures with reduced load-carrying capacity due to changing of the purposes of the structure utility. However, the application of CFRP sheet to steel structures for corrosion and fatigue factors gains the most in popularity. Numerous studies have already verified the effectiveness of using CFRP sheet to reinforce the corroded members; consisting of the members subjected to the axial stress such as the chord members of truss bridge and the lower flange of I-girder of steel bridges^{1.11)-1.13)}, and the members subjected to the reaction force

(compressive stress) such as the vertical stiffener at the supports of I-girder steel bridges^{1.11), 1.14)-1.16)}. In addition, recovering from the shear buckling strength of the corroded web in steel girder bridges by using CFRP sheet was also investigated^{1.11), 1.17), 1.18)}. However, to the best of our knowledge, up to date, there have been not any cases in which CFRP sheets are applied to the corroded gusset plate connections.

Therefore, in order to establish a proper repair method for the corroded gusset plate connection, this study proposed the CFRP-sheet-based repair methods after investigating the effectiveness of using CFRP sheets as a repair material for the corroded gusset plate connections.

1.3. THESIS OUTLINE

This study focuses on the following main objectives: 1) evaluating the remaining load-carrying capacity of the corroded gusset plate connection; 2) establishing a proper repair method for the corroded gusset plate connection; with six chapters described as the following.

Chapter 1 is the introduction which contains background knowledge, motivation, and objectives of this study. A comprehensive review of literature and a description of the scopes and method were expressed in this chapter.

Chapter 2 is the conduction of laboratory loading tests and FEM analyses by using an approximately half-scale models of actual bridges on two different forms of corrosion of a critical gusset plate: the corrosion loss of the welded connection between the gusset plate and the upper flange of the lower chord member in the compressive direction, and the corrosion loss of the gusset plate thickness. Both of the loading tests and the FEM analyses were carried out with the objective of determining the deformation performance, failure behaviors, and the reduction rate in load-carrying capacity of the corroded gusset plate connection. This chapter then implemented parametric FEM analyses of the effect of the degree of corrosion on the remaining load-carrying capacity of the gusset plate connection with the model of specimen and the full-scale model of an actual bridge. Additionally, based on the results of the parametric FEM analysis of the cases with the corrosion loss of the gusset plate thickness, an evaluation method for determining the local buckling strength of the corroded section was proposed.

Chapter 3 is the focus on investigating the effectiveness of repair method by using carbon fiber reinforced polymers (CFRP) for the corroded gusset plate connection. Loading tests were conducted with a model of approximately 50% the size of an actual bridge and the degree of corrosion assumed to be approximately 50%

of the gusset plate thickness. Further, the loading tests were carried out with three parameters of the repair method including the area of the bonded CFRP sheets, the direction ($\pm 45^\circ$, $\pm 56^\circ$, and 90°) of the bonded CFRP sheets, and the location of the bonded CFRP sheets (out-side bonding and both-sides bonding).

Chapter 4 is the establishment of a nonlinear theoretical analysis method considering the peeling condition of CFRP sheet, and the nonlinear material condition of all member on the analytical model; for a steel plate bonding a layer of CFRP sheet under uniaxial tensile loading. Moreover, after grasping the peeling mechanism of CFRP sheet from the proposed nonlinear theoretical analysis, finite element analyses were implemented on the repaired gusset plate connection to reproduce the experimental results obtained in Chapter 3. Finally, a parametric analysis was carried out on the repaired gusset plate connection by varying the number of bonding CFRP sheets calculated from the equation of steel conversion, to clarify the necessary number of CFRP sheets bonding into the corroded gusset plate.

Chapter 5 is the proposal of the design method to repair the corroded gusset plate connection, after the effectiveness of the repair method using CFRP sheets were investigated by conducting loading tests and FEM analysis in Chapter 3 and 4.

Chapter 6 is an overall summary of the obtained results and proposed further research needed.

REFERENCES

- 1.1) Janberg, N.: International Database for Civil and Structural Engineering, <https://structurae.net/structures/bridges-and-viaducts/truss-bridges>, 1998-2018. (Accessed on September 2016)
- 1.2) Lichtenstein, A. G.: Inspection and rehabilitation of steel truss for highway bridges, In: *Bridge Management, Inspection, Maintenance, Assessment and Repair* (reference book), Springer US, USA, pp. 695-704, 1990.
- 1.3) Lima, K., Robson, N., Oosterhof, S., Kanji, S., DiBattista, J. and Montgomery, C. J.: Rehabilitation of a 100-year-old steel truss bridge, *CSCE 2008 Annual Conference*, Canada, pp. 1-11, 2008.
- 1.4) National Transportation Safety Board: Collapse of I-35W highway bridge Minneapolis, Minnesota, Accident report, NTSB/HAR-08/03, PB2008-916203, August 2007.
- 1.5) Hatano, H., Murakami, S., Rokugou, Y. and Yoda, T.: Summary of NTSB report on I-35W bridge in Minneapolis, *Bridge and Foundation*, pp. 37-42, 2010.
- 1.6) Kasano, H. and Yoda, T.: Collapse mechanism and evaluation of node damages of I-35W Bridge, Minneapolis, USA, *Proceedings of Japan Civil Engineering Association-A*, Vol. 66, No. 2, pp. 312-323, 2010 (in Japanese).
- 1.7) Cooperative research report of PWRI (June 2013). "Evaluation method of load-carrying capacity of bridge members with corrosion damage", No. 456, (in Japanese).
- 1.8) Cooperative research report of PWRI (January 2012). "FEM analysis of corroded gusset plate connection in steel truss bridge", No. 429, (in Japanese).
- 1.9) ACI-440, 2008: Guide for the design and construction of externally bonded FRP systems for strengthening concrete structures, *American Concrete Institute*.
- 1.10) FRP in China: The state of FRP research, design guidelines and application in construction, *FRP Composites in Civil Engineering – CICE 2004*.
- 1.11) Nippon Expressway Research Institute: Repair and reinforcement method for corroded steel members by using CFRP sheet, October 2013 (in Japanese).
- 1.12) Nagai, M., Hidekuma, Y., Miyashita, T., Okuyama, Y., Kudo, A. and Kobayashi, A.: Bonding characteristics and flexural stiffening effect of CFRP strand sheets bonded to steel beams, *Procedia*

Engineering, Vol. 40, pp. 137–142, 2012.

- 1.13) Hidekuma, Y., Miyashita, T., Okuyama, Y., Ishikawa, T. and Kobayashi, A.: Repairing method for steel member with cross-section loss by CFRP bonding, *IABSE Symposium Report*, Vol. 104, No. 12, pp. 1-5, 2015.
- 1.14) Wakabayashi, D., Miyashita, T., Okuyama, Y., Nagai, M., Koide, N., Kobayashi, A., Hidekuma, Y. and Horimoto, W.: Experimental study on repair and reinforcement method for web in steel girder bridge using FRP, *the 9th Symposium on Research and Application of Hybrid Structures*, pp. 371-378, 2011 (in Japanese).
- 1.15) Miyashita, T. and Nagai, M.: Repair method for corroded steel girder ends using CFRP sheet, *IABSE-JSCE Joint Conference on Advances in Bridge Engineering-III*, 21-22 August, 2015, Dhaka, Bangladesh.
- 1.16) Okuyama, Y., Miyashita, T., Wakabayashi, D., Hidekuma, Y., Kobayashi, A., Koide, N., Horimoto, W. and Nagai, M.: A study on optimum design method of repair and reinforcement method using carbon fiber sheets for corroded web in steel girder bridge, *Proceedings of Structural Engineering*, Vol. 60A, pp. 541–553, March 2014 (in Japanese).
- 1.17) Wakabayashi, D., Miyashita, T., Okuyama, Y., Kobayashi, A. and Hidekuma, Y.: Repair method using CFRP for corroded steel girder ends, *Fourth Asia-Pacific Conference on FRP in Structures (APFIS 2013)*, pp.1-6, 11-13 December 2013.
- 1.18) Miyashita, T., Wakabayashi, D., Hidekuma, Y., Kobayashi, A., Okuyama, Y., Koide, N., Horimoto, W. and Nagai, M.: CFRP repair method for corroded steel girder ends, *IABSE Symposium Report*, Vol. 104, No. 12, pp. 1-7, August 2015.
- 1.19) Miyashita, T., Nagai M.: Stress analysis for steel plate with multilayered CFRP under uni-axial loading, *Journal of JSCE*, Vol. 66, No. 2, pp.378-392, June 2010 (in Japanese).
- 1.20) Okuyama, Y., Miyashita, T., Ogata, T., Fujino, K., Ohgaki, K., Hidekuma, Y., Horimoto, W., Nagai, M.: Uniaxial compression test of steel plate bonded FRP sheet for rational repair and reinforcement of web in steel girder bridge, *Journal of Structural Engineering*, Vol. 57A, pp. 735-746, March 2011 (in Japanese).
- 1.21) Okuyama, Y., Miyashita, T., Wakabayashi, D., Koide, N., Kobayashi, A., Hidekuma, Y., Horimoto, W.,

- and Nagai, M.: Shear buckling test and prediction of shear load carrying capacity for steel girder bonded CFRP on its web, *Journal of JSCE*, Vol. 68, No. 3, pp. 635-654, 2012 (in Japanese).
- 1.22) Ishikawa, T., and Miyashita, T.: High-precision solution of steel plate strengthened with CFRP plates under uniaxial loading, *Journal of JSCE*, Vol. 69, No. 1, pp. 89-100, 2013 (in Japanese).
- 1.23) Ishikawa, T., and Miyashita, T.: Step design for CFRP bonded onto steel plate under uni-axial load, *Journal of JSCE*, Vol. 67, No. 2, pp. 351-359, 2011 (in Japanese).
- 1.24) Miyashita, T., Hidekuma, Y., Kobayashi, A., Okuyama, Y., Kudo, A., and Nagai, M.: Tensile test of steel plate bonded CFRP strand sheet with joint, *Journal of JSCE*, Vol. 69, No. 2, pp. 257-274, 2013 (in Japanese).
- 1.25) Okuyama, Y., Miyashita, T., Wakabayashi, D., Koide, N., Hidekuma, Y., Horimoto, W., Nagai, M.: Experimental study on repair method using CFRP for corroded web in steel girder bridge, *Journal of Structural Engineering*, Vol. 58A, pp. 710-720, 2012 (in Japanese).
- 1.26) Okuyama, Y., Miyashita, T., Wakabayashi, D., Koide, N., Hidekuma, Y., Horimoto, W., Nagai, M.: A study on optimum design method of repair and reinforcement method using carbon fiber sheets for corroded web in steel girder bridge, *Journal of Structural Engineering*, Vol. 60A, pp. 541-553, 2014 (in Japanese).
- 1.27) Okuyama, Y., Miyashita, T., Ogata, T., Fujino, K., Ohgaki, K., Hidekuma, Y., Horimoto, W., Nagai, M.: Uniaxial compression test of steel plate bonded FRP sheet for rational repair and reinforcement of web in steel girder bridge, *Journal of Structural Engineering*, Vol. 57A, pp. 735-746, 2011 (in Japanese).
- 1.28) Miyashita, T., Wakabayashi, D., Hidekuma, Y., Kobayashi, A., Koide, N., Horimoto, W., Nagai, M.: Repair for axial member in steel bridge by bonding CFRP sheet through high-elongation and low elastic putty, *Journal of JSCE*, Vol. 71, No. 5, pp. 23-38, 2015 (in Japanese).
- 1.29) Wakabayashi, D., Miyashita, T., Okuyama, Y., Hidekuma, Y., Kobayashi, A., Koide, N., Horimoto, W., Nagai, M.: Repair method for steel girder by bonding carbon fiber sheet using high elongation elastic butty, *Journal of JSCE*, Vol. 71, No. 1, pp. 44-63, 2015 (in Japanese).
- 1.30) Miyashita, T., Ishikawa, T.: Stress analysis for steel member multilayered CFRP plates under bending, *Journal of JSCE*, Vol. 69, No. 1, pp. 26-39, 2013 (in Japanese).

- 1.31) Liu, C., Miyashita, T, Nagai, M.: Analytical study on shear capacity of steel I-girder with local corrosion nearby girder ends, *Journal of Structural Engineering*, Vol. 57A, pp. 715-723, 2011 (in Japanese).

CHAPTER 2

EVALUATION OF REMAINING LOAD-CARRYING CAPACITY OF CORRODED GUSSET PLATE CONNECTION

2.1. INTRODUCTION

Recently, numerous instances of severe corrosion damage to the gusset plate connections of steel truss bridges have been widely reported across the world, as shown in **Fig. 2.1**. The corrosion of gusset plate connections has been confirmed to decrease load-carrying capacity, and it can lead to the collapse of the entire bridge. In Chapter 2, the remaining load-carrying capacity of a corroded gusset plate connection was evaluated using load testing and finite element method (FEM) analysis. Two different types of gusset plate corrosion were investigated: the corrosion loss of the lower chord flange-to-gusset weld and the corrosion loss of the gusset plate thickness. The loading tests and FEM analyses were conducted on an approximately half-scale model of a real bridge. Corrosion effects were evaluated for an assumed disconnection of 50% of the weld length, and for the loss of 50% and 75% of the gusset plate thickness in a selected region. This chapter then implemented parametric FEM analyses of the effect of the degree of corrosion on the remaining load-carrying capacity of the gusset plate connection with the model of specimen and the full-scale model of an actual bridge. Finally, based on the results of the parametric FEM analysis in cases with corrosion loss of the gusset plate thickness, a method for evaluating the local buckling strength of the corroded section was proposed.



Fig. 2.1 Frequently corroded locations on steel truss bridges.

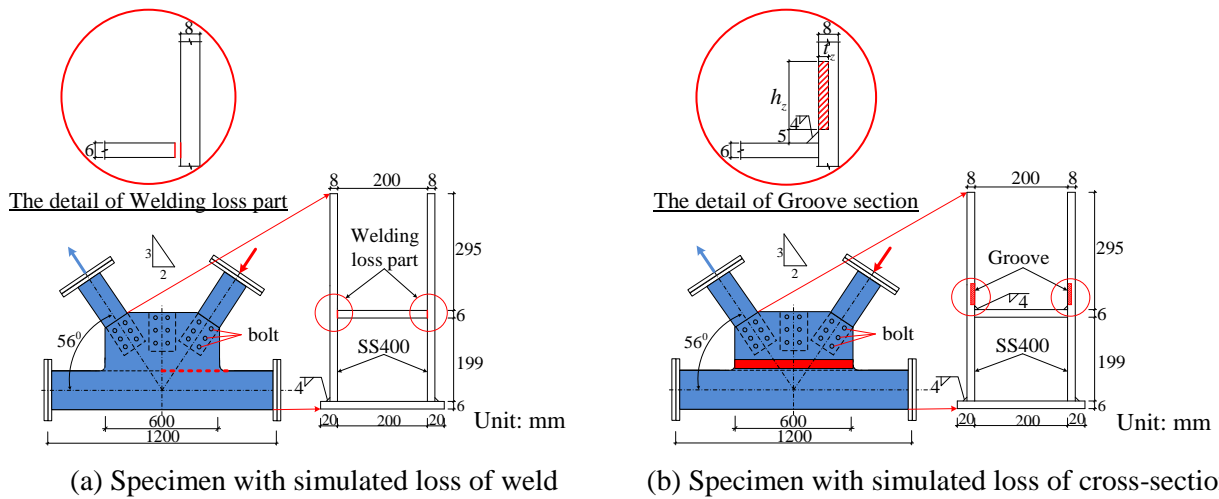


Fig. 2.2 Specimen geometry.

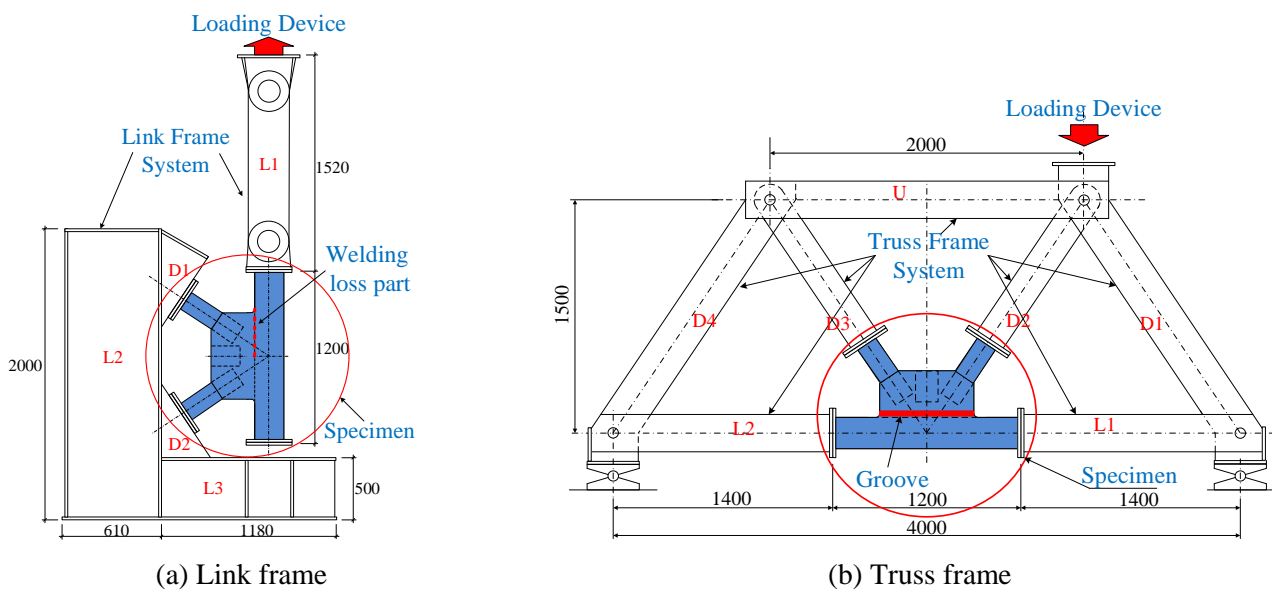


Fig. 2.3 Loading frame.

Table 2.1 Experimental parameters.

No.	Specimen	Corrosion level	Dimension of Groove section		Test frame
			h_z (mm)	t_z (mm)	
1	N	Without corrosion	–	–	Link frame
2	W	Welding corrosion	–	–	Link frame
3	S	Small cross-sectional corrosion	25	4	Link frame
4	L	Large cross-sectional corrosion	50	6	Truss frame

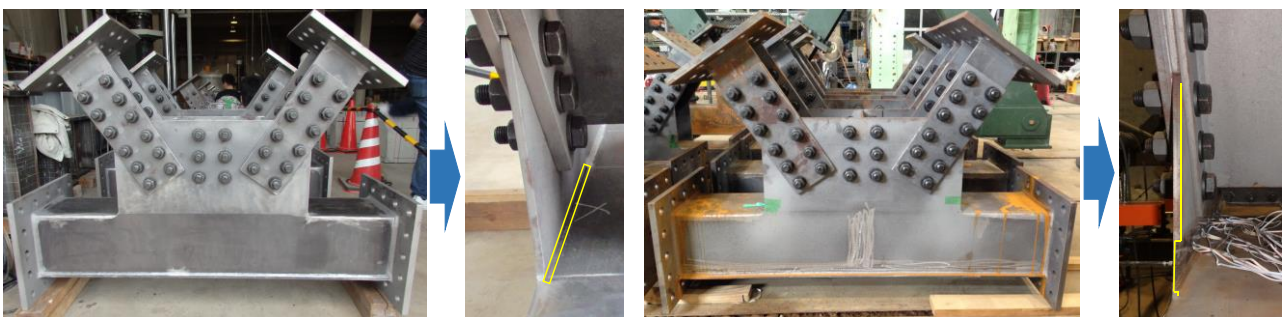


Fig. 2.4 The specimens prior to the loading tests.

2.2. EXPERIMENTAL OVERVIEW

2.2.1. Specimen shape

The gusset plate specimens used in this study were monolithic with the chord members: the projected web plates of the lower chord members were projected to serve as the gusset plates. The dimensions of all members in the models were approximately 50% the size of those on the subject bridges (the S-truss-bridge (1974), the N-truss-bridge (1980), the T-truss-bridge (1983), and the K-truss-bridge (1985) in JAPAN used bolted-connections), which were chosen because of the severe corrosion damage found on their gusset plate connections. The length, width, and thickness of the model gusset plate connection were 1200 mm, 216 mm, and 8 mm, respectively, as shown in **Fig. 2.2**. The angle between the lower chord member and the two diagonal members connecting into the gusset plate was 56 degrees. Further, because the axial force of the diagonal members was much larger than that of the vertical member in the subject bridges and the existing bridges, the influence of the vertical members was omitted in the specimens. The loss of the weld between the flange plate and the gusset due to corrosion was represented by introducing a disconnection between the gusset plate and the upper flange of the lower chord member in the compressive direction (see **Fig. 2.2(a)**). The corrosion loss of the gusset plate thickness was represented as a cross-sectional loss by cutting a groove (called the “Groove”) of height h_z and width t_z at the location where the gusset plate connected to the upper flange of the lower chord member (see **Fig. 2.2(b)**). The base metal used in this study was SS400 steel with a yield stress of 317 MPa and an elastic modulus of 200 GPa, determined from the mill sheet certificate and the tensile experiments of the SS400 steel in the laboratory.

Because of the limited capacity of the experimental equipment (only 3000 kN), the loading tests were conducted using two frames: a truss frame system and a link frame system with the size of the specimen used 50% that of the actual bridges, as shown in **Fig. 2.3**. The dimensions of the members of the two frames were designed such that they would operate within their elastic phase during the loading test process. The length and height of the truss frame was 4000 mm and 1500 mm, respectively, and 1790 mm and 2000 mm, respectively, for the link frame. The frame loading system was connected to the specimen using high-tension bolts through the connecting plates.

2.2.2. Experimental parameters

The experimental parameters used in this study are shown in **Table 2.1**. With the basic aim of determining the deformation performance, failure behavior, and load-carrying capacity of the gusset plate connection, a loading test was first conducted on the connection without any simulated corrosion loss. Because the excessive loss of section in the welded connection in the compressive direction of the gusset plate could lead to large out-of-plane deformation, a loading test was then conducted on a specimen with one-half of the flange-to-gusset weld removed, as shown in **Fig. 2.4(a)**. To account for the failure behavior of corroded gusset plate thickness, approximately 50% and 75% of the gusset plate thickness was assumed to be corroded (see **Fig. 2.4(b)**) in two additional specimens. The 50% and 75% corrosion levels were simulated by introducing a Groove in the gusset plate of $h_z = 25$ mm and $t_z = 4$ mm, and $h_z = 50$ mm and $t_z = 6$ mm, respectively.

In total, four specimens were tested: one control with no simulated corrosion loss (Specimen N), one simulating the loss of the flange-to-gusset weld (Specimen W), and specimens simulating small and large cross-sectional corrosion (Samples S and L).

2.2.3. Measured items

a) Strain gauge location

The locations of the strain gauges are shown in **Figs. 2.5, 2.6, and 2.7**. Four single-element strain gauges were attached to the cross-section of each member of the truss frame and the link frame, in order to consider the effects of the two-axis bending moment and the axial force on them. Moreover, in order to determine the principal stress components on the cross-sectional loss part and the border line between the gusset plate and the lower chord; three-element $0^\circ/45^\circ/90^\circ$ Rosette Stacked strain gauges were employed, as shown in **Fig. 2.7**. In the corroded cases, the strain gauges were attached to the inside and outside of the cross-sectional loss part. In addition, three-element $0^\circ/45^\circ/90^\circ$ Rosette Stacked strain gauges were also used at the plate area underneath the compressive diagonal member, to grasp the buckling behavior, and single-element strain gauges were used for the other locations.

b) Displacement measurement

In each loading step, vertical and horizontal displacements were measured on the members of the truss frame and the link frame, and the bottom surface of gusset plate connection, as shown in **Fig. 2.5** and **Fig. 2.6**. In addition, the out-of-plane displacement of the gusset plate was also measured at the two outside surfaces of

the gusset plate connection. These positions were labeled 7-1~7-6, as shown in **Fig. 2.5** and **Fig. 2.6**.

c) Loading method

The loading tests were conducted in the laboratory using the link frame system for the intact Specimen N, the welding loss Specimen W, and the small cross-sectional loss Specimen S; and using the truss frame system for the large cross-sectional loss Specimen L.

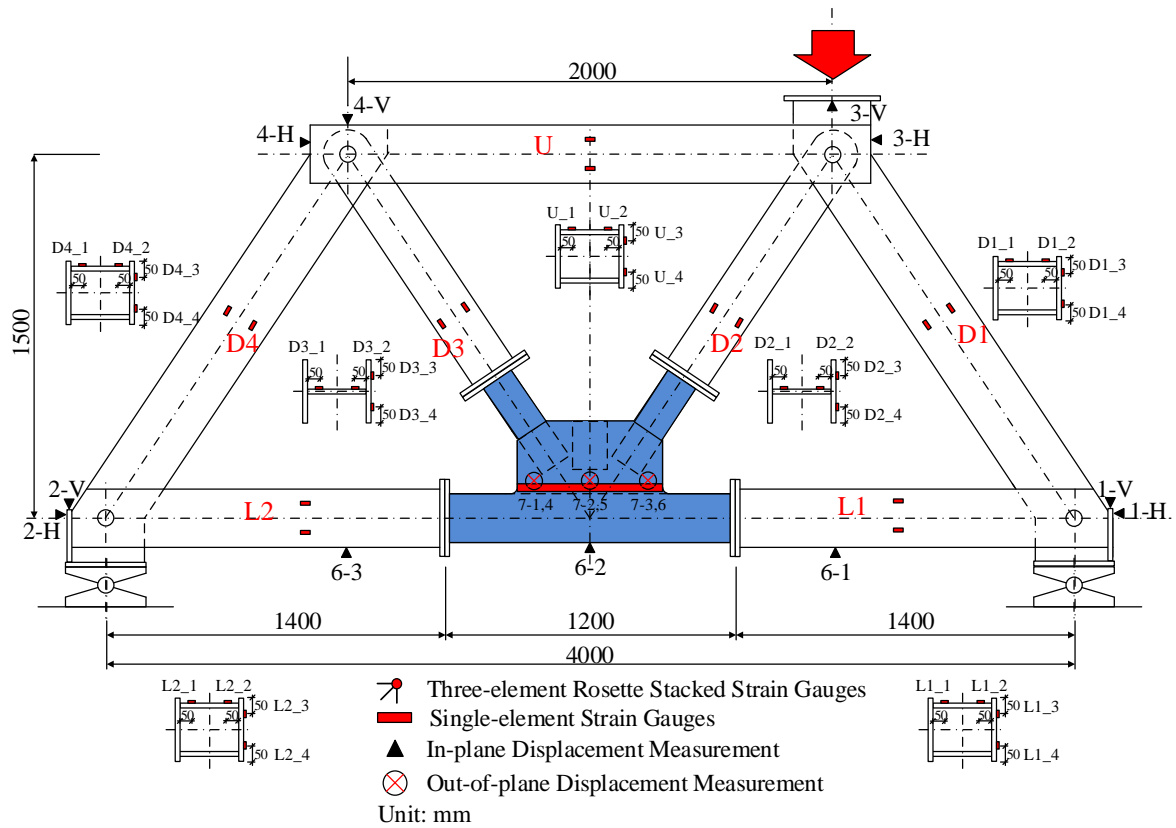


Fig. 2.5 Measured items in the truss frame.

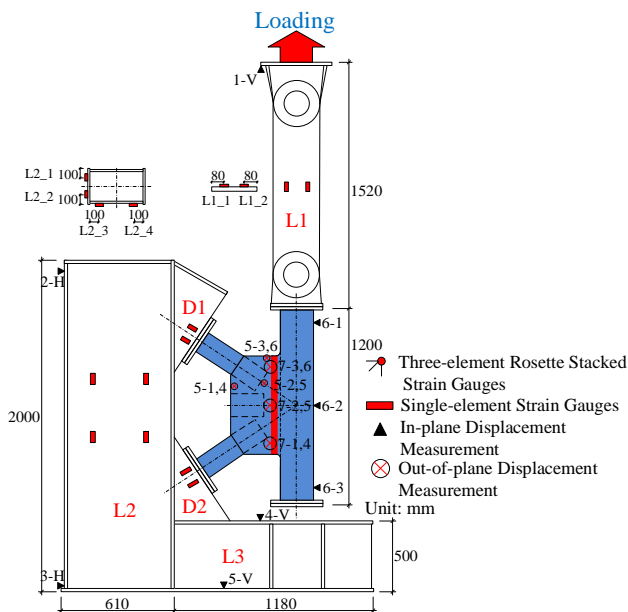


Fig. 2.6 Measured items in the link frame.

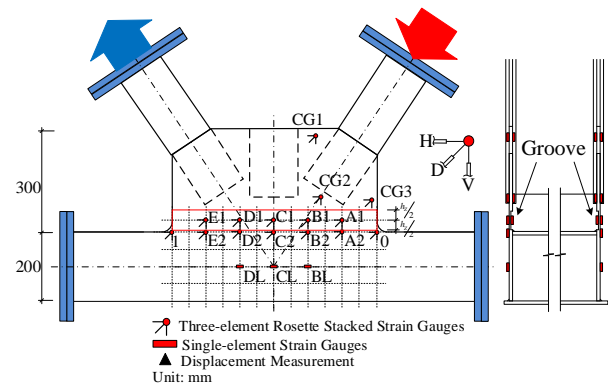


Fig. 2.7 Strain gauge locations in the gusset plate.

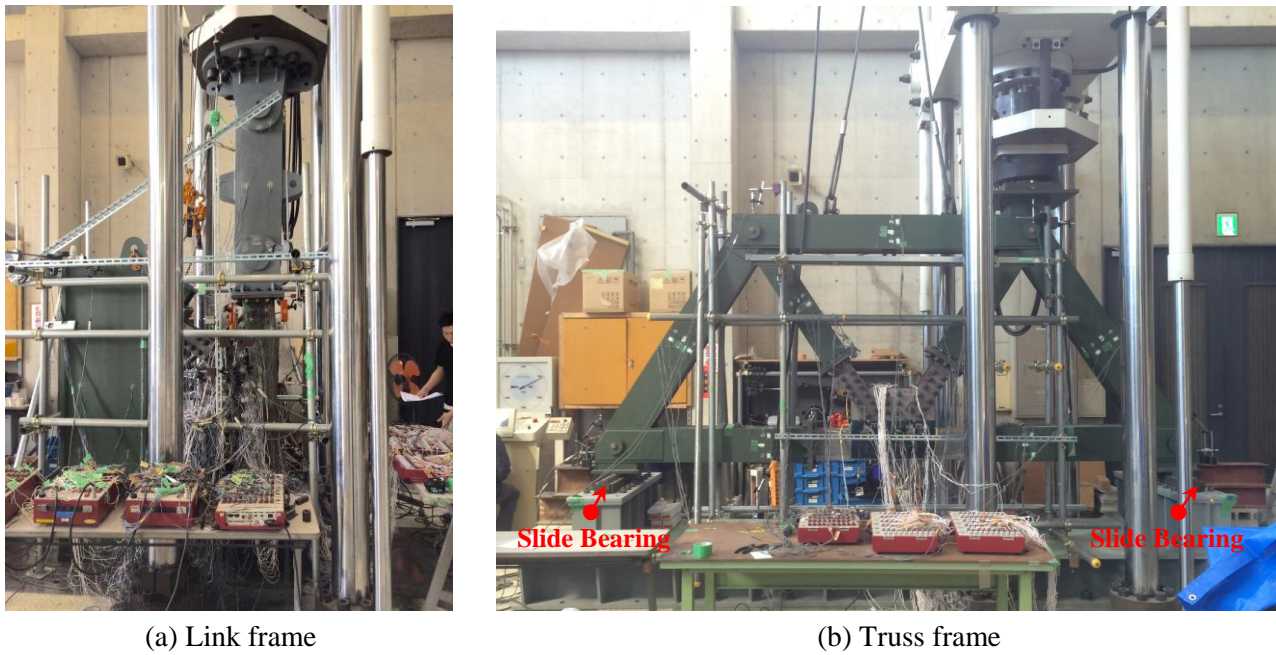


Fig. 2.8 Loading test condition.

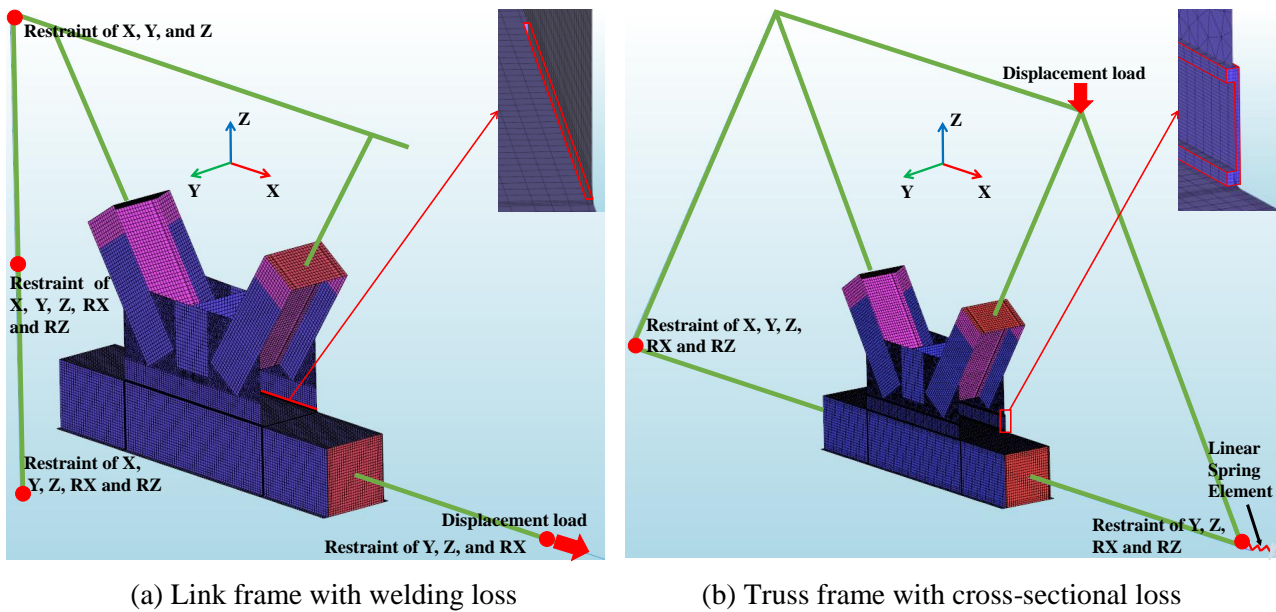


Fig. 2.9 Finite element analysis model.

SHIMADZU experimental equipment with 3000 kN capacity was used to test all specimens. The formal loading test process was only carried out after finishing the repetition about two or three times for the loading test at the elastic phase of the material. The two bottom joints of the truss frame were placed onto the two Teflon plates to allow freedom for the slide bearing. The experimental environment is shown in **Fig. 2.8**.

2.3. FINITE ELEMENT ANALYSIS OVERVIEW

Finite element analysis (FEA) was conducted to reproduce the experimental results and observed failure behavior of the loaded gusset plate connections. The analysis software used in this study was DIANA 9.6^{2.7}.

2.3.1. Analysis model

A three-dimensional geometric nonlinear analysis was implemented to model the gusset plate connections both with and without the simulated corrosion losses using a displacement load as shown in **Fig. 2.9**. The gusset plate connection and loading members were constructed of curved shell elements (the eight-node CQ40S and six-node CT30S) and the three-dimensional beam element (the two-node L13BE), respectively. In the case with the welding loss, the loss of the weld was modeled by introducing a disconnection as shown in **Fig. 2.9(a)**. In cases with a Groove section, the Groove section itself was simulated using the solid brick element (the twenty-node CHX60) (see **Fig. 2.9(b)**). The sections connecting this solid element to the shell element were considered to be in the central plane of the cross-section of the gusset plate. The boundary conditions of the right and left support of the truss frame were simulated as a roller support and a pinned support, respectively. Furthermore, the movement of the right support of the truss frame was limited by the linear translation spring element (the two-node SP2TR), as shown in **Fig. 2.9(b)**. The linear spring stiffness was determined as the average slope of the relationship between the load and displacement of the right support in the horizontal direction, as measured during the loading test with a value of approximately 24000 N/mm.

With the major aim of focusing on the failure behavior, deformation performance, and strength of the gusset plate when corrosion damage occurred on the gusset plate, the dimensions of the specimens were designed such that the failure conditions due to block shear, tensile fracture, and slippage of the gusset plate around high-tension bolts and the connecting plates would not appear during the loading tests. In addition, like the actual gusset plate connections on the subject bridges, to improve the eccentric bending moment, which could occur owing to the eccentricity between the original plane of the gusset plate and that of the flange of the diagonal member, four additional plates were attached to the outside of the gusset plate with their thickness similar to the thickness of the flange of the diagonal members, as shown in **Fig. 2.4**. Therefore, to enable easier simulation of the connecting sections between the gusset plate and the diagonal members, these connections were modeled as being monolithic. This means that the high-tension bolts were not modeled in the FEM analysis, and the gusset plate and the flange of the diagonal member was the same plane. The resolution of the finite element mesh in all of the models was 1 mm in the Groove section and 5 mm in all other members. Therefore, the total number of nodes and elements was 78223 and 27378, respectively, in the intact case, and 101403 and 28476, respectively, in cases with cross-sectional loss.

2.3.2. Material and initial imperfection

a) Steel

The stress-strain curve relationship of the SS400 steel used in this analysis was bilinear, in which the primary Young's modulus was 200 GPa, and the secondary modulus after yield was $E/100 = 2$ GPa. The Poisson ratio was 0.3, the yield stress and tensile strength were 317 MPa and 436 MPa, respectively, as declared on the mill sheet certificate. In addition, the yield stress and tensile strength of the SS400 steel were also reconfirmed through the tensile experiment in the laboratory. The Von Mises yield condition was applied to simulate the steel material, and geometric nonlinearity was considered. In this analysis, all members of the gusset plate connection were simulated as a multilinear material, and the loading members and connecting plates were considered to be elastic materials.

b) Initial imperfection (Initial deflection and residual stress)

In this study, before conducting the loading test on all specimens, the initial deflection of the gusset plates was measured directly. The measured value indicated that the average inclination level of the gusset plates was approximately 1 mm, and the initial deflection shape was considered as the SIN-shape. Therefore, the initial deflection of the gusset plate was considered in all of the analysis models. The maximum initial deflection of the gusset plate was h_w/K for the intact case N, the cross-sectional loss cases S, and L; and h_g/K for the weld loss case W, as determined using Equations (2.1) and (2.2), respectively.

$$\Delta y = \frac{h_w}{K} \sin\left(\frac{\pi}{h_w} z\right) \quad (2.1)$$

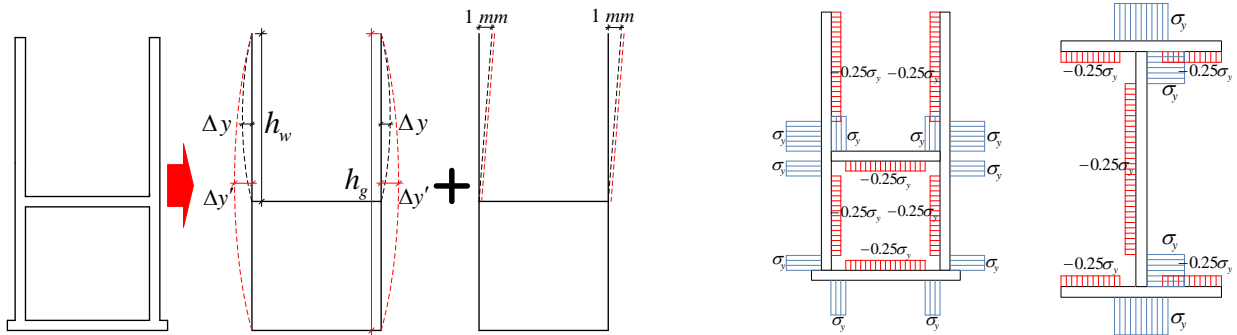
$$\Delta y' = \frac{h_g}{K} \sin\left(\frac{\pi}{h_g} z\right) \quad (2.2)$$

where, h_w is the height of the gusset plate, h_g is the height of the gusset plate connection, and K is a factor determining the maximum initial deflection.

In addition, because the final failure shape of the experimentally tested specimens was asymmetric in the plane of the loading frame, asymmetry was also considered in the initial deflection of the gusset plate in this analysis. Finally, an additional 1 mm of inclination was added to the initial deflected shape of the gusset plate to reproduce conditions measured in the field, as presented at the beginning of this section. The complete initially deflected shape of the gusset plate can be seen in **Fig. 2.10**.

The residual stress distributions on each surface of the gusset plate connection and the diagonal members were considered as shown in **Fig. 2.11**. However, in this analysis, the effect of the residual stress on the loading frame members was ignored. The shape and amplitude of the residual stress were determined by reference to the Specifications for Highway Bridges (JSHB)^{2,8}, with a stress of σ_y for the tensile region and $-0.25\sigma_y$ for the compressive region. The width of the tensile and compressive stress portions on each surface of the gusset plate connection were calculated from the self-balanced condition of the stress in the cross-section.

The initial deflection and the residual stress were input into the data file of the FEA models, which was used directly to implement the calculation. The displacement load was applied in 0.1-mm steps during the second phase of the analysis once the self-balanced condition of the residual stress was achieved.



Red dashed line: Specimen W, Black dashed line: the other specimens'

(a) Gusset plate connection (b) Diagonal member

Fig. 2.10 Initial deflection of the gusset plate.

Fig. 2.11 Residual stress distribution. σ_y : Yield stress

Table 2.2 Analysis parameters.

No.	Case	Corrosion level	Dimension of Groove section		Residual stress	Initial deflection $K(\Delta y = \frac{h_i}{K} \sin(\frac{\pi}{h_i} z))$	Test frame
			h_z (mm)	t_z (mm)			
1	N	Without corrosion	-	-	-	-	Link frame
					-	500	
					-	250	
					-	150	
					-	250	
					○	250	
2	W	Welding corrosion	-	-	-	250	Link frame
3	S	Small cross-sectional corrosion	25	4	-	250	Link frame
4	L	Large cross-sectional corrosion	50	6	-	250	Truss frame

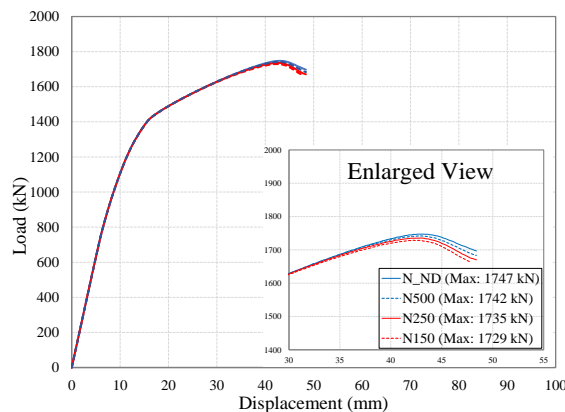


Fig. 2.12 Load-displacement relationship, subject to initial deflections of the gusset plate (Specimen N).

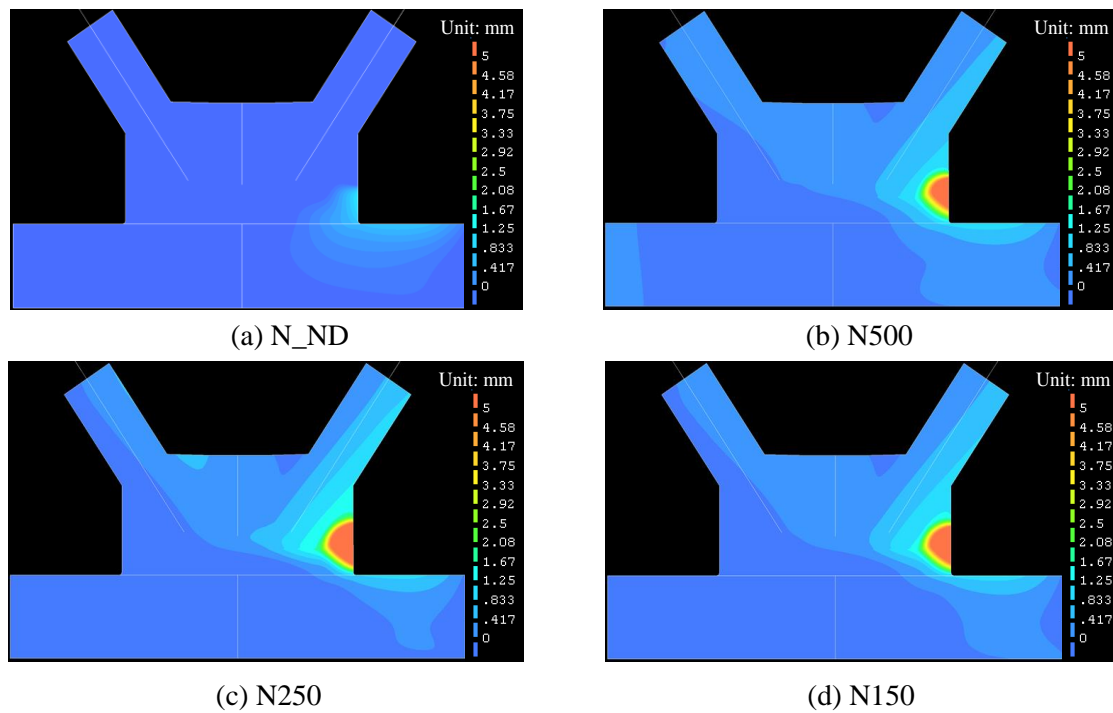


Fig. 2.13 Contour drawing of the out-of-plane deformation of the Specimen N intact series (at maximum load).

2.3.3. Analysis parameters

The parameters used to evaluate the FEM analysis presented in this section are shown in **Table 2.2**. In the case of Specimen N, which had no simulated corrosion loss, in order to clarify the influence of the initial deflection of the gusset plate on the maximum load-carrying capacity and the deformation performance of the gusset plate connection, a parametric analysis was conducted on the parameter K in Equation (2.1) for determining the initial deflection, in which the K factor was assigned values of 500, 250, and 150. The original case N_ND, in which the initial deflection was not considered, was also included in this parametric analysis. Note that the residual stress is commonly accepted to be a major influence on the load-carrying capacity and the load-displacement relationship of normal steel members under compressive force. To confirm the effects of this parameter, an additional analysis of the intact Specimen N was conducted with and without the effects of residual stress.

As the main purpose of this section was to reproduce the experimental results and failure behavior of the gusset plate connection under the loading test, an FEM analysis of the three corroded specimens (W, S, and L) was conducted. The effect of the residual stress was not considered in these cases, and the K factor was taken with 250 for all three.

2.4. ANALYSIS RESULTS AND DISCUSSION

As mentioned in Section 2, in order to reach the complete failure condition of the specimens with the limited capacity of the experimental equipment, the link frame and the truss frame were used to conduct the loading tests. Because of the difference in the loading frames, in this study, the following data from the experimental and analytical results were evaluated using the average axial force in the two diagonal members of either frame connecting directly to the specimen.

2.4.1. Intact model (Specimen N)

a) Influence of initial imperfection on maximum load

To investigate the influence of initial imperfections on the maximum load and the load-displacement relationship of the gusset plate connection under the FEM analysis, two parametric analyses were implemented by varying the initial deflection of the gusset plate and the residual stress in the gusset plate connection.

Figure 2.12 depicts the relationship between load and vertical displacement at the highest point of the tensile link member of the link frame for the Specimen N test. In **Fig. 2.12**, the K factor in Equation (1) determining the initial deflection of the gusset plate was varied, and the parametric analysis results were obtained as follows. The enlarged view attached to **Fig. 2.12** is provided to clarify the changes toward the end of the load-displacement curve. Based on the information shown in **Fig. 2.12**, when the initial deflection was changed, the initial stiffness of the gusset plate connection was completely unchanged. In fact, the load-displacement curve trend changed with initial deflection only in the phases immediately before and after achieving the maximum load, and the larger the initial deflection, the smaller the maximum load resisted by the gusset plate connection. However, the change in the maximum load was quite small. The out-of-plane deformation of each initial deflection case evaluated in the FEM parametric analysis is shown in **Fig. 2.13**, which depicts the deformation contours at maximum load. The out-of-plane deformation at the free edges of the gusset plate did not appear when the initial deflection was not considered in the case N_ND (**Fig. 2.13(a)**). However, in the cases where the initial deflection was considered, the largest out-of-plane deformation was observed at the free edges of the gusset plate, and this deformation decreased as the initial deflection decreased (**Fig. 2.13(b)**, **2.13(c)**, and **2.9(d)**). As before, this change was not considerable.

Figure 2.14 illustrates the relationship between the load and vertical displacement at the highest point of the tensile link member, in the intact Specimen N tests, both with and without residual stress on the gusset

plate connection, as determined by the FEM analysis. Clearly, the inclusion of residual stress resulted in a slightly reduced gusset plate stiffness. However, there was almost no change in the maximum load carried by the gusset plate connection: the maximum load was 1735 kN without residual stress and 1731 kN with residual stress. This small difference is due to the limited size of the compressive stress regions of the gusset plate connection, and the small residual stress levels in these areas.

From the FEM analysis results when the initial deflection of the gusset plate and the residual stress in the gusset plate connection were varied, it is confirmed that the initial imperfections had very little effect on the maximum load and the load-displacement relationship of the gusset plate connection. However, the out-of-plane deformation at the free edges of the gusset plate in all cases will not appear, if the initial deflection of the gusset plate is not considered. Therefore, in the FEM analysis of all following specimens, the K factor was taken as 250, and the residual stress was not considered.

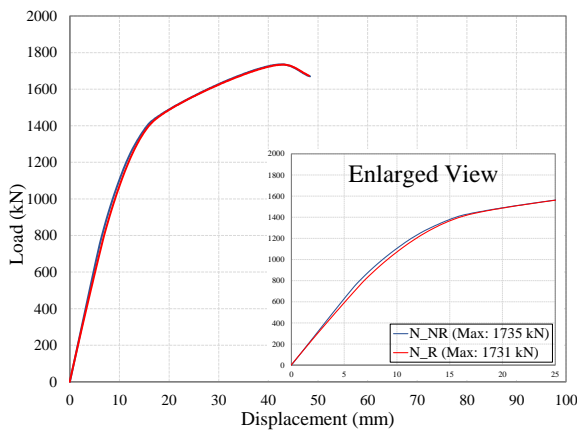


Fig. 2.14 Load-displacement relationship, subject to residual stress on the gusset plate connection (Specimen N).

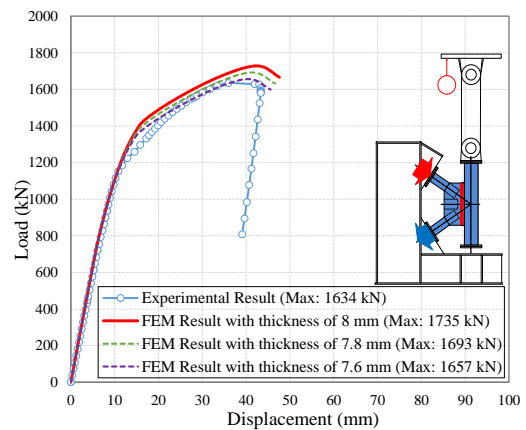


Fig. 2.15 Load-vertical displacement relationship, subject to the actual plate thickness (Specimen N).

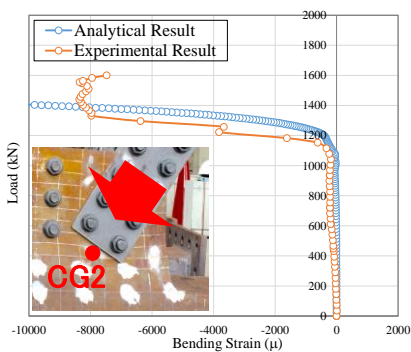


Fig. 2.16 Load-bending strain relationship (Specimen N)

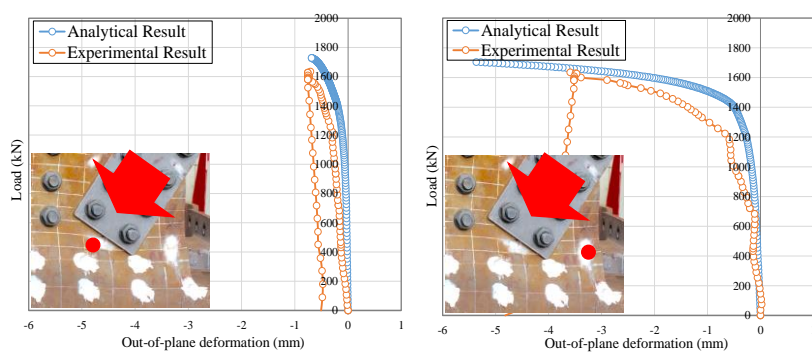


Fig. 2.17 Out-of-plane deformation of plate area underneath diagonal member (N). (a) Underneath the diagonal member (b) Free edge of the gusset plate

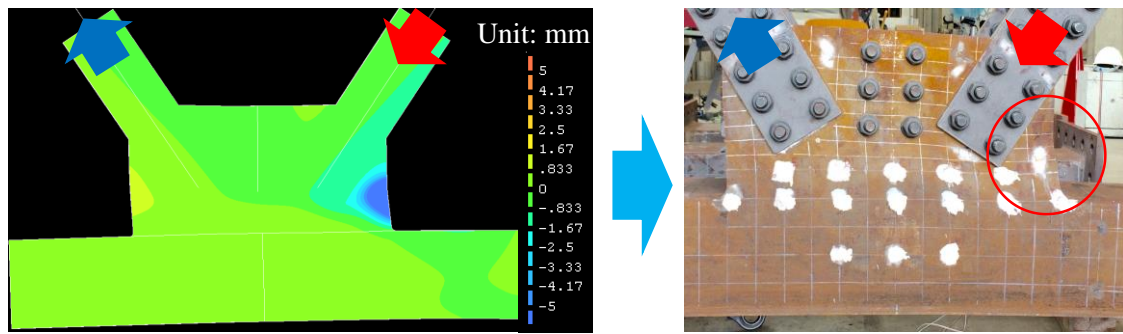


Fig. 2.18 Analytical contours of out-of-plane deformation and physical deformation of Specimen N (at maximum load).

b) Load-vertical displacement relationship

With the basic aim of determining the deformation performance, failure behavior, and load-carrying capacity of the gusset plate connection, the loading test and FEM analysis of the intact Specimen N (without any simulated corrosion loss) were implemented. The relationship between load and vertical displacement at the highest point of the tensile link member of the link frame for Specimen N are shown in **Fig. 2.15** to provide comparison between the analytical and experimental results.

From the analysis, it is clear that the load-displacement curve begins to change at a load of 1226 kN (the buckling load) due to buckling of the plate region underneath the compressive diagonal member, a trend consistent with the behavior obtained in the experiment. Furthermore, the experimental and analytical initial stiffness of the gusset plate connection was almost in agreement. After overcoming the buckling load, the load-displacement curve of the analysis diverged slightly from the experimental result; however, the difference was quite small. The maximum load carried by the gusset plate connection was 1634 kN from the experimental result, and 1735 kN from the analytical result, a difference of approximately 6%. This difference is explained by the influence of the variations in the thickness of the actual gusset plate. The measured thickness of the actual gusset plates tested at the laboratory varied from 7.6 mm to 8 mm, as did the gusset plate used for Specimen N. As in **Fig. 2.15**, a gusset plate thickness of 7.6 mm and 7.8 mm in the analysis results in a 1% and 4% difference in maximum load, respectively, compared to the experimental result.

These comparisons confirm that the load-displacement curve and the maximum load provided by the analytical result agreed well with those of the experimental result in the intact Specimen N case.

c) Failure conditions

The initial failure condition observed in the link frame tests of Specimen N was the buckling of the plate

region underneath the compressive diagonal member at a load of 1184 kN. This was confirmed by the relationship between the load and bending strain of this plate region, shown in **Fig. 2.16**. Furthermore, the load-carrying capacity of Specimen N reached the maximum value after large out-of-plane deformation occurred both in this plate region and at the free edges of the gusset plate, due to buckling.

The comparisons of the analytical results with the experimental results in **Figs. 2.16** and **2.17** clearly demonstrate that the simulated and observed relationships of load-bending strain and out-of-plane deformation in the plate region underneath the compressive diagonal member and at the free edges of the gusset plate in the compressive direction are consistent. The overall shape of the gusset plate connection is compared in **Fig. 2.18**: the out-of-plane deformation shown in the simulated contours is quite similar to the final shape of the experimental specimen after achieving maximum load.

As a result of these comparisons, the failure behavior of the gusset plate connection observed in the loading test can clearly be accurately reproduced using an FEM analysis.

2.4.2. Corroded models (Specimens W, S, and L)

a) Load-vertical displacement relationship

Damage resulting in the loss of some portions of the gusset plate is likely to reduce the load-carrying capacity of the gusset plate connection. Therefore, to clarify the relationship between damage and capacity reduction, loading tests and FEM analyses were conducted to evaluate the effects of two types of losses on the gusset plate: the loss of the flange-to-gusset weld and the loss of plate cross-section. The relationship between load and vertical displacement, determined by loading tests and FEM analyses of the weld loss Specimen W, and the small and large cross-sectional loss Specimens S and L, respectively, are shown in **Fig. 2.19**. The black dashed lines (1634 kN) indicate the load-carrying capacity of intact Specimen N, obtained by loading test and described in Section 2.4.1b.

From the experimental results, the load-carrying capacities achieved by Specimens W, S, and L were 1547 kN, 1303 kN, and 415 kN, respectively. This indicates that the loss of the weld in Specimen W resulted in a load-carrying capacity decrease of only 5.3% from that of the intact Specimen N. On the other hand, the cross-sectional loss simulated in Specimens S and L resulted in a decrease in load-carrying capacity of 20.3% and 74.6%, respectively, from that of the intact Specimen N.

The relative impacts of weld loss and cross-section area reduction on the load-carrying capacity of the

gusset plate connection have thus been clarified by the experimental results: the corrosion loss of the flange-to-gusset weld had only a slight effect, while the corrosion loss of the gusset plate cross-section had a significant effect.

The comparison of the experimental and FEM analysis results shown in **Fig. 2.19** indicates consistent agreement between the two results. The load-displacement curve in the case of Specimen W begins to change at a load of 1200 kN as a result of the buckling of the plate area underneath the compressive diagonal member. In the case of Specimen S, the load-displacement curve begins to change at a load of 800 kN due to local buckling in the Groove section, and in the case of Specimen L, this occurs at a load of 240 kN due to shear buckling in the Groove section.

The maximum load determined by the analysis was 1639 kN for Specimen W, 1334 kN for Specimen S, and 441 kN for Specimen L. The maximum loads determined by experiment and analysis for all specimens are compared in **Fig. 2.20**, in which it can be observed that the difference in maximum load between the analytical and experimental results was between -6% and -2%, indicating that the analytical model provides a high level of accuracy. The small differences observed can be mainly attributed to the influence of the varying thickness of the actual gusset plate, as described in Section 2.4.(1) b).

b) Failure condition

The results of the loading test conducted on Specimen W indicate that the initial failure condition was buckling in the plate region underneath the compressive diagonal member and near the lost portion of the weld at a load of 1200 kN. This load is determined from the relationship between the load and the bending strain of the plate region underneath the diagonal member shown in **Fig. 2.21**. The load-carrying capacity of Specimen W reached its maximum value after large out-of-plane deformation developed in the region underneath the compressive diagonal member as a result of buckling. Unlike in the intact Specimen N, Specimen W exhibited the largest out-of-plane deformations not only at the free edges of the gusset plate, but also in the region near the weld loss because losing the weld increased the effective buckling length in this area of the plate. **Figure 2.22** illustrates the relationship between the load and the out-of-plane deformation in the subject plate region, indicating that the analytical results are consistent with the experimental results.

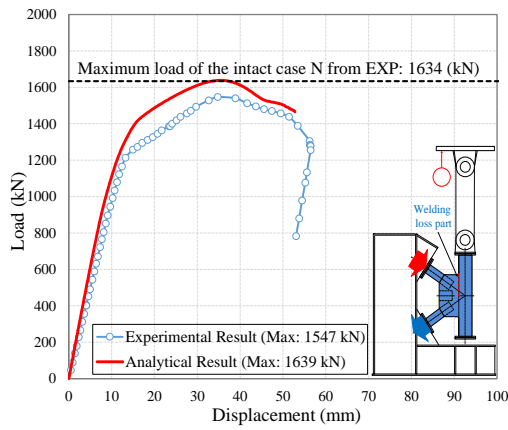
In the small cross-sectional loss Specimen S, local buckling initially appeared during the experiment in the Groove section under a load of 800 kN. This is understood to be the result of eccentricity due to the decreased

thickness of the Groove section, causing a significant increase in the bending moment in the compressive direction. This is illustrated by the relationship between the load and bending strain in the Groove section as shown in **Fig. 2.23**. Additionally, the next failure condition was marked by the appearance of buckling in the plate region underneath the compressive diagonal member at a load of 1200 kN, as determined by reference to the relationship between load and bending strain shown in **Fig. 2.24**. The final failure condition for Specimen S was the large out-of-plane deformation resulting from buckling in the plate region underneath the compressive diagonal member, and shear fracture at the Groove section. The analytically and experimentally determined relationships of load-bending strain and out-of-plane deformation in this plate region and at the free edges of the gusset plate in compression are shown in **Fig. 2.24** and **2.25**, indicating that the analytical result is consistent with the experimental result.

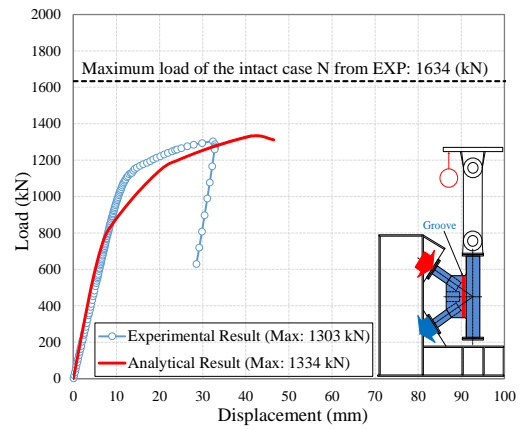
In the case of the large cross-sectional loss Specimen L, unlike Specimen S, shear buckling occurred at the Groove section. This is understood to be a result of the comparatively large height/thickness ratio of the Groove section, which reduced its shear buckling strength. The final failure in this case was the result of large deformation due to shear buckling and shear fracture. **Figure 2.26** provides a comparison of the simulated contours describing the out-of-plane deformation and the residual deformation of the gusset plate connection specimens after the conclusion of the loading tests. In this figure, the white dashed-line indicates the weld loss and Groove section areas on the gusset plate.

As a result, in the gusset plate with simulated corrosion loss of the weld, the largest out-of-plane deformations appeared not only at the free edges of the gusset plate (as in the case of Specimen N), but also in the area of the corroded weld. In the gusset plates with simulated corrosion loss of plate cross-section, the failure behavior of the corroded gusset plate depended on the severity of the corroded section: local buckling was observed in the small corrosion case of Specimen S, while shear buckling was observed in the large corrosion case of Specimen L. Notably, the failure behavior of the corroded gusset plate connections observed in the loading test could be accurately reproduced using the FEM analysis.

Moreover, from the results shown in Section 4, the influent level of not modeling the bolts of the connecting sections in the FEM analysis was confirmed to be inconsiderable through comparison of the analytical and loading test results: the difference in maximum load being between -6% and -2%, the same in the load-bending strain relationship, the load-out-of-plane deformation relationship and the physical deformation.

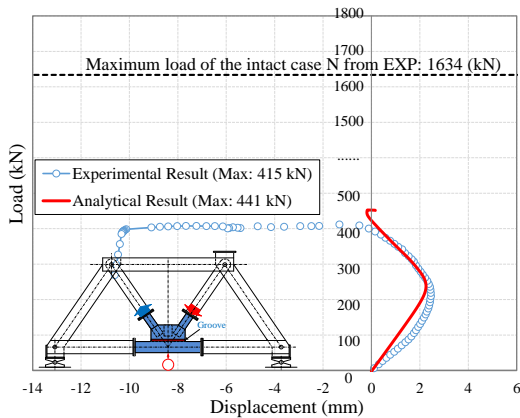


(a) Weld loss Specimen W



(b) Small cross-sectional loss Specimen S

Fig. 2.19 Load-vertical displacement relationship (W, S, and L).



(c) Large cross-sectional loss Specimen L

Fig. 2.19 Load-vertical displacement relationship (W, S, and L).

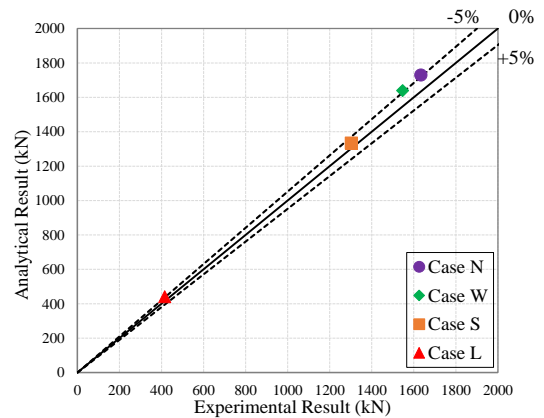
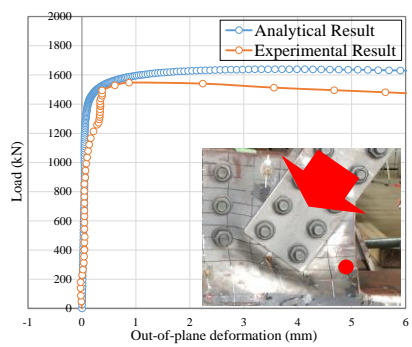
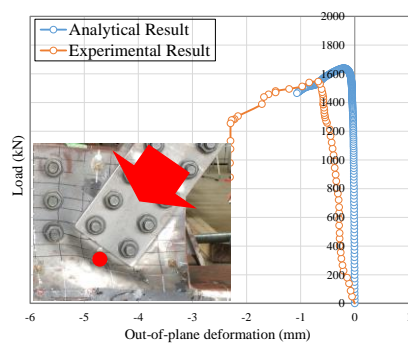
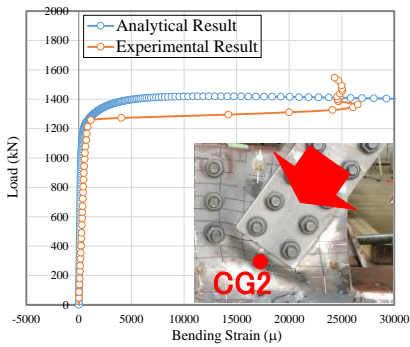


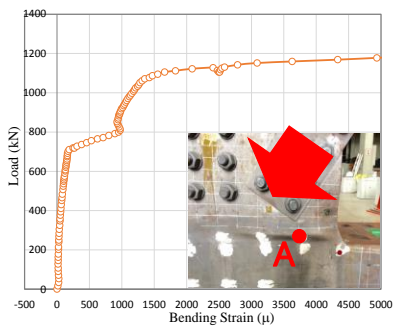
Fig. 2.20 Maximum load between FEA and EXP.



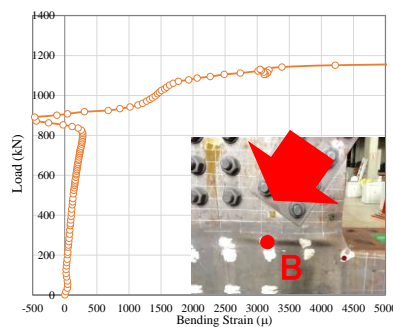
(a) Underneath the diagonal member

(b) Free edge of the gusset plate

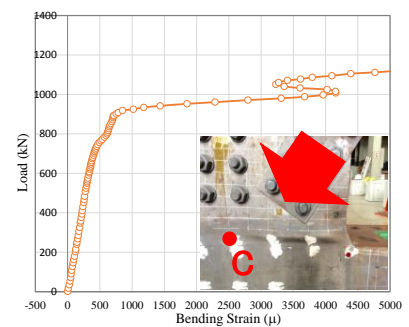
Fig. 2.21 Load-bending strain relationship (W). **Fig. 2.22** Out-of-plane deformation in plate region underneath diagonal member (W).



(a) Location A



(b) Location B



(c) Location C

Fig. 2.23 Load-bending strain relationship of Specimen S.

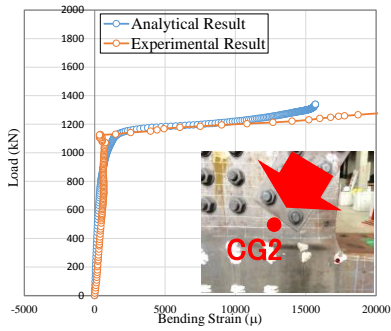
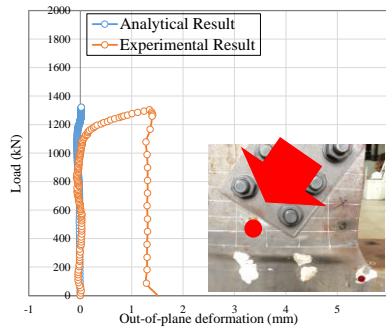
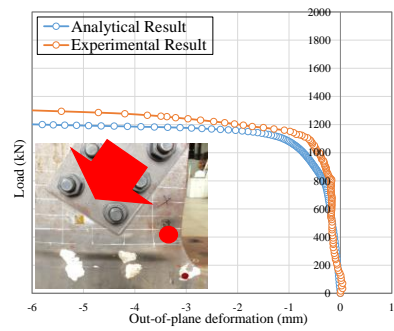


Fig. 2.24 Load-bending strain relation (S).

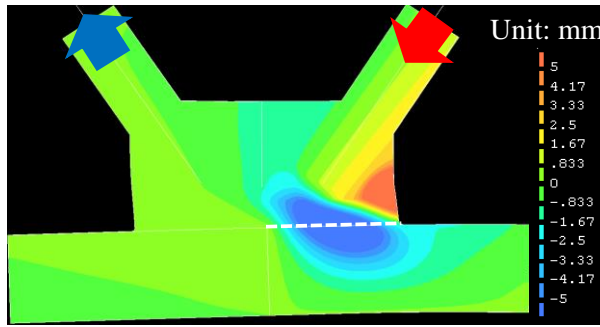


(a) Underneath the diagonal member

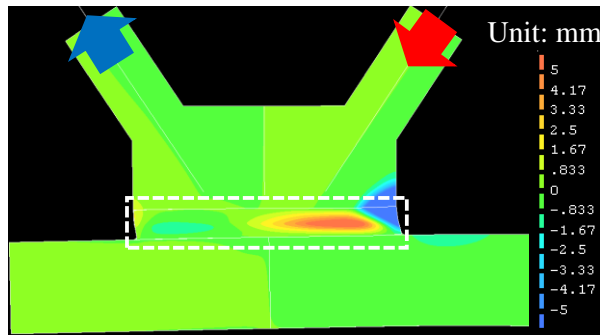
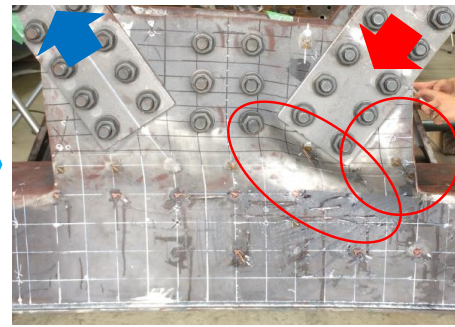


(b) Free edge of the gusset plate

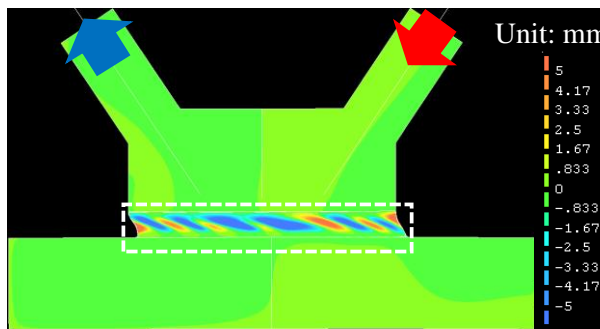
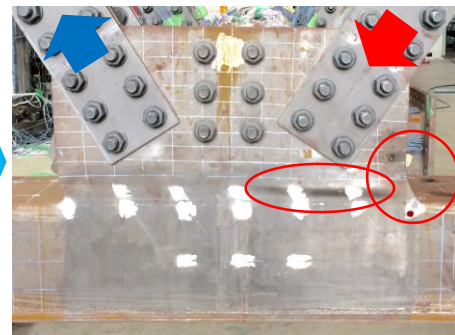
Fig. 2.25 Out-of-plane deformation in plate region underneath diagonal member (S).



(a) Weld loss Specimen W



(b) Small cross-sectional loss Specimen S



(c) Large cross-sectional loss Specimen L

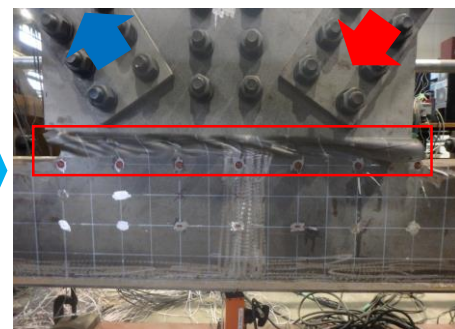


Fig. 2.26 Analytical contours of out-of-plane deformation and physical deformation of the gusset plate (at maximum load).

2.5. PARAMETRIC ANALYSIS

Once the FEM analysis had been confirmed as accurate by comparison with the experimental results, two parametric FEM analyses were conducted to investigate the relationship between the remaining capacity of the corroded gusset plate connection and the degree of corrosion in the two forms evaluated.

2.5.1. Analysis parameters

The loading tests and the FEM analysis conducted in Section 2.4 both concluded that the damage due to corrosion could lead to a reduction in the load-carrying capacity of the gusset plate connection. The most significant reductions were observed in the cross-sectional corrosion cases. The failure conditions of the cross-sectionally corroded region depended on the corrosion level, either manifesting as local buckling under a small degree of corrosion or as shear buckling under a large degree of corrosion. To obtain further information on the remaining load-carrying capacity, failure behavior, and deformation performance of the gusset plate connection with even more severe corrosion, a parametric analysis was implemented by varying the degree of cross-sectional loss in the gusset plate. The analysis cases conducted are listed in **Table 2.3**, consisting of remaining thickness of 87.5%, 75%, 62.5%, 50%, 43.75%, 37.5%, and 25% of the original gusset plate thickness. For each thickness, the height of the corroded section was evaluated for approximately 50% and 100% of the maximum height of the potentially damaged area, defined as 50 mm in this study. Note that the link frame model was applied in all these FEM analysis cases.

An additional parametric FEM analysis was conducted by varying the length of the flange-to-gusset weld loss, detailed in the cases listed in **Table 2.4**, in which the length of the corroded weld was assumed to be either 50% or 100% of the length of the gusset plate, which was defined as 600 mm in this study.

Table 2.3 Parametric analysis parameters for cross-sectional corrosion loss cases.

No.	Case	Remaining thickness of corroded section / 8 mm (%)	Height of corroded section / 50 mm (%)	Dimension of Groove section		Test frame	Note
				t_z (mm)	h_z (mm)		
1	t87.5h50	87.5%	50%	1	25	Link frame	
2	t87.5h100		100%		50		
3	t75h50	75%	50%	2	25		
4	t75h100		100%		50		
5	t62.5h50	62.5%	50%	3	25		
6	t62.5h100		100%		50		
7	t50h50	50%	50%	4	25		EXP
8	t50h100		100%		50		
9	t43.75h50	43.75%	50%	4.5	25		
10	t43.75h100		100%		50		
11	t37.5h50	37.5%	50%	5	25		
12	t37.5h100		100%		50		
13	t25h50	25%	50%	6	25		
14	t25h100		100%		50		EXP

Table 2.4 Parametric analysis parameters for flange-to-gusset weld loss cases.

No.	Case	Location of corroded weld	Length of corroded weld / 600 mm (%)	Test frame	Note
1	W50	Compressive direction	50%	Link frame	EXP
2	W100	Compressive direction + Tensile direction	100%		

2.5.2. Results of parametric analyses

a) Load and vertical displacement relationship

Figure 2.27 depicts the relationship between the applied load and vertical displacement of the gusset plate connection as the cross-sectional loss parameter was varied from remaining thicknesses of 87.5%, 75%, 62.5%, 50%, 43.75%, 37.5%, to 25%. The inset diagram in each figure depicts an enlarged view of the initial stiffness of the gusset plate connection. When looking at **Fig. 2.27**, it is immediately obvious that for remaining thicknesses of 87.5%, 75%, 62.5%, and 50%, the initial stiffness of the gusset plate connection exhibited nearly no change with the reduction rate in the range of 2% to 5%. However, for considerable cross-sectional losses (remaining thicknesses of 43.75%, 37.5%, and 25% of the plate), a significant decrease in the initial stiffness can be clearly observed with the reduction rate in the range of 9% to 13%. Moreover, in all cases with the cross-sectional loss, the load-displacement curve began to change after the first signs of failure appeared in the Groove section. The details of the observed initial failure condition in the Groove section in each case were as described in Section 2.5.(2)c).

The relationships between load and vertical displacement of the gusset plate connection as the length of the flange-to-gusset weld loss was varied are shown in **Fig. 2.28**. As the enlarged view of the initial stiffness shown inset in **Fig. 2.28** illustrates, there was almost no change in the initial stiffness of the gusset plate connection with the reduction rate of 3% to 5% as the length of the corroded weld increased. Additionally, the load-displacement curve of the gusset plate connection did not significantly change until buckling occurred in the plate region underneath the compressive diagonal member.

The results of the FEM parametric analyses indicate that a significant reduction in the initial stiffness of the gusset plate connection occurs in cases when the thickness of the gusset plate has been reduced by more than 50%. In cases with less than 50% loss of thickness, there is no significant reduction in stiffness. Finally, there was no change observed in the initial stiffness of the gusset plate connection as the length of the corroded portion of the flange-to-gusset weld was increased.

b) Remaining load-carrying capacity

The maximum loads determined using the parametric FEM analysis of the change in cross-sectional loss are shown in **Fig. 2.29(a)**, in which the horizontal axis and vertical axis depict P_{\max}/P_{\max}^0 and the remaining thickness (%), respectively. In this figure, P_{\max} and P_{\max}^0 are the maximum load carried by the cross-sectional

loss case and the maximum load of the intact Specimen N, respectively. As shown in **Fig. 2.29(a)**, the loss of the gusset plate cross-section significantly decreased the load-carrying capacity of the gusset plate connection. For both Groove section heights evaluated, the relationship between P_{\max}/P_{\max}^0 and the remaining thickness rate were approximately linear, while the value of P_{\max}/P_{\max}^0 exhibited a sharp decrease when the failure condition in the Groove section changed from local buckling to shear buckling.

For the same remaining thickness, as the height of the Groove section was increased, a reduction in the maximum capacity of the gusset plate connection was only notable for cases in which local buckling appeared in the Groove section, while only a slight reduction was observed for cases in which shear failure or shear buckling occurred in the Groove section. The final failure of the gusset plate in cases failing by shear buckling was due to shear failure (i.e., insufficient shear strength) of the Groove section, which is independent of the height of the cross-sectional loss. On the other hand, the final failure of the gusset plate in cases failing by local buckling in the Groove section was due to the large out-of-plane deformation that appeared in the plate region underneath the compressive diagonal member.

The parametric FEM analysis determined that as the length of the corroded flange-to-gusset weld increased, the maximum loads were as shown in **Fig. 2.29(b)**, which reveals that the loss of the weld only slightly reduced the load-carrying capacity of the gusset plate connection, in the range of 5% to 7%. This is understood to be a result of the compressive strength of the diagonal member, which determines the load-carrying capacity of the gusset plate connection, and thus depends greatly on the dimensions and strength of the free edges of the gusset plate in the compressive direction. Obviously, the behavior of these free edges was not at all affected by the loss of the flange-to-gusset weld.

c) Failure condition

Figure 2.30 shows the contours of the residual out-of-plane deformation of the gusset plate connection as the degree of cross-sectional loss was varied. The results obtained from the FEM analyses confirmed that the initial failure condition of the gusset plate occurred in the Groove section in all cases. For the cases with a Groove height of 25 mm (50% of the maximum damaged section height), local buckling appeared in the Groove section when the remaining plate thickness was greater than 50% of the original (see **Figs. 2.30(a1)-2.30(d1)**). For the cases with a Groove height of 50 mm (100% of the maximum damaged section height), local buckling in the Groove section was observed when the remaining thickness was greater than

37.5% of the original (see **Figs. 2.30(a2)-2.30(e2)**). In all these cases, at the peak load value the gusset plates failed from large out-of-plane deformation due to the buckling in the plate region underneath the compressive diagonal member and at the free edges of the gusset plate.

In the other cases, the initial failure condition of the gusset plates was observed to be shear failure or shear buckling in the Groove section (see **Figs. 2.30(e1)-2.30(g1)**, and **2.30(f2)-2.30(g2)**), and at their peak load-carrying capacity the gusset plates failed from large deformation of the Groove section due to shear failure.

The contours describing the out-of-plane deformation of the gusset plates at maximum load as the length of the flange-to-gusset weld loss was increased can be seen in **Fig. 2.31**. The FEM analysis indicates that in all cases, the initial failure condition region underneath the compressive diagonal member, nearest to the lost weld, and the final failure condition was large out-of-plane deformation in the plate region nearest to the lost weld, and at the free edges of the gusset plate. The size of the region exhibiting large out-of-plane deformation near the lost weld can be observed to increase considerably as the length of the weld loss increased.

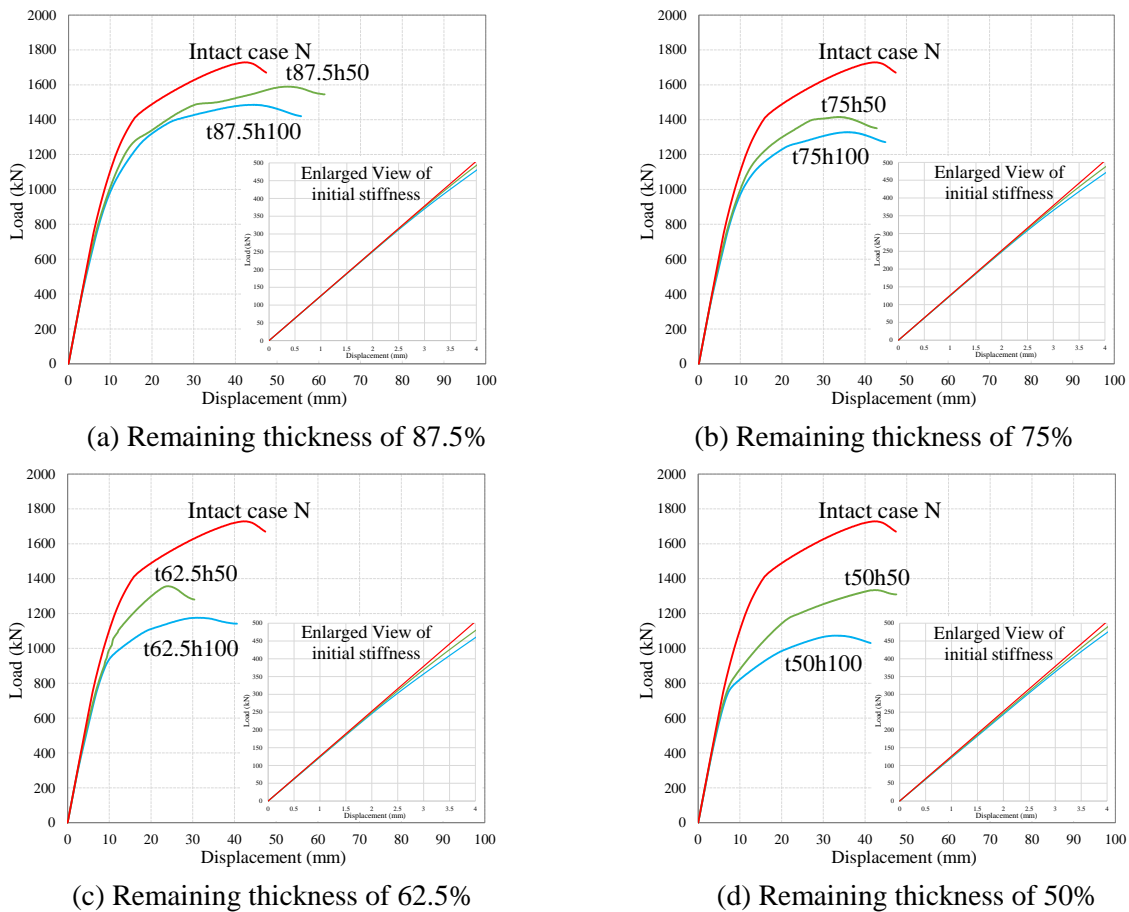
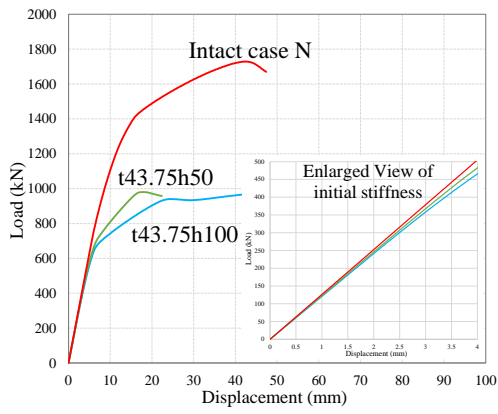
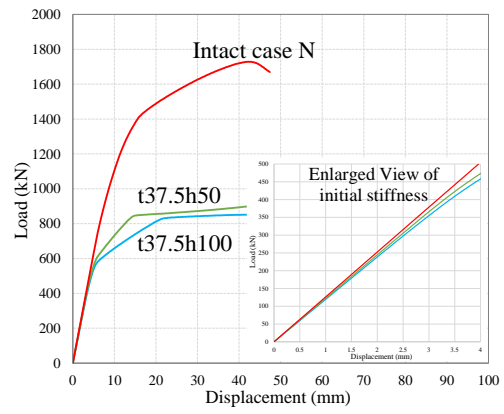


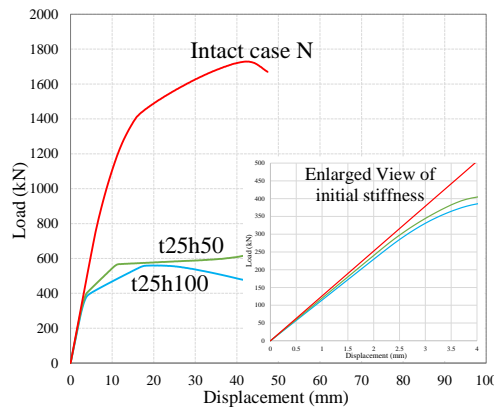
Fig. 2.27 Load-displacement relationship as the cross-sectional loss parameter is varied.



(e) Remaining thickness of 43.75%



(f) Remaining thickness of 37.5%



(g) Remaining thickness of 25%

Fig. 2.27 Load-displacement relationship as the cross-sectional loss parameter is varied.

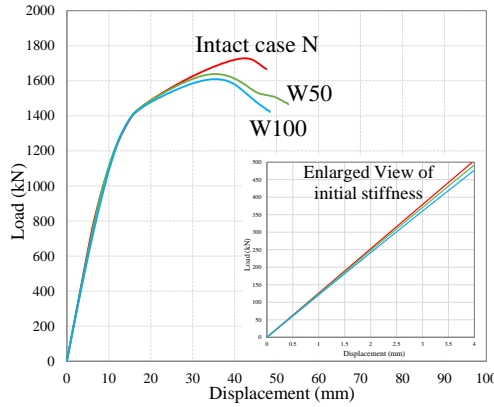
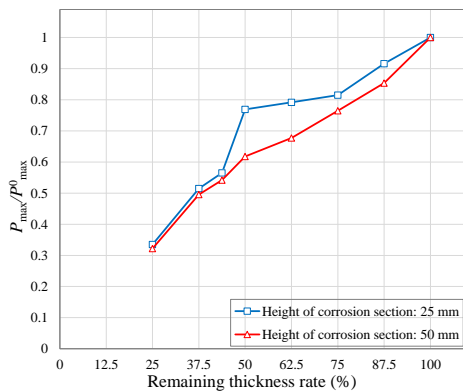
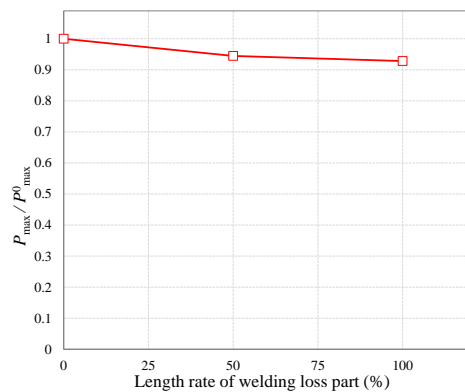


Fig. 2.28 Load-displacement relationship as the flange-to-gusset weld loss parameter is varied.



(a) Cross-sectional loss



(b) Flange-to-gusset weld loss

Fig. 2.29 Relationship between corrosion loss and remaining load-carrying capacity.

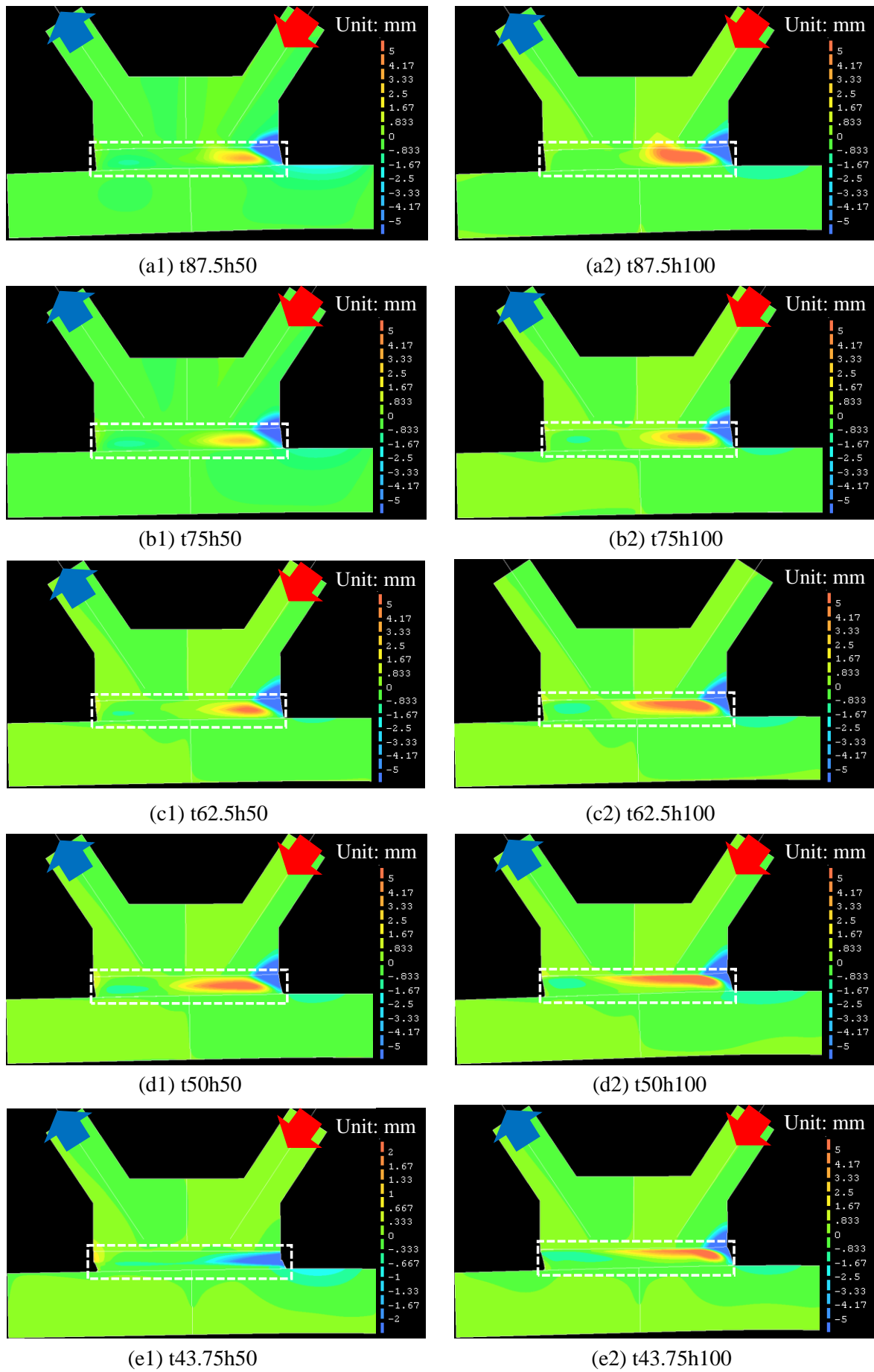


Fig. 2.30 Analysis contours of out-of-plane deformation as the cross-sectional loss is varied (at maximum load).

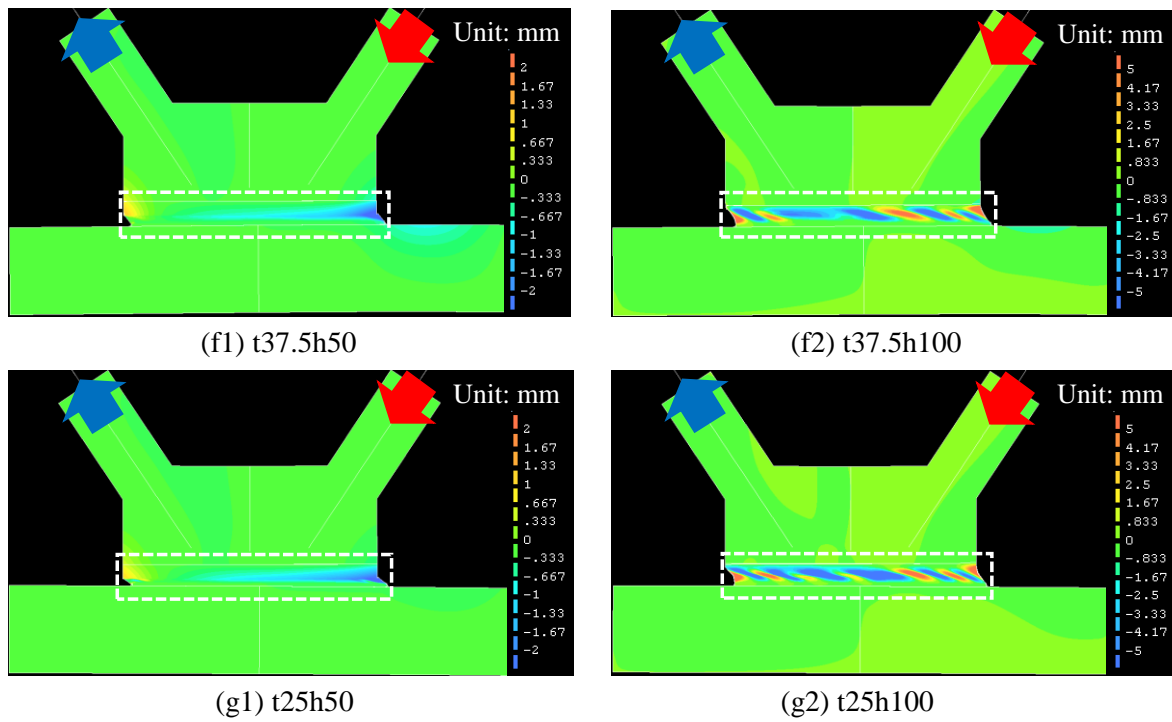


Fig. 2.30 Analysis contours of out-of-plane deformation as the cross-sectional loss is varied (at maximum load).

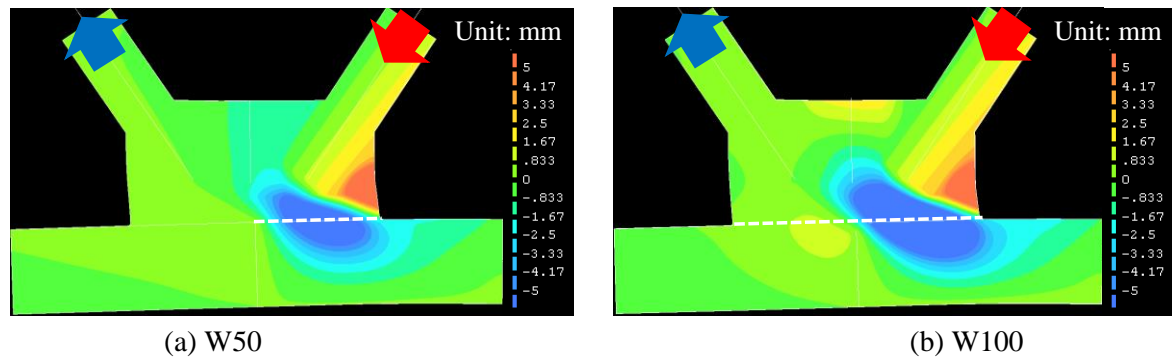


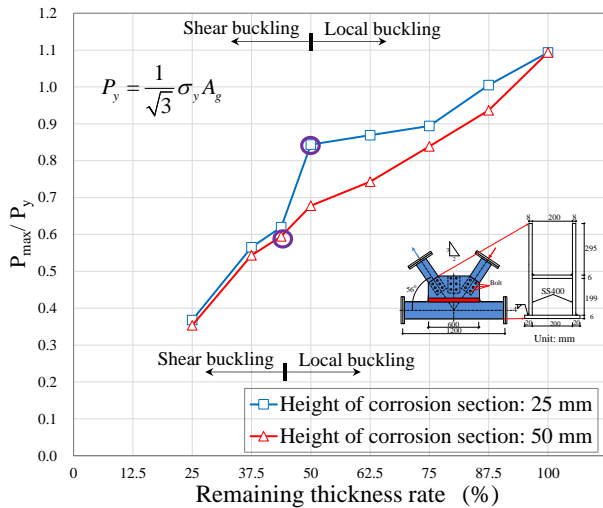
Fig. 2.31 Analysis contours of out-of-plane deformation as the length of the flange-to-gusset weld loss is varied (at maximum load).

2.5.3. Remaining load-carrying capacity under the full-scale model of a real bridge

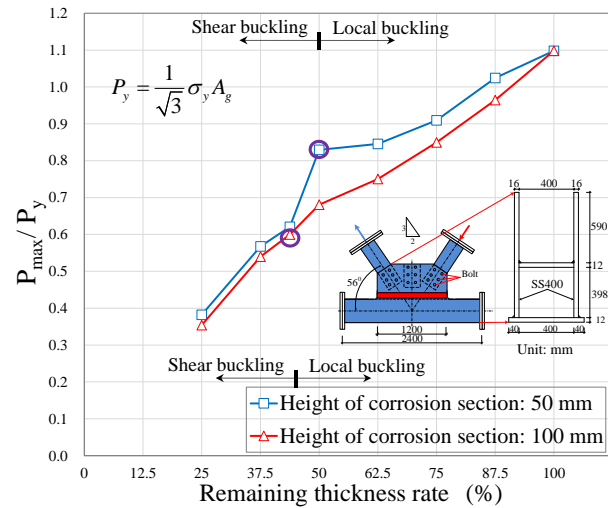
In this Section, in order to grasp further information on the remaining load-carrying capacity, failure behavior, and deformation performance of the actual gusset plate connection with the cross-sectional corrosion; an additional parametric analysis was conducted under the full-scale model of a real bridge. The dimension of the actual gusset plate connection in this parametric analysis was larger 2 times than that of the model of specimens. The analysis cases implemented are listed in **Table 2.5**, including the thickness of the corroded section being 12.5%, 25%, 37.5%, 50%, 62.5%, and 75% of the original gusset plate thickness. Moreover, for each thickness, the height of the corroded section was evaluated for about 50% and 100% of the maximum height of the potentially damaged area, defined as 100 mm in this Section.

Table 2.5 Parametric analysis parameters for cross-sectional corrosion loss cases under the full scale model of a real bridge.

No.	Case	Height of corroded section / 100 mm (%)	Thickness of corroded section / 16 mm (%)	Dimension of Groove section		Shape of Groove section
				h_z (mm)	t_z (mm)	
1	N	—	—	—	—	
2	S12.5	50%	12.5%	50	2	
3	S25		25.0%		4	
4	S37.5		37.5%		6	
5	S50		50.0%		8	
6	S56.25		56.3%		9	
7	S62.5		62.5%		10	
8	S75		75.0%		12	
9	L12.5		100%		12.5%	
10	L25	25.0%		4		
11	L37.5	37.5%		6		
12	L50	50.0%		8		
13	L56.25	56.3%		9		
14	L62.5	62.5%		10		
15	L75	75.0%		12		



(a) The dimensions of Specimen



(b) The dimensions of the actual model

Fig. 2.32 Remaining load-carrying capacity curve, normalized to the horizontal shear yield strength of the intact gusset plate.

The maximum loads obtained from the parametric FEM analysis of the change in cross-sectional loss level are shown in **Fig. 2.32**, in which the horizontal axis and vertical axis illustrate the remaining thickness rate (%) and P_{max}/P_y , respectively. **Figure 2.32(a)** described the remaining load-carrying capacity curve obtained from Section 2.5.2(b) with the dimensions of Specimen, and **Fig 2.32(b)** provided the remaining load-carrying capacity curve with the dimensions of the actual gusset plate connection. In these figures, P_{max} and P_y are the maximum load carried by the cross-sectional loss cases and the horizontal shear yield strength of the intact gusset plate, respectively. In addition, the horizontal shear yield strength of the intact gusset plate was calculated by using the following equation (2.3).

$$P_y = \frac{1}{\sqrt{3}} \sigma_y A_g = \frac{1}{\sqrt{3}} \sigma_y 2bL \quad (2.3)$$

where, σ_y is the yield stress of the steel, A_g is the cross-sectional area of the gusset plate.

As shown in **Fig. 2.32(b)** with the dimensions of the actual gusset plate connection, the remaining load-carrying capacity curves were approximately linear, while the value of P_{max}/P_y exhibited a sharp decrease when the failure condition in the corroded section changed from local buckling to shear buckling. Moreover, for the cases with the dimensions of the actual gusset plate, the remaining load-carrying capacity curves normalized to the horizontal shear yield strength of the intact gusset plate is completely the same with that of the cases with the dimensions of specimens obtained from Section **2.5.2(b)**. Therefore, by using the remaining load-carrying capacity curves, normalized to the horizontal shear yield strength of the intact gusset plate; the load-carrying capacity of corroded gusset plate connection on real bridges can be effectively determined. In addition, the results of the parametric analysis in this Section also indicated that the failure condition on the actual gusset plate agreed completely with that of the gusset plate connection under the dimensions of the specimen.

2.6. EVALUATION EQUATION FOR LOCAL BUCKLING STRENGTH

2.6.1. Proposed evaluation equation

This section proposes an evaluation method for determining the local buckling strength of the plate region underneath the compressive diagonal member in cases of the corrosion loss of the gusset plate thickness. For the specimens tested in the experiments, the diagonal members were connected to the gusset plate using bolts through the connecting plates. Therefore, the effective width of the buckling plate area was determined in accordance with the Whitmore method^{2,10)} (**Fig. 2.33(a)**). The local buckling strength of the plate region with the cross-sectional corrosion was then calculated from three component fixed-end-columns (l_{01} , l_{02} , and l_{03}) with the sudden change in cross-section, as shown in **Fig. 2.33(b)**. In this evaluation method, the eccentricity of the cross-sectional loss section and the initial deflection of the local buckling plate region is neglected. Thus, the buckling load condition of each “component column” with sudden change in cross-section can be described by Equation (2.4).

$$\left(\frac{\lambda_1}{\lambda_2} \right) \tan(\lambda_1 l_1) + \tan(\lambda_2 l_2) = 0 \quad (2.4a)$$

$$\begin{aligned}\lambda_1 &= \sqrt{P/EI_1} \\ \lambda_2 &= \sqrt{P/EI_2}\end{aligned}\quad (2.4b)$$

where, E is the elastic modulus of steel; l_1 and l_2 are the length of the plate region without and with corrosion, respectively; and I_1 and I_2 are the moment of inertia of the plate region without and with corrosion, respectively (see **Fig. 2.33(b)**).

The process of calculating the local buckling strength of the plate region underneath the compressive diagonal member is as shown in the flowchart in **Fig. 2.34**. More specifically, it is described as follows.

In Step 1, the effective buckling length (\bar{l}_{01} , \bar{l}_{02} , and \bar{l}_{03}) of each component column was calculated by using the local buckling strength (P_1 , P_2 , and P_3) of each component column, calculated using Equation (2.4a). Then, in Step 2, the slenderness ratio $\bar{\lambda}_c$ of the plate region in which the local buckling occurred was determined as the average value of the three component slenderness ratios, by Equation (2.5b).

The slenderness ratio is determined by:

$$\begin{cases} l_{01} \Rightarrow \bar{l}_{01} = \pi \sqrt{\frac{EI_{01}}{P_1}} \\ l_{02} \Rightarrow \bar{l}_{02} = \pi \sqrt{\frac{EI_{02}}{P_2}} \\ l_{03} \Rightarrow \bar{l}_{03} = \pi \sqrt{\frac{EI_{03}}{P_3}} \end{cases} \Rightarrow \begin{cases} \lambda_{c1} = \left(\frac{1}{\pi}\right) \sqrt{\frac{\sigma_y}{E}} \left(\frac{\bar{l}_{01}}{r_{s1}}\right) \\ \lambda_{c2} = \left(\frac{1}{\pi}\right) \sqrt{\frac{\sigma_y}{E}} \left(\frac{\bar{l}_{02}}{r_{s2}}\right) \\ \lambda_{c3} = \left(\frac{1}{\pi}\right) \sqrt{\frac{\sigma_y}{E}} \left(\frac{\bar{l}_{03}}{r_{s3}}\right) \end{cases}\quad (2.5a)$$

$$\Rightarrow \bar{\lambda}_c = \frac{\lambda_{c1} + \lambda_{c2} + \lambda_{c3}}{3}\quad (2.5b)$$

where, I_{01} , I_{02} , and I_{03} are the moment of inertia of each component column; r_{s1} , r_{s2} , and r_{s3} are the radius of gyration of each component column; λ_{c1} , λ_{c2} , and λ_{c3} are the slenderness ratio of each component column; and σ_y is the yield stress of the steel.

Finally, the local buckling strength of the compressive plate area was determined using the standard buckling equations specified in Japanese Design code^{2,8)} (JSHB) with the previously calculated slenderness ratio value, as shown in Equation (5).

$$P_{cr} = \sigma_y A_{average} \quad (\bar{\lambda}_c \leq 0.2) \quad (2.6a)$$

$$P_{cr} = (1.109 - 0.545\bar{\lambda}_c) \sigma_y A_{average} \quad (0.2 < \bar{\lambda}_c \leq 1.0) \quad (2.6b)$$

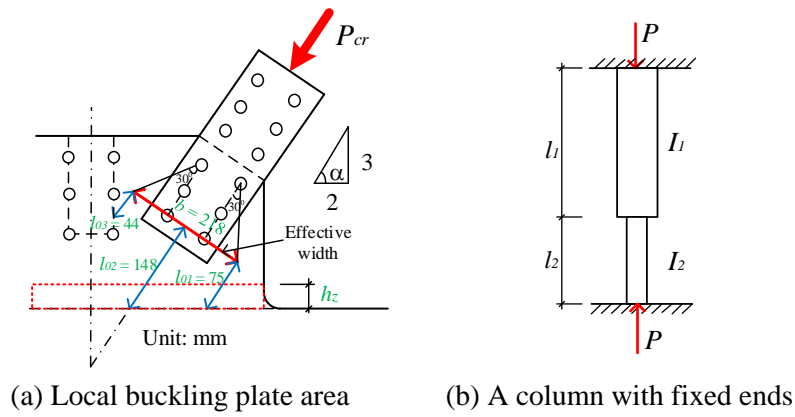
$$P_{cr} = \frac{1}{0.773 + \bar{\lambda}_c^2} \sigma_y A_{average} \quad (1.0 < \bar{\lambda}_c) \quad (2.6c)$$

where, $A_{average}$ is the average cross-sectional area of the plate.

2.6.2. Calculated result and discussion

The details of the process used to calculate the local buckling strength of the plate region underneath the compressive diagonal member with cross-sectional corrosion are shown in **Table 2.6** and **Table 2.7**. To confirm the accuracy of the proposed evaluation method, the local buckling strength value obtained from the parametric FEM analyses, the loading tests, are also listed in **Table 2.7**. Further, a comparison of the local buckling strength predicted by the loading test and analysis and by the proposed calculation is shown in **Fig. 2.35(a)**. To evaluate the differences between the proposed calculation method and a method using another standard buckling strength curve, another set of results, calculated with AASHTO, was included, as shown in **Fig. 2.35(b)**. The information shown in **Fig. 2.35** indicates that when using the buckling strength curve obtained by JSHB, the difference in strength between the calculated and observed results was in the range of -10% to 0% on the safe side, indicating that the proposed calculated result had a high level of accuracy. However, when using the buckling strength curve of AASHTO, the difference in strength between the calculated and observed results was in the range of -10% to +10%, with only some of the results on the safe side. This is due to the fact that for the same slenderness ratio, the value of the buckling strength given by the strength curve in JSHB is typically lower than that given by AASHTO, as shown in **Fig. 2.36**. Therefore, to safely evaluate the local buckling strength of the compressive plate area, the use of the standard buckling strength curve given by JSHB is strongly preferred.

Figure 2.37 illustrates the calculated local buckling strength of the cross-sectionally corroded section using the proposed method for various corrosion heights and remaining thicknesses. In this figure, the shear strength of the cross-sectionally corroded section is expressed by the value of the shear yield strength. It is immediately obvious that for both corrosion heights, the intersections between the local buckling strength curve and the shear yield strength line are consistent with the point at which the mode of failure of the cross-sectionally corroded section (obtained in Section 2.5.2 c)) changes from local buckling to shear buckling. This demonstrates that using the relationship between the local buckling strength curve and the shear yield strength line can effectively determine the change in the failure condition of a corroded gusset plate cross-section.



(a) Local buckling plate area (b) A column with fixed ends

Fig. 2.33 Local buckling underneath the compressive diagonal.

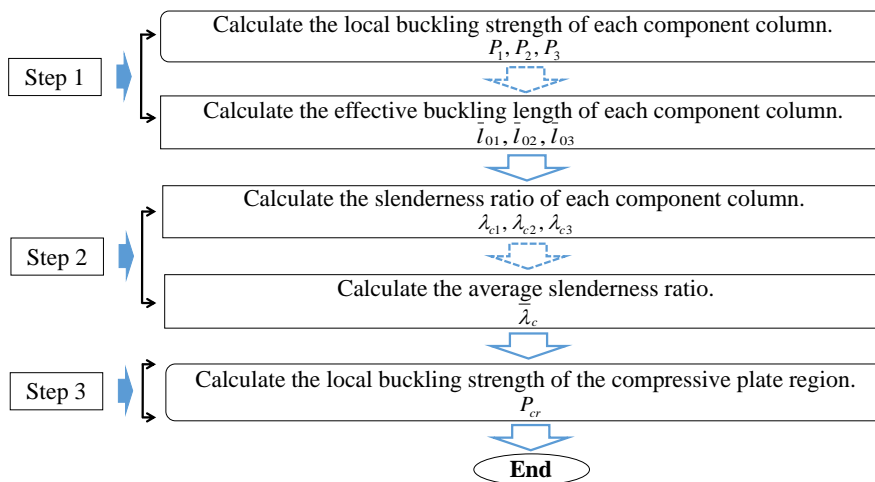


Fig. 2.34 Flowchart of process for calculating the local buckling strength.

Table 2.6 Calculating the local buckling strength of the three component columns of the gusset.

Case	$l_{01, 02 \text{ and } 03}$ (mm)	h_z (mm)	l_1 (mm)	l_2 (mm)	t_1 (mm)	t_2 (mm)	$t_{average}$ (mm)	b (mm)	I_1 (mm ⁴)	I_2 (mm ⁴)	E (MPa)	I_{0i} ($i = 1\sim3$) (mm ⁴)	P_i ($i = 1\sim3$) (kN)	
t50h50	Column 1	75	45.0	30.0	8	4	6.4	218	9301	1163	200000	4757	1412	
	Column 2	148	25	118.0	30.0	8	4	7.2	218	9301	1163	200000	6747	385
	Column 3	44	25	44.0	0.0	8	8	8.0	218	9301	9301	200000	9301	37934
N	Column 1	75	25	45.0	30.0	8	8	8.0	218	9301	9301	200000	9301	13056
	Column 2	148	25	118.0	30.0	8	8	8.0	218	9301	9301	200000	9301	3353
	Column 3	44	25	44.0	0.0	8	8	8.0	218	9301	9301	200000	9301	37934

Table 2.7 Calculating the local buckling strength of the plate region underneath the compressive diagonal member.

Case	$\bar{l}_{0i} = \pi \sqrt{\frac{EI_{0i}}{P_i}}$ ($i = 1\sim3$) (mm)	r_{si} ($i = 1\sim3$) (mm)	$\lambda_{ci} = \left(\frac{1}{\pi}\right) \sqrt{\frac{\sigma_y}{E}} \left(\frac{\bar{l}_{0i}}{r_{si}}\right)$ ($i = 1\sim3$)	$\bar{\lambda}_c$	$A_{average}$ (mm ²)	P_{cr} (kN)			
						CAL	FEM	EXP	
t50h50	Column 1	81.5	1.8	0.56	0.61	1569	775	820	800
	Column 2	185.9	2.1	1.14					
	Column 3	22.0	2.3	0.12					
N	Column 1	37.5	2.3	0.21	0.24	1744	1079	1226	1184
	Column 2	74.0	2.3	0.41					
	Column 3	22.0	2.3	0.12					

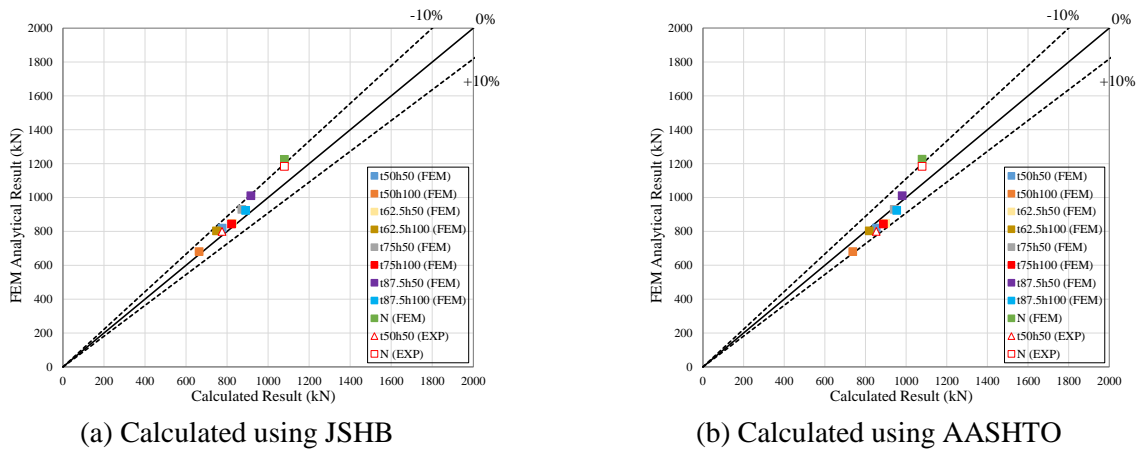


Fig. 2.35 Calculated (CAL), analytical (FEM), and experimental (EXP) local buckling strengths.

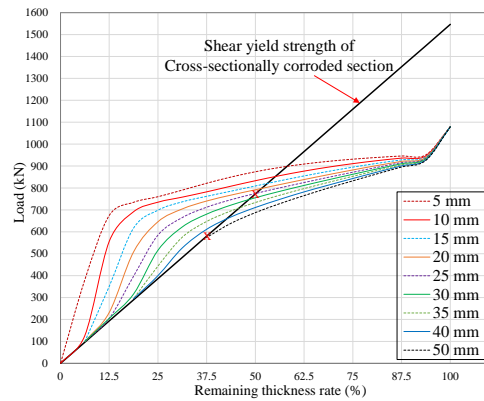
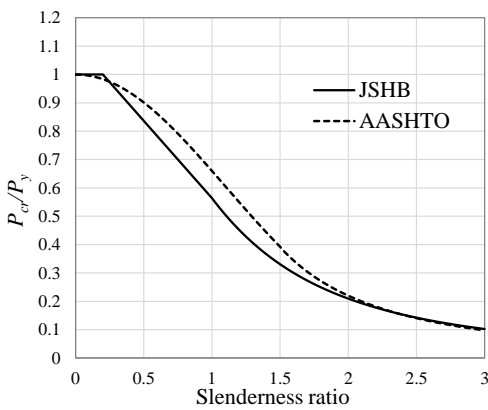


Fig. 2.36 Standard buckling strength curve. **Fig. 2.37** Changed point of failure condition of the corroded section.

2.7. CONCLUSION

This study evaluated the effects of two different forms of gusset plate corrosion on the load-carrying capacity of the gusset plate connection: the loss of the flange-to-gusset weld and the loss of the gusset plate cross-section. Loading tests performed in the laboratory and an FEM analysis were conducted on an existing bridge configuration using an approximately half-scale model. The gusset plate connections were tested for 50% and 75% corrosion of the gusset plate thickness, and 50% corrosion of the length of the flange-to-gusset weld in compression. This study then conducted parametric FEM analyses by changing the size of the corroded sections to verify the relationship between the remaining load-carrying capacity and corrosion levels with the model of specimen and the full-scale model of an actual bridge. Finally, based on the results of the parametric FEM analysis of cases with the corrosion loss of the gusset plate thickness, an evaluation method for determining the local buckling strength of the corroded section was proposed. The results obtained from this study are summarized as follows:

- (1) The reduction in the load-carrying capacity of the gusset plate connection resulting from corrosion was

determined using the experimental results. Specifically, only a slight reduction in the load-carrying capacity was observed in the case of flange-to-gusset weld corrosion, while significant reduction in capacity was observed in the case of cross-sectional corrosion.

(2) The experimental results revealed that in the case of flange-to-gusset weld corrosion, large out-of-plane deformation appeared not only at the free edges of the gusset plate, but also in the area of the corroded weld. In cases with cross-sectional corrosion, local buckling was observed to be the failure mechanism of a plate with a small degree of corrosion and shear buckling was verified as the failure mechanism of a plate with a large degree of corrosion.

(3) The deformation performance, failure behavior, and load-carrying capacity of the gusset plate connection observed in the loading tests was reproduced with high accuracy using an FEM analysis in all cases.

(4) The results of the parametric FEM analyses confirmed that there was a significant reduction in the initial stiffness of gusset plate connections in cases of corroded gusset plates with less than 50% of the original thickness remaining. Corroded gusset plates with greater than 50% remaining thickness showed little change in stiffness. No change was observed in the initial stiffness of the gusset plate connection when the length of the flange-to-gusset weld corrosion was extended.

(5) Based on the results of the parametric FEM analysis, as the dimensions of the corroded sections were increased, the load-carrying capacity of the gusset plate connection decreased. Specifically, for each cross-sectional corrosion height evaluated, the load-carrying capacity of the gusset plate connection exhibited nearly the same linear decrease with the increasing thickness of the cross-sectional corrosion of the section. Furthermore, the load-carrying capacity of the gusset plate connection was found to sharply drop when there was a change in the failure condition of the corroded section. Only a slight reduction in capacity, in the range of 5% to 7%, was found as the length of the flange-to-gusset weld corrosion increased from 50% to 100% of the gusset plate width.

(6) The parametric FEM analysis results revealed that under the effects of cross-sectional corrosion, local buckling in the corroded section occurred in cases with more than 50% of the original gusset thickness remaining for a corrosion height of 25 mm (50% of the potential corroded section), and in cases with more than 37.5% of the original gusset thickness remaining for a corrosion height of 50 mm (100% of the potential corroded section). Shear failure or shear buckling in the corrosion section was observed in the other cases. In

cases of flange-to-gusset weld corrosion, large out-of-plane deformation was observed in the area near the corroded weld during failure.

(7) The parametric analysis results with the dimensions of the actual gusset plate connection indicated that the load-carrying capacity of corroded gusset plate connection on real bridges can be effectively determined, by using the remaining load-carrying capacity curves, normalized to the horizontal shear yield strength of the intact gusset plate. In addition, the failure behavior and the deformation performance of the actual gusset plate connection agreed completely with that of the gusset plate connection under the dimensions of the specimen.

(8) In this study, it was proposed that the local buckling strength of the cross-sectionally corroded section was evaluated as a column with suddenly changing cross-section properties. The calculated result obtained from this proposed evaluation method was on the safe side in the range of -10% to 0% when compared to the results of the FEM analysis and loading tests.

(9) Using the proposed method to evaluate the local buckling strength of the cross-sectionally corroded section, it was confirmed that the relationship between the local buckling strength curve and the shear yield strength line can be used to easily determine the failure conditions of a cross-sectionally corroded section.

REFERENCES

- 2.1) Janberg, N.: International Database for Civil and Structural Engineering, <https://structurae.net/structures/bridges-and-viaducts/truss-bridges>, 1998-2018. (Accessed on March 2017)
- 2.2) Lichtenstein, A. G.: Inspection and rehabilitation of steel truss for highway bridges, In: *Bridge Management, Inspection, Maintenance, Assessment and Repair* (reference book), Springer US, USA, pp. 695-704, 1990.
- 2.3) Lima, K., Robson, N., Oosterhof, S., Kanji, S., DiBattista, J. and Montgomery, C. J.: Rehabilitation of a 100-year-old steel truss bridge, *CSCE 2008 Annual Conference*, Canada, pp. 1-11, 2008.
- 2.4) National Transportation Safety Board: Collapse of I-35W highway bridge Minneapolis, Minnesota, Accident report, NTSB/HAR-08/03, PB2008-916203, August 2007.
- 2.5) Hatano, H., Murakami, S., Rokugou, Y. and Yoda, T.: Summary of NTSB report on I-35W bridge in Minneapolis, *Bridge and Foundation*, pp. 37-42, 2010.
- 2.6) Kasano, H. and Yoda, T.: Collapse mechanism and evaluation of node damages of I-35W Bridge, Minneapolis, USA, *Proceedings of Japan Civil Engineering Association-A*, Vol. 66, No. 2, pp. 312-323, 2010 (in Japanese).
- 2.7) Manie, J. and Kikstra, W. P.: DIANA Finite Element User's Manual, Analysis Procedures (release 9.6), TNO DIANA b.v., 2016.
- 2.8) Japan Road Association: *Specification for highway bridges, Part-2 Steel Bridges*, Tokyo, Maruzen Publication, 2012 (in Japanese).
- 2.9) Liu, C., Miyashita, T. and Nagai, M.: Analytical study of steel I-girders with local corrosion nearby supports, *Procedia Engineering*, Vol. 14, pp. 2276-2284, 2011.
- 2.10) Whitmore, R. E.: *Experimental Investigation of Stresses in Gusset-Plates*, *Engineering Experiment Station*, University of Tennessee, Knoxville, Bulletin, No. 16, May 1952.
- 2.11) Kasano, H., Yoda, T., Nogami, K., Kishi, Y. and Lin, W.: Proposal of strength equation for gusset plates subjected to compressive force in steel truss bridge, *Journal of Structural Engineering*, Vol. 62A, pp. 84-92, March 2016.

CHAPTER 3

EXPERIMENTAL STUDY ON REPAIR METHOD USING CFRP SHEETS

3.1. INTRODUCTION

In steel truss bridges, several severe damage due to corrosion at gusset plate connection has been widely reported. The reduction of the load-carrying capacity of the gusset plate connection is confirmed to lead to the collapse of the entire truss bridge. Attachment of stiffening plate and member replacement are among the conventional methods often applied to repair corroded structures. However, these repair works lack efficacy because of the heavy machinery and welding facilities required. Therefore, a simple and effective repair method for the corroded gusset plate connection is urgently needed. In order to overcome this problem, Chapter 3 focused on investigating the effectiveness of repair method by using carbon fiber reinforced polymers (CFRP) for the corroded gusset plate connection. CFRP sheets are used as the repair material for the corroded gusset plate connection because of its light weight, high strength, and superior durability. Loading tests were conducted with a model approximately 50% the size of an actual bridge and the degree of corrosion assumed to be approximately 50% of the gusset plate thickness. Further, the loading tests were carried out with three parameters of the repair method: including the area of the bonded CFRP sheets, the direction (± 45 degrees: the direction of principal stress on the gusset plate, ± 56 degrees: the direction of the diagonal member, and 90 & 0 degrees: the direction resisting the horizontal shear stress on the corroded section) of the bonded CFRP sheets, and the location of the bonded CFRP sheets (out-side bonding and both-sides bonding). This Chapter established a proper repair method for the corroded gusset plate connection. The improvement rate of the strength of the corroded gusset plate and the effectiveness of the proposed repair methods were evaluated by using the obtained load-testing results.

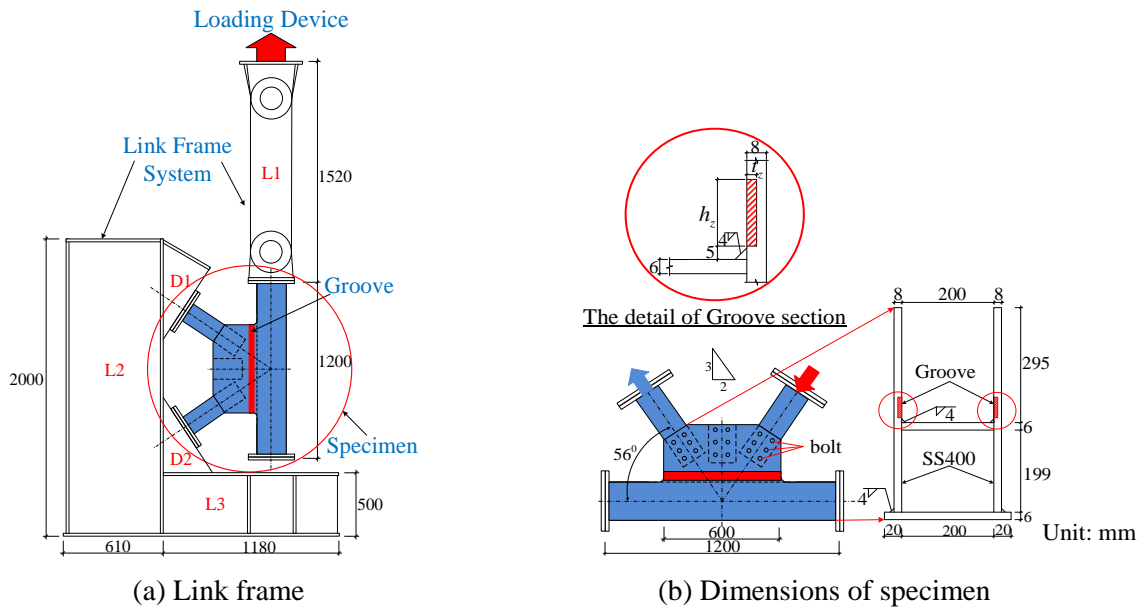


Fig. 3.1 Specimen shape.


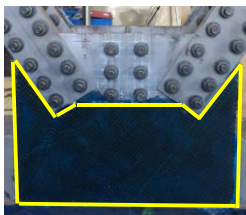
Table 3.1 Properties of CFRP sheet and steel.

	CFRP (FTS-C8-30)	Steel (SS400)
Elastic modulus (GPa)	640	200
Tensile strength (MPa)	2430	–
Yield stress (MPa)	–	317
Poisson's ratio	0.3	–
Design thickness (mm)	0.143	–
Density (g/cm ³)	2.1	7.86

Table 3.2 Properties of putty and resin.

	Polyurea putty	Resin	Groove section putty
Amount of coating (g/m ²)	1000	1000	–
Coating thickness (mm)	0.8	0.85	–
Young's modulus (MPa)	54.7	2533	4021
Density (g/cm ³)	1.25	1.17	1.53

Table 3.3 Experimental parameters.

No.	Specimen	Dimension of Groove section		The area of bonding CFRP sheets	The direction of bonding CFRP sheets	The location of bonding CFRP sheets	Number of CFRP (layer)		
		h_z (mm)	t_z (mm)						
1	N	–	–	–	–	No repair	–		
2	S	–	–	–	–	No repair	–		
3	S1_45	25	4		±45° (The direction of principal stress on the gusset plate)	Out side	9 outer (each direction)		
4	S2_45					Both sides	4 inner + 5 outer (each direction)		
5	S1_56					Out side	9 outer (each direction)		
6	S2_56					Both sides	4 inner + 5 outer (each direction)		
7	S2_90						±56° (The direction of the diagonal member)	Out side	9 outer (each direction)
								Both sides	4 inner + 5 outer (each direction)
							90° & 0° (The direction resisting the horizontal shear stress of the corroded section)	Both sides	4 inner + 5 outer (each direction)

3.2. EXPERIMENTAL OVERVIEW

3.2.1. Specimen shape

The specimens used in this study were of the monolith-type, denoting that the projected web-plates of the lower chord member were employed as a gusset plate. In addition, these models were approximately 50% the size of the real bridge. Further, their dimensions were decided with respect to the shape of real truss bridges on which corrosion damage of the gusset plate connection had been found. The length and width of the gusset plate connection and the thickness of gusset plate were 1200 mm, 216 mm, and 8 mm, respectively (**Fig. 3.1**). Moreover, the cross-sectional loss part owing to corrosion was expressed by cutting a groove (called the “Groove”) at the location connecting the gusset plate and the lower chord member, with height h_z and width t_z . The loading tests were conducted in the laboratory with the link frame system for all specimens, as shown in **Fig. 3.1(a)**. The frame loading system was connected to the specimen using bolts through the connecting plates. In addition, only the specimen was changed after finishing the loading test; the frame of the loading system was kept for the ensuing test.

3.2.2. Properties of the materials

a) Steel and CFRP sheet

The mechanical properties of CFRP sheet and the steel used in this study are listed in **Table 3.1**. SS400 steel was used as a base metal. Its yield stress is 317 MPa and elastic modulus is 200 GPa, as determined based on the mill sheet certificate. The employed FTS-C8-30 CFRP, in sheet form, is lightweight (2.1 g/cm^3), has a large tensile strength (2430 MPa), and is durable in harsh environments. In particular, the FTS-C8-30 CFRP sheet has an elastic modulus that is 3.2 times higher than that of the steel. Further, the design thickness of CFRP sheet is 0.143 mm. These mechanical values were used directly in the design to determine the number of CFRP layers used in this study.

b) Putty and resin

Table 3.2 lists the mechanical properties of polyurea putty and resin. In this study, to maximize the effectiveness of the proposed method using CFRP sheets, and prevent delamination of CFRP layers under large deformations such as buckling, polyurea putty with a low elastic modulus (54.7 MPa) and high elongation (300%-500%) was inserted between the steel and CFRP sheet. Moreover, the epoxy-type putty filled the cross-sectional loss part of the groove, with a coating amount that accorded with the amount of loss of the

gusset plate thickness.

3.2.3. Experimental parameters

The experimental parameters in this study are shown in **Table 3.3**. With the basic aim of grasping the deformation performance, failure behavior, and load-carrying capacity of the gusset plate connection, a loading test onto the intact case without the cross-sectional loss part was conducted. The level of corrosion in this study was assumed to be approximately 50% of the gusset plate thickness, with the dimensions of the Groove section being $h_z = 25$ mm, $t_z = 4$ mm. In the corroded case, in order to consider the effectiveness of using the CFRP bonding method, loading tests were conducted for the repaired and non-repaired cases. For the bonding method, the loading tests were conducted with three parameters: including the area of the bonded CFRP sheets (see **Table 3.3**, **Fig. 3.2**, and **Fig. 3.3**); the direction of the bonded CFRP sheets (± 45 degrees: the direction of principal stress on gusset plate, ± 56 degrees: the direction of the diagonal member, 90° degrees: the direction resisting the horizontal shear stress on the Groove section); and the location of the bonded CFRP sheets (out-side bonding and both-sides bonding). In addition, with the aim of considering a simpler method of bonding CFRP sheets onto the cross-sectional loss part, this study proposes two CFRP bonding methods, both-sides and outside bonding, as shown in **Fig. 3.2** and **Fig. 3.3**. In the both-sides bonding method, CFRP sheets are bonded to the outside and inside of the gusset plate. At the inside, CFRP sheets were connected continuously to the upper flange of the lower chord member by an R-shape (R50). Space created by this R-shape was filled with the epoxy-type putty. In the outside bonding method, CFRP sheets are bonded only to the outside of the gusset plate.

Therefore, seven specimens were tested: one intact specimen (Specimen N), one corroded specimen without repair (Specimen S), two specimens (S1_45, S2_45) with the bonded CFRP direction of ± 45 degrees, two specimens (S1_56, S2_56) with the bonded-CFRP direction of ± 56 degrees, and one specimen (S2_90) with the CFRP sheets of the 90° -direction bonding in both sides of the gusset plate. The specimens were named according to the corrosion level: No corrosion, Small corrosion, abbreviated N, S, respectively. The numbers following the names are the face numbers of the bonded CFRP sheet, the direction of bonding CFRP sheets, respectively.

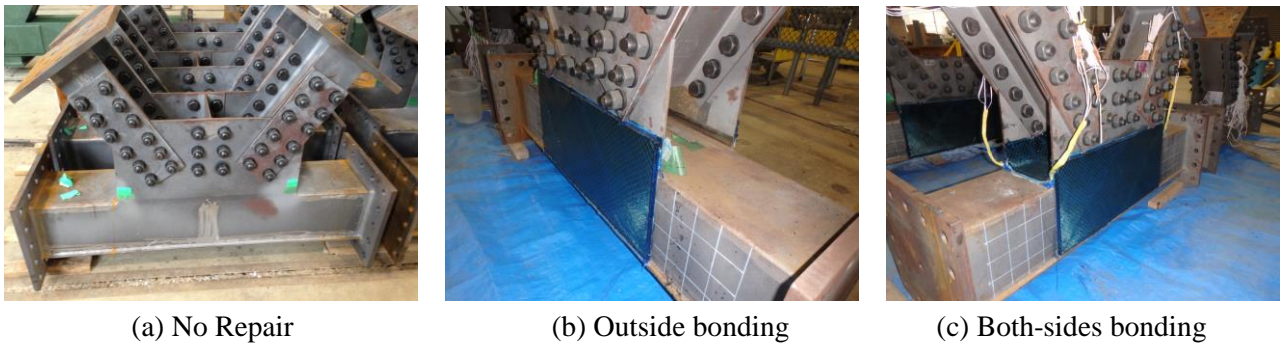


Fig. 3.2 The specimens before loading test.

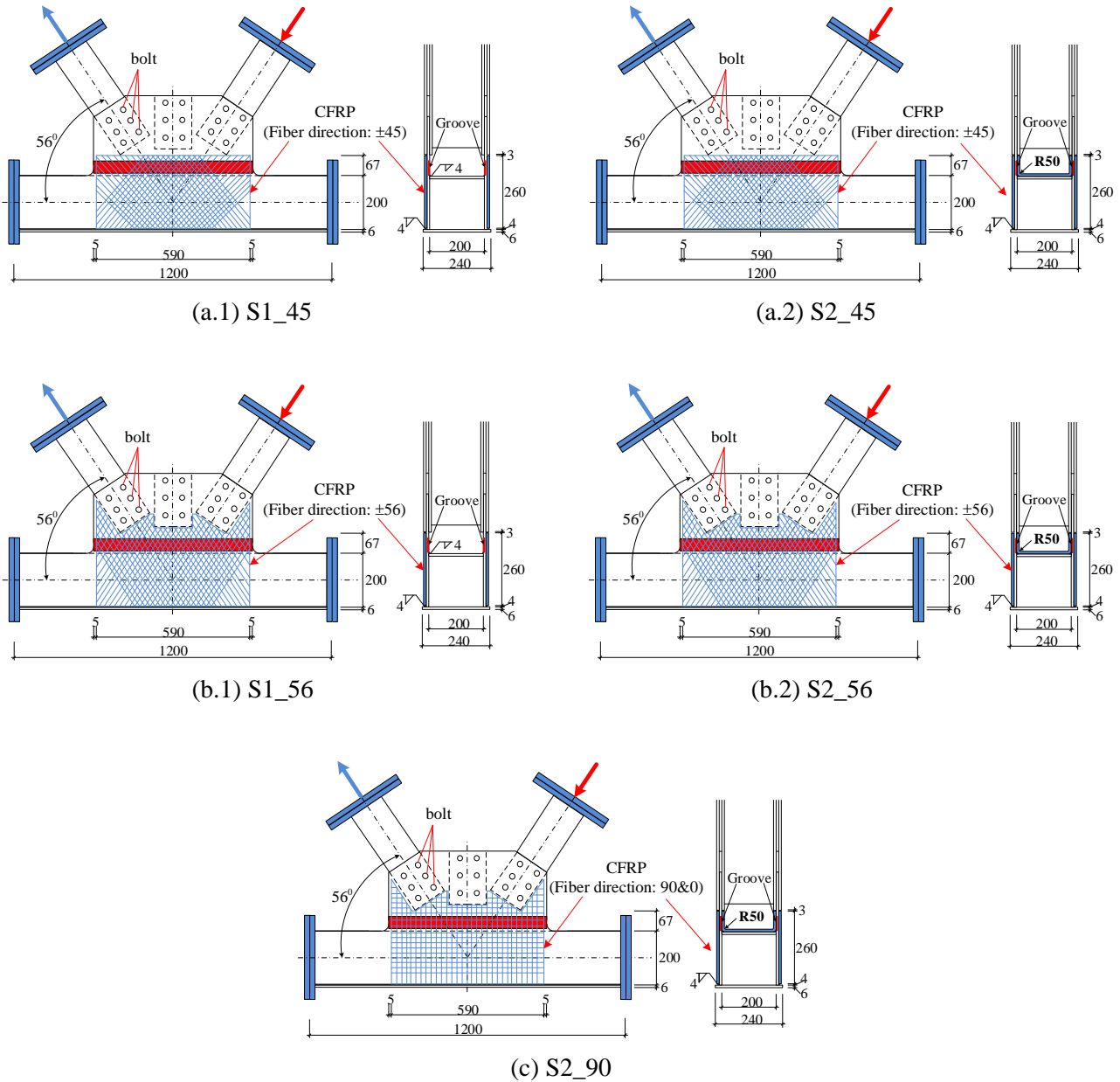


Fig. 3.3 The CFRP bonding methods on the corroded gusset plate.

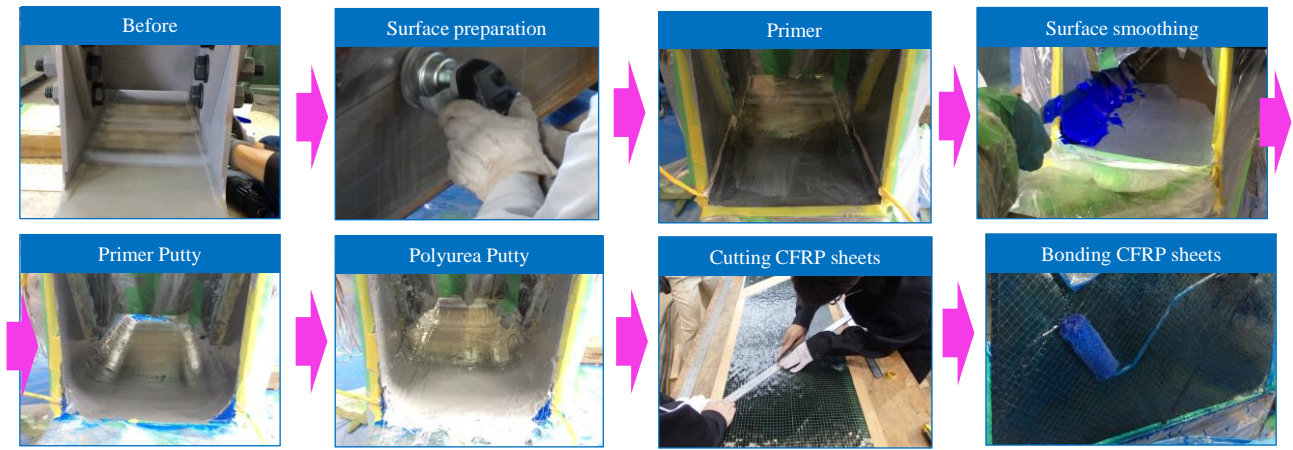


Fig. 3.4 Process bonding CFRP sheets.

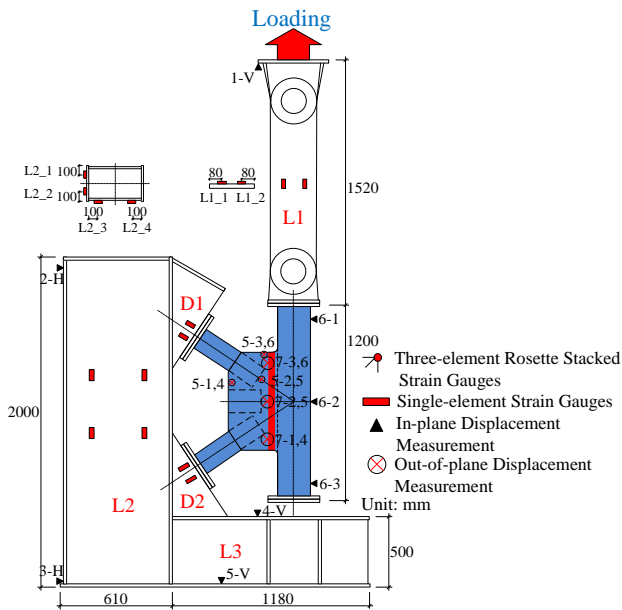


Fig. 3.5 Measured items in the link frame.

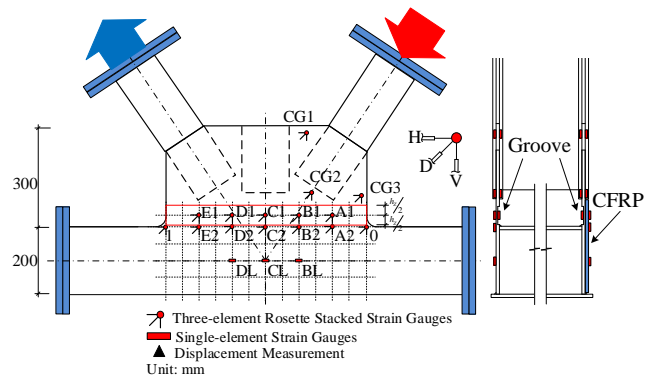


Fig. 3.6 Strain gauge locations in the gusset plate.

3.2.4. Determining the number of CFRP sheets

For the CFRP bonding method, this study considered the direction of principal stress on the gusset plate (± 45 degrees) through the experimental result and finite element method (FEM) analysis of the case without the cross-sectional loss; the direction of the diagonal member (± 56 degrees); and the direction resisting the horizontal shear stress on the corroded section (90 & 0 degrees). Therefore, the direction of CFRP sheets was interwoven at an angle of ± 45 degrees in cases of S1_45, S2_45; at an angle of ± 56 degrees in cases of S1_56, S2_56; at an angle of 90 & 0 degrees in case of S2_90; for each direction (in terms of compression and tension). The current manual related to the CFRP bonding standard^{3,12)} states that the development length of the outermost layer of the CFRP sheet should be more than 200 mm. Further, in order to avoid stress concentration

on the top of each CFRP layer, creating a shift amount of more than 10 mm (about 14 mm for the 45 degrees direction of CFRP) was necessary. However, this method was very difficult to implement in this study practically, because the length of CFRP sheets was limited by the bolts connecting the gusset plate to the diagonal members. Therefore, in this study, on the outside of the gusset plate, CFRP sheets were bonded from the areas around the diagonal members, and was extended to the edge of the welding part of the lower chord member. With this bonding method, although the development length of CFRP sheets on the upper side was insufficient, the CFRP bonding process became easier. Moreover, the shift length at the top of each CFRP layer was not implemented. Therefore, delamination between CFRP sheets and the gusset plate need to be clarified from the experimental results.

In the cases of bonding of CFRP sheets into the inner side of the gusset plate (both-sides bonding), the length of CFRP sheets also started from the areas around the diagonal member, extended to the upper flange of the chord member, and then connected between the gusset plate and the flange with an R-shape (R50), as shown in **Fig. 3.3(a2)** (b2) and (c). At this connection, CFRP sheets were extended continuously to the areas of the opposite diagonal member. The epoxy-type putty was used to fill the cross-sectional loss part. In the case of the same number of CFRP sheets, the bonding process of the both-sides bonding method usually requires much more time than that of the out-side bonding method. This is because the inside of a gusset plate has a complex shape. However, there was no major problem during this bonding process. The bonding process was completed as planned.

In this study, as a basic design method, the number of CFRP sheets had to be determined so that the corroded thickness of the gusset plate could be recovered as a healthy thickness. Therefore, the number of CFRP layers for each direction (in terms of compression and tension) was calculated such that the layers bonded to be thicker than the thickness reduced by the cross-sectional loss, which was calculated using the steel equivalent thickness of the CFRP sheet using Equation (1). The thickness of CFRP sheet of layer 1 was converted to that of steel by $0.143 \text{ (mm)} \times 640 \text{ (GPa)} / 200 \text{ (GPa)} = 0.458 \text{ (mm)}$, where 0.143 (mm), 640 (GPa), and 200 (GPa) are the design thickness, Young's modulus of CFRP sheet, and Young's modulus of steel.

Equation used to determine the number of CFRP sheets:

$$E_{cf} \times t_{cf} \times n \geq E_s \times t_{sd} \quad (3.1)$$

where, E_{cf} is the elastic modulus of CFRP sheet; t_{cf} is the thickness of a CFRP sheet; n is the necessary number

of CFRP sheets; E_s is the elastic modulus of the steel; and t_{sd} is the thickness of the cross-sectional loss part of the steel.

For example, in the case having a cross-sectional loss part of 50% of the gusset plate thickness, with $t_z = 4$ mm, the necessary number of CFRP layers for each direction with the outside bonding method was $4 \text{ mm} / 0.458 \text{ mm} = 9$ layers. For both-sides bonding, these nine layers were divided evenly between the inside and the outside. In this case, four layers were bonded on the inside and five layers were bonded on the outside, because CFRP sheet bonding on the outside is easier than that on the inside. This was calculated similar to the case with loss part 75% of the gusset plate thickness. This means that the total number of CFRP layers was $6 \text{ mm} / 0.458 \text{ mm} = 13$ layers, and there were six and seven layers on each side, respectively.

In the CFRP sheet bonding process, the first layer was for the direction of tension or compression, and the second layer for the other direction. This means that the first direction of the gusset plate bonded with the CFRP sheet was able to be tension or compression. This is because the first direction, which was bonded with CFRP sheet, did not affect the effectiveness of the repair method. The third and fourth layers were a repeat of the first layer and the second layer, respectively.

3.2.5. Process bonding CFRP sheets

Figure 3.4 depicts the construction plan and the process bonding CFRP sheets to construct smoothly and secure the required performance. For the detail of the process bonding CFRP sheets is described as the following^{3,12}.

(a) Surface preparation

Firstly, existing painting and rust on the surface should be removed by appropriate preparation methods such as blasting or disk sanding. Secondly, smears should be removed by using the organic solvent to keep the surface clean. Note that a built-up portion of welding should not be chipped off by a disk sander since it may damage the welded part.

(b) Application of the primer

Primer is applied to prevent corrosion after surface preparation, upgrading the bonding ability between the steel member and the CFRP sheets. The primer should be applied immediately after surface preparation, and after removal of rust and smear if they appear. The primer should not be applied when the surface of the steel is wet because the primer ingredient is only curable at warmer, drier temperatures. In principle, when the

temperature is lower than 5°C or humidity is higher than 85% on a rainy day, the primer should not be applied.

(c) Surface smoothing

Flatten uneven or pitted areas by using the resin putty after application of the primer, since flatness influences the bonding capability. Apply the resin putty. When covering a corner portion (inner curve), mold into an arch-like shape. Surface smoothing should be carried out after confirming the primer is dry to the touch. Other required steps such as surface cleaning, temperature, and humidity are same as the step of “Application of the primer”.

(d) Application of the primer for highly expansive elastic putty

Apply the primer for highly expansive elastic putty on the surface of the steel member and smoothing agent to secure their bond after achieving initial hardening of the smoothing agent. Other required conditions are same as the step of “Application of the primer”.

(e) Application of the highly expansive elastic putty

Confirm the primer is dry to the touch and apply the highly expansive elastic putty. Keep the thickness of the putty by design and as even as possible to obtain required repairing effect. Other required conditions are same as the step of “Application of the primer”.

(f) Application of the CFRP sheets

Place the CFRP sheets accordingly and set it in the direction required by design after the putty gains initial hardening. Other required conditions are same as the step of “Application of the primer”.

3.2.6. Measured items

a) Strain gauge location

The locations of the strain gauges are shown in **Figs. 3.5**, and **6**. Four single-element strain gauges were attached to the cross-section of each member of the link frame, in order to consider the effects of the two-axis bending moment and the axial force on them. Moreover, in order to determine the principal stress components on the cross-sectional loss part and the border line between the gusset plate and the lower chord; three-element 0°/45°/90° Rosette Stacked strain gauges were employed, as shown in **Fig. 3.6**. In the non-repaired cases, the strain gauges were attached to the inside and outside of the cross-sectional loss part. In the bonding cases of CFRP sheet, the strain gauges were attached to the inside of the cross-sectional loss part (steel), and to the outside of the CFRP sheet (**Fig. 3.6**). In addition, three-element 0°/45°/90° Rosette Stacked strain gauges were

also used at the plate area underneath the compressive diagonal member, to grasp the buckling behavior, and single-element strain gauges were used for the other locations.

b) Displacement measurement

In each loading step, vertical and horizontal displacements were measured on the members of the truss frame and the link frame, and the bottom surface of gusset plate connection, as shown in **Fig. 3.5**. In addition, the out-of-plane displacement of the gusset plate was also measured at the two outside surfaces of the gusset plate connection. These positions were labeled 7-1~7-6, as shown in **Fig. 3.5**.

3.2.7. Loading method

The loading tests were conducted in the laboratory with the link frame system for all specimens. This frame system was connected to the specimen by using bolts through the connecting plates. Further, only the specimen was changed after finishing the loading test, and the frame system was kept for the ensuing test.

SHIMADZU experimental equipment with 3000 kN capacity was used to test all specimens. The formal loading test process was only carried out after finishing the repetition about two or three times for the loading test at the elastic phase of the material.

3.3. RESULTS AND DISCUSSION

3.3.1. Improved effectiveness for maximum load

The maximum loads collected from the experiments are shown in **Table 3.4**. The max load reduction rate of the specimens was calculated as the difference between the average axial force of the two diagonal members of the frame of the cases with cross-sectional loss, and that of the case without cross-sectional loss, as in Equation (3.2). The improvement rate was taken as the difference in the average axial force of the two diagonal members between the repaired specimen and the non-repaired specimen, as in Equation (3.3).

Determining the max load reduction rate.

$$R_1 (\%) = \frac{P_{\max} - P_{\max}^0}{P_{\max}^0} \quad (3.2)$$

where, P_{\max} is the average axial force of the two diagonal members in the non-repaired case at the max load; and P_{\max}^0 is the average axial force of the two diagonal members in the intact case N at the max load.

Determining the max load improvement rate.

$$R_2(\%) = \frac{P'_{\max} - P_{\max}}{P_{\max}} \quad (3.3)$$

where, P'_{\max} is the average axial force of the two diagonal members of the repaired case at the max load; and P_{\max} is the average axial force of the two diagonal members in the non-repaired case at the max load.

From the information in **Table 3.4**, the load-carrying capacity of the non-repair case S reduced significantly compared to the intact case N by 20.3%. Furthermore, in the repaired cases bonding CFRP sheets in the direction of 45 degrees and 56 degrees, their load-carrying capacity increased only slightly, with improvement rates of 0.3% to 11.1%. This is because the peeling failure between CFRP sheets and the gusset plate occurred under the large out-of-plane deformation of buckling, which occurred at the plate area underneath the diagonal member of the gusset plate connection and the free edge of the gusset plate. Moreover, with the bonded CFRP-sheet direction of 45 degrees and 56 degrees, the effectiveness of CFRP sheets resisting the horizontal shear stress of the Groove section, which decided the final load-carrying capacity of the corroded gusset plate connection, is not considerable. Meanwhile in the case of S2_90, by bonding CFRP sheets in the direction of 90 degrees, its load-carrying capacity recovered to that of the intact case with the improvement rate of 19.7%. This is understood that bonding CFRP sheets with the purpose of increasing the horizontal shear strength of the Groove section significantly increased the final load-carrying capacity of the corroded gusset plate connection.

From the experimental results, the reduction of the load-carrying capacity of the gusset plate connection owing to the corrosion is clarified. Further, the proposed repair method by bonding CFRP sheets in the direction of 90 degrees recovered the load-carrying capacity of the corroded gusset plate connection.

Table 3.4 Maximum load and improvement rate.




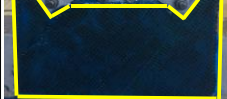

No.	Specimen	Maximum load (kN)	Maximum load reduction rate $R_1(\%)$	Maximum load improvement rate $R_2(\%)$	CFRP bonding method			
					The direction of bonding CFRP sheets	The area of bonding CFRP sheets	The location of bonding CFRP sheets	Number of CFRP (layer)
1	N	1634	–	–	No repair			
2	S	1303	20.3	–	No repair			
3	S1_45	1448	–	11.1	$\pm 45^\circ$		Out side	9 outer (each direction)
4	S2_45	1348	–	3.5			Both sides	4 inner + 5 outer (each direction)
5	S1_56	1314	–	0.8	$\pm 56^\circ$		Out side	9 outer (each direction)
6	S2_56	1387	–	6.4			Both sides	4 inner + 5 outer (each direction)
7	S2_90	1560	–	19.7	90° & 0°		Both sides	4 inner + 5 outer (each direction)

Table 3.5 Strength of gusset plate connections (AASHTO).

Limit State of Gusset Plate Connection	Loading value (kN)	Loading value (kN)	
		N	S
1a - Shear fracture strength of bolts	P_{ru}	2897	–
1b - Block shear rupture strength of bolts	P_{ru}	3203	–
2a - Cross section yielding strength of gusset plate at the closest bolt part	P_{gy}	2221	–
2b - Net section fracture resistance of gusset plate at the closest bolt part	P_{gu}	2881	–
3 - Block shear rupture strength in tension	P_{gbs}	2415	–
4a - Cross section yielding strength of diagonal member	P_{dv}	2184	–
4b - Net section fracture strength of diagonal member	P_{du}	2734	–
5 - Compressive strength (Buckling at the plate area underneath diagonal member)	P_{gr}	1131	–
6 - Shear fracture strength of gusset plate	V_{gsy}	1581	791

The process calculating the strengths of the gusset plate connection is described in **APPENDIX**.

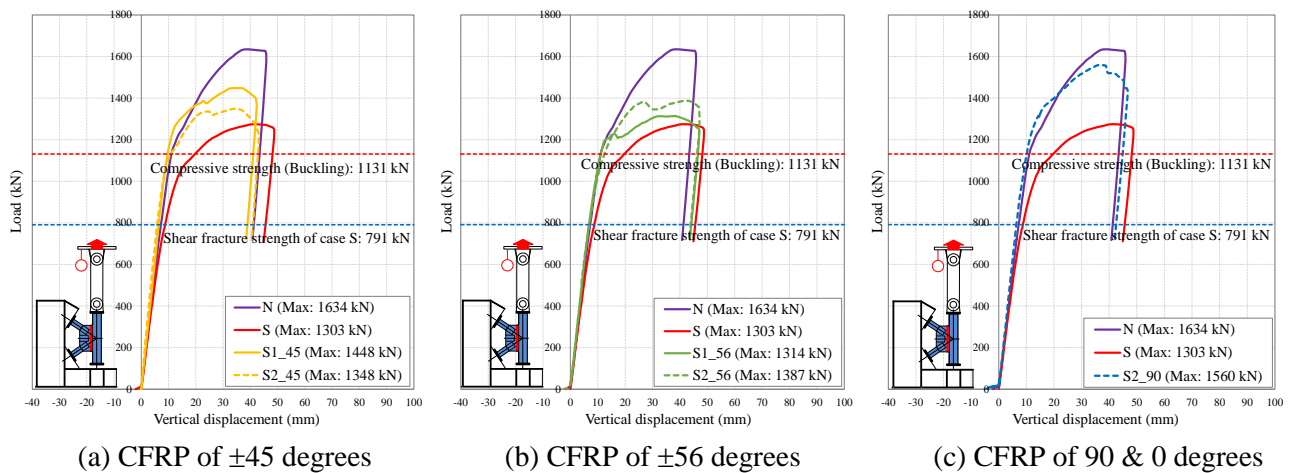


Fig. 3.7 Load-Vertical displacement relation.

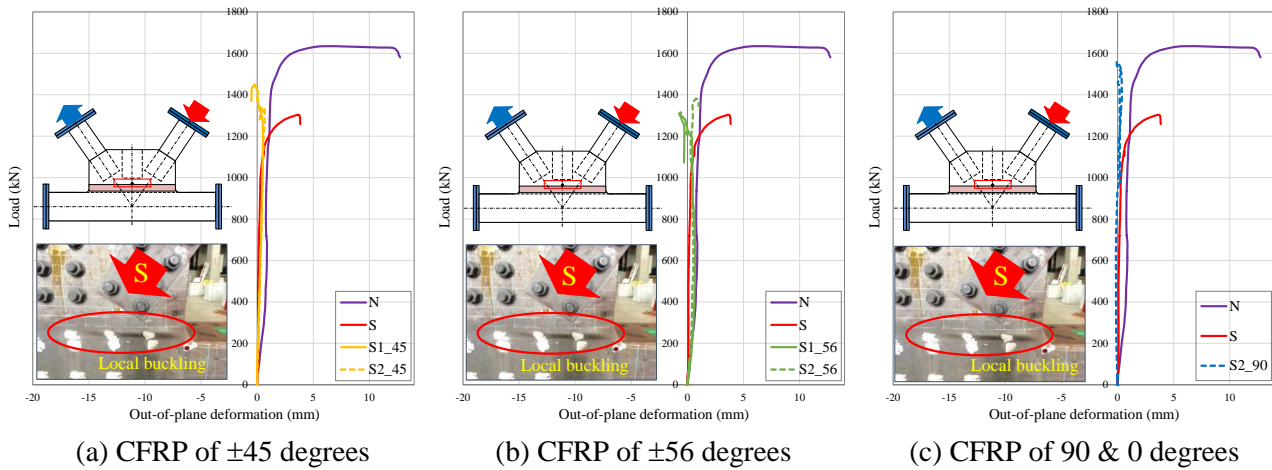


Fig. 3.8 Load-Out-of-plane deformation relation.

3.3.2. Improved effectiveness for deformation

a) Load and vertical displacement relation

The strength of the gusset plate connection was determined as the resistance ability of the gusset plate to compression, shear, and tension. In this study, calculating the strength of the gusset plate connection was conducted by using the load rating guidance for bolted and riveted gusset plates in truss bridges, as suggested by AASHTO^{3,20}. In particular, the buckling strength (compressive strength) at the plate area underneath the diagonal member of the gusset plate connection was calculated by referring to ref. 3.21. This calculation process is described in **APPENDIX**. In addition, the strength of the gusset plate connection is summarized in **Table 3.5**.

The relations between load and vertical displacement at the highest point of the tensile link member of the link frame in all specimens are shown in **Fig. 3.7**. The red and blue dashed lines in **Fig. 3.7** express the compressive strength and shear fracture strength of the gusset plate connection, which are summarized in **Table 3.5**. In the non-repaired specimens S with the corrosion level of 50% of the gusset plate thickness, there was almost no change of the initial stiffness. Further, in the repaired cases, buckling at the plate area underneath diagonal member occurred at the load of approximately 1100 kN in the specimens of S1_45 and S2_45, in which the CFRP sheets were not added to the free edges of the gusset plate; and at the load of approximately 1200 kN in the specimens of S1_56, S2_56, and S2_90, in which the CFRP sheets were added to the free edges of the gusset plate (this point is clarified in Section 3.3.4). The vertical displacement of the specimens in-

creased linearly until buckling occurred at the diagonal member. After overcoming the buckling load, the load-displacement curve trend changed.

As a result, there was virtually no change in the initial stiffness of the case with the corrosion level of 50% of the gusset plate thickness.

b) Load and out-of-plane deformation relation

The relations between the load and out-of-plane deformation on the central point of the gusset plate are shown in **Fig. 3.8**. In **Fig. 3.8**, the out-of-plane deformation of the intact case N is large only in the phase with virtually maximum load. This is due to the influence of large deformation induced by buckling at the plate area underneath the compressive diagonal member.

In the non-repaired case S, the out-of-plane deformation is large. This is because of the influence of the local buckling at the Groove section. However, with the proposed methods bonding CFRP sheets, its out-of-plane stiffness increased substantially, and local buckling is prevented at the Groove area. This is clearly seen through the out-of-plane deformation of Cases S1_45, S2_45, S1_56, S2_56, and S2_90, as shown in **Fig. 3.8**. These results confirm that the proposed CFRP bonding methods are able to recover the out-of-plane stiffness of the corroded gusset plate.

3.3.3. Improved effectiveness for eccentricity moment on the corroded section

Figure 3.9 shows the relations between the load and strain on the inner surface of the Groove section in the diagonal direction in all of specimens without and with repair. From the information of **Fig 3.9**, in the non-repaired case S, the strain on the inner surface of the Groove section in the diagonal direction is large. This is understood to be the result of eccentricity due to the decreased thickness of the Groove section, causing a significant increase in the bending moment in the compressive direction. Furthermore, in the outside bonding cases of S1_45 and S1_56, because of the eccentric nature of the cross-sectional loss part, the strain of the loss part has reached a large value even under a low loading value. However, by bonding CFRP sheets to both-sides of the gusset plate in the cases of S2_45, S2_56, and S2_90; the bending moment in the compressive direction of the Groove section due to the eccentricity was improved considerably compared to the cases (S1_45, and S2_56) bonding the CFRP sheets to only outside of the gusset plate. This information was clarified through the relation between the load and the strain on the inner surface of the Groove section repaired, as shown in **Fig. 3.9**.

As a result, the repair methods bonding CFRP sheets into both-sides of the corroded gusset plate are able to improve the bending moment in the compressive direction of the corroded section owing to the eccentricity.

3.3.4. Failure condition

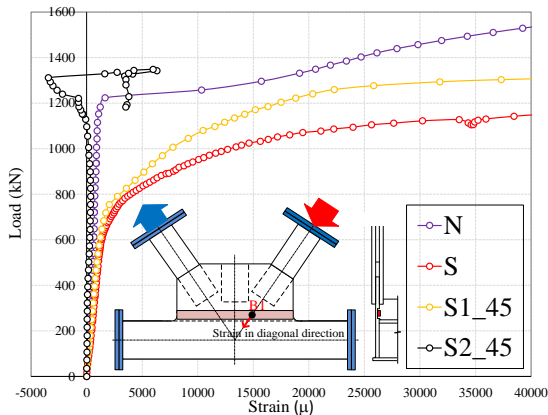
Figure 3.10 shows the residual deformation of the specimens after the loading test, and **Table 3.6** lists all of the failure conditions on the gusset plate in each case in order. In the intact case N with the link frame, the first failure condition was buckling at the plate area underneath the diagonal member from 1100 kN. This was clarified through the relation between the load and the bending strain of the plate area underneath the compressive diagonal member, as shown in **Fig. 3.11(a)**. On the other hand, the load causing buckling in this plate area was similar to the non-repaired case S; and the repaired cases S1_45, and S2_45 (see **Fig. 3.11(b)** and (c)), in which CFRP sheets were not attached to the area around the diagonal member. Further, the load-carrying capacity of the intact case N reached the maximum value after the large out-of-plane deformation occurred at the plate area underneath the compressive diagonal member owing to buckling.

In the non-repaired case S, local buckling appeared at the Groove section for 801 kN. This is understood to be as a result of eccentricity, due to the decreased thickness of the Groove section, which caused a significant increase in the bending moment in the compressive direction of the Groove section. This point clarified through the relation between the load and bending strain on the Groove section, as shown in **Fig. 3.12**. The final failure condition in this case was the shear fracture at the Groove section.

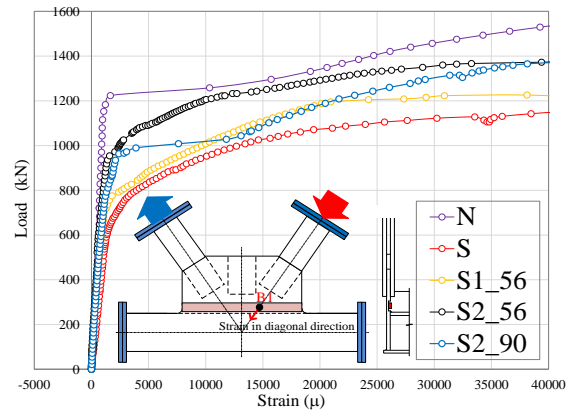
On the other hand, using CFRP sheets bonding method increased the out-of-plane stiffness of the gusset plate. Consequently, in all of the repaired cases, local buckling on the Groove section did not occur. Moreover, by bonding CFRP sheets to both sides of the gusset plate in the cases of S2_45, S2_56, and S2_90; the bending moment in the compressive direction of the Groove section due to the eccentricity was improved considerably compared to the cases (S1_45, and S2_56) bonding CFRP sheets to only outside of the gusset plate. This information was clarified through the relation between the load and the strain on the inner surface of the Groove section, as described in Section **3.3.3**.

In cases added CFRP sheets to the area around the diagonal member such as cases of S1_56, S2_56, and S2_90; the plate area underneath the diagonal member was reinforced by CFRP sheets, so the buckling load on this area was grown up by 10%, compared to the cases of S1_45, and S2_45.

Figure 3.13 shows the relations between load and von Mises stress on the outermost CFRP sheet of the locations, in which the first delamination between CFRP sheet and the gusset plate occurred. The first delamination appeared at the Groove section for specimens S1_45 and S2_45; at the areas around the diagonal members for specimens S1_56, S2_56 and S2_90. In **Fig. 3.13**, the red horizontal line indicates the load (delamination load), which caused delamination between CFRP sheets and the gusset plate. The delamination load was determined at the loading value, with the stress on the outermost CFRP sheet substantially lower. The delamination load was approximately equal to the max load in each case. This confirms that the delamination occurred between CFRP sheets and the gusset plate, the load-carrying capacity of the specimens could not increase beyond that point. In short, although the low elastic putty material was applied, delamination occurred between CFRP sheets and the gusset plate. Specifically, under the large out-of-plane deformation of the free edge of the gusset plate during compression and the very large out-of-plane stiffness of CFRP sheets, deformation of the putty layer exceeded its plastic limit. Therefore, CFRP sheets and the gusset plate were rapidly delaminated. The final status in all of the repaired cases was the delamination of CFRP sheets and shear fracture at the Groove section.



(a) S1_45 and S2_45



(b) S1_56, S2_56, and S2_90

Fig. 3.9 Load-Strain relation on the inner surface of the Groove section in the diagonal direction.

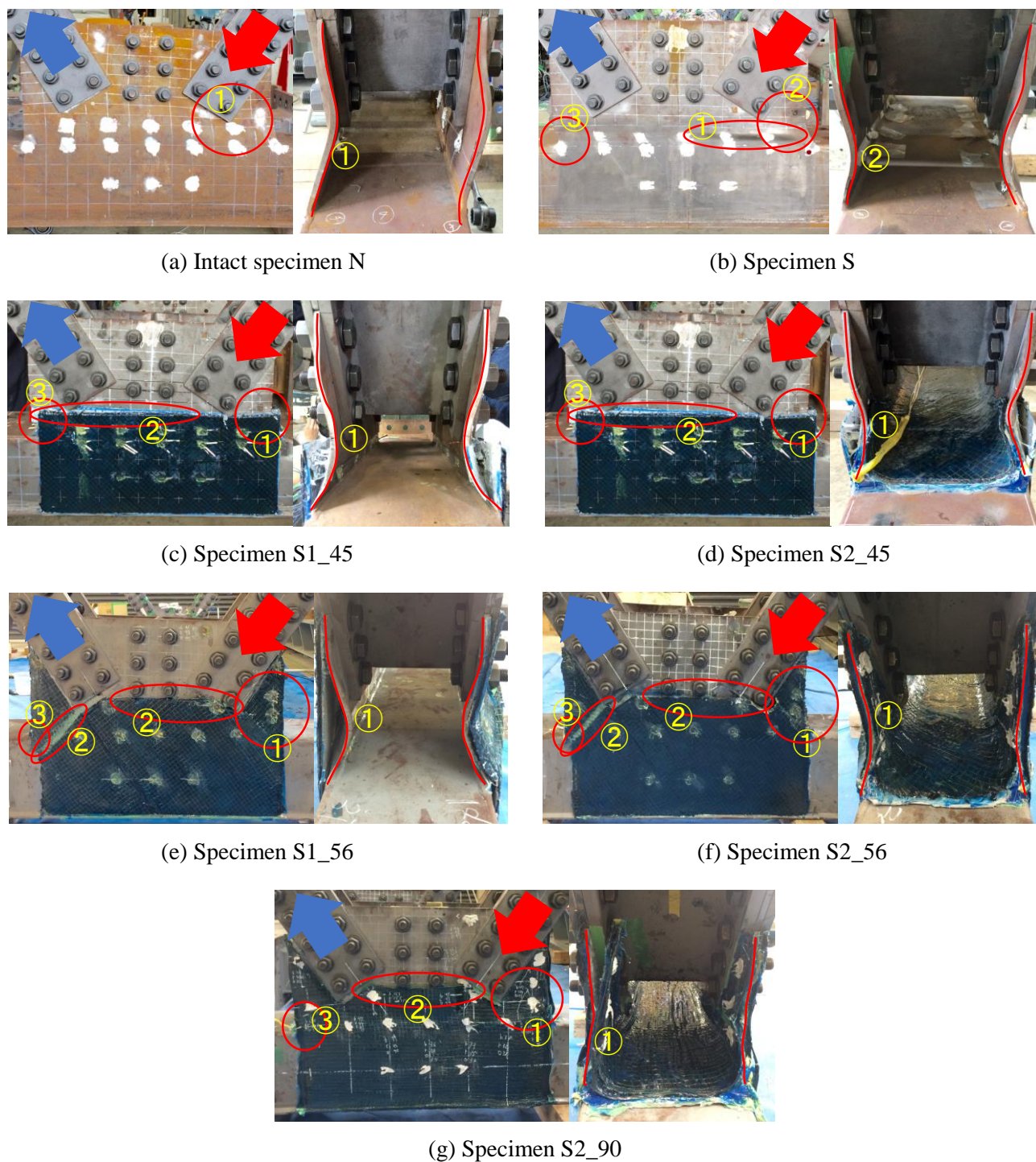
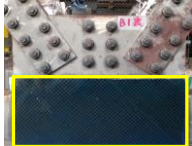
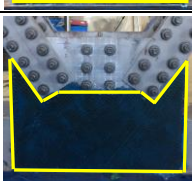
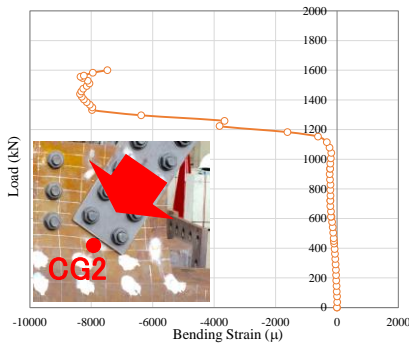


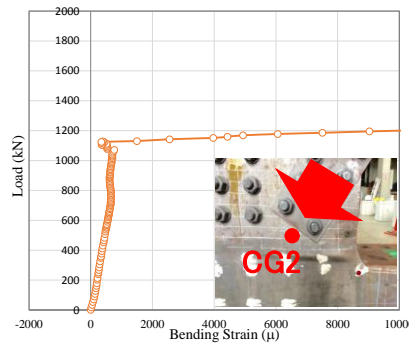
Fig. 3.10 Final shape of the specimens.

Table 3.6 Summary of failure conditions on the gusset plate.

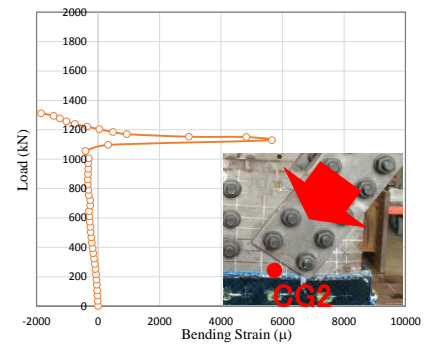
No.	Specimen	Local buckling at Groove section (kN)	Buckling at the plate area underneath diagonal member (kN)	Delamination between CFRP sheet and the gusset plate (kN)	Final failure condition	Maximum load (kN)	The area bonding CFRP sheets
1	N	–	1100	–	Large out-of-plane deformation	1634	–
2	S	801	1086	–	Shear fracture at Groove section	1303	–
3	S1_45	–	1080	1386		1448	
4	S2_45	–	1096	1329		1348	
5	S1_56	–	1205	1224		1314	
6	S2_56	–	1196	1250		1387	
7	S2_90	–	1184	1450		1560	



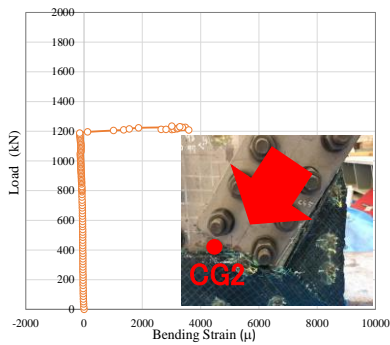
(a) Intact specimen N



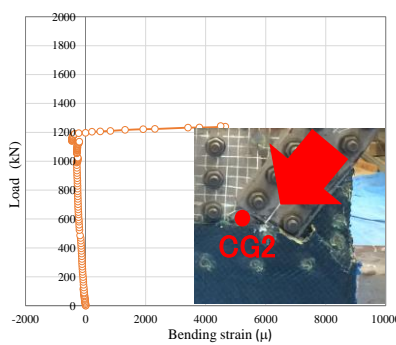
(b) Specimen S



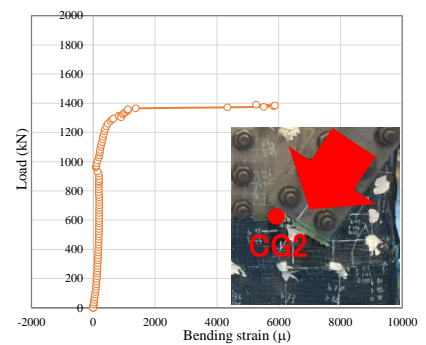
(c) Specimen S2_45



(d) Specimen S1_56

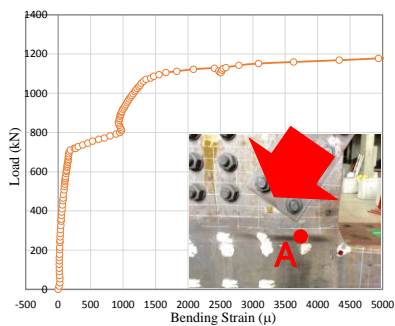


(e) Specimen S2_56

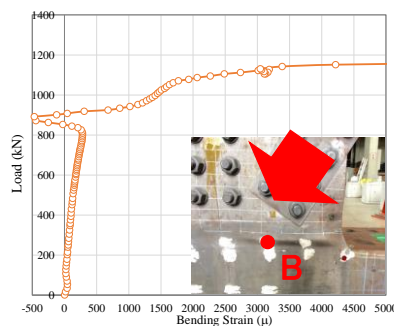


(f) Specimen S2_90

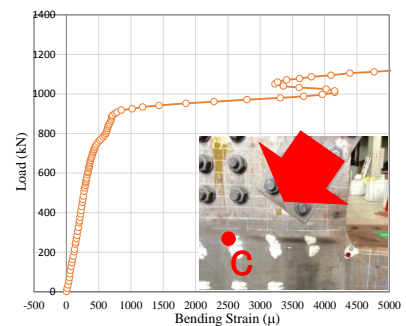
Fig. 3.11 Load-bending strain relation at the plate area underneath the diagonal member.



(a) Location A



(b) Location B



(c) Location C

Fig. 3.12 Load-bending strain relationship of Specimen S.

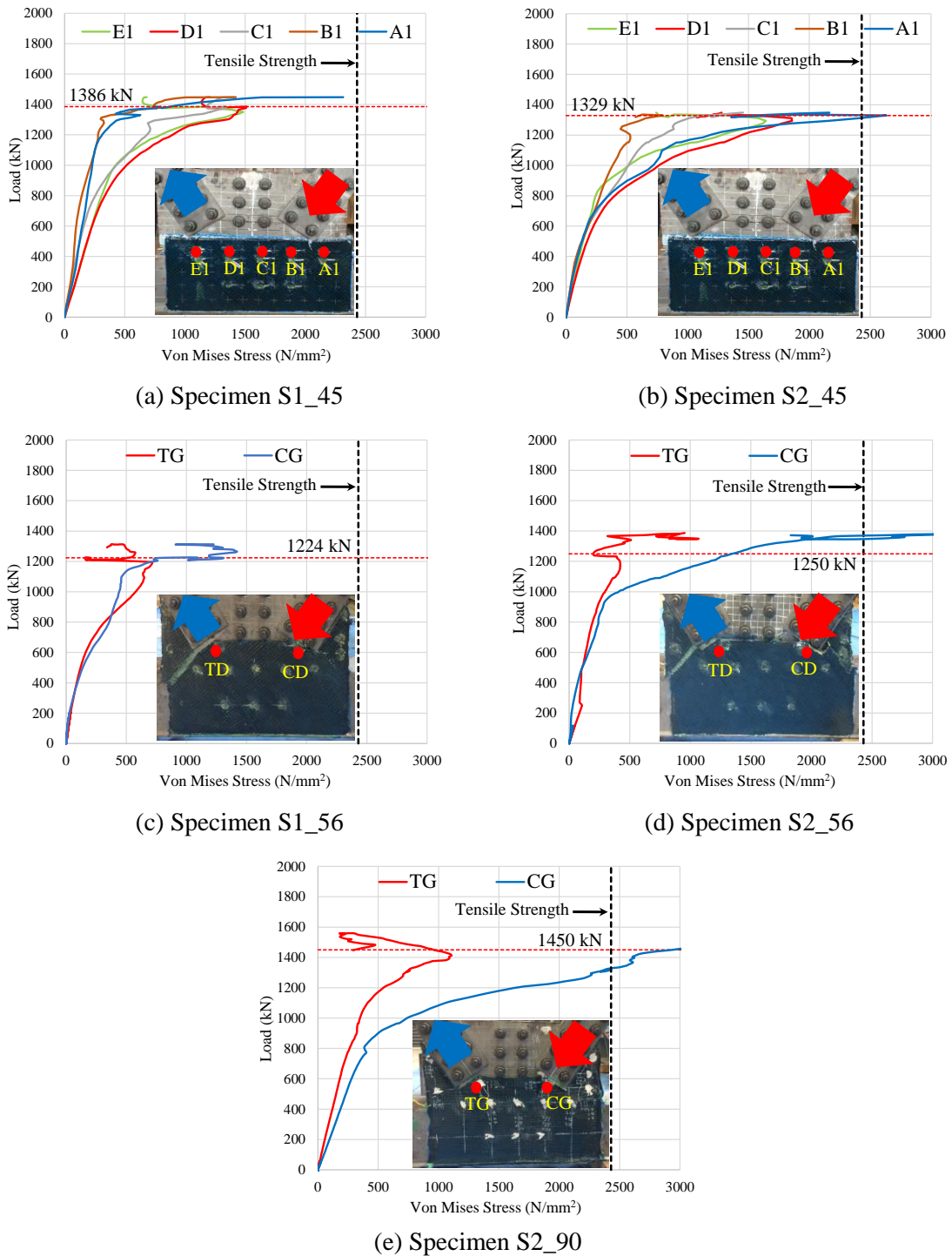


Fig. 3.13 Load-Von Mises stress on CFRP sheet.

3.4. CONCLUSION

This study proposed the repair methods using carbon fiber-reinforced polymer (CFRP) for corroded gusset plate connections after investigating their effectiveness, with three parameters: including the area of the bonded CFRP sheets; the direction (± 45 degrees: the direction of principal stress on the gusset plate, ± 56 degrees: the direction of the diagonal member, 90 & 0 degrees: the direction resisting the horizontal shear

stress on the corroded section) of the bonded CFRP sheets; and the location of the bonded CFRP sheets (out-side bonding and both-sides bonding). Evaluations were conducted by implementing the five bonding methods with CFRP sheets, and evaluating the improvement rate of the load-carrying capacity of the corroded gusset plate. Loading tests in the laboratory with a model approximately 50% the size of the actual bridge, and the degree of corrosion assumed approximately 50% of the gusset plate thickness, were conducted. The results obtained from this study are summarized as the following:

(1) The reduction of the load-carrying capacity of the gusset plate connection due to the corrosion level of 50% of the gusset plate thickness, is clarified with the reduction rate of 20.3%.

(2) The proposed repair methods using CFRP sheets were able to improve the load-carrying capacity of the corroded gusset plate connection with the improvement rate in the range of 0.8% to 19.7%. While, the method bonding CFRP sheets in the direction of 90 degrees recovered the load-carrying capacity of the corroded gusset plate connection to virtually the same as that of the intact case. This is understood that the method bonding CFRP sheets with the direction of 90 degrees achieved the better effectiveness in resisting the horizontal shear stress of the corroded section, which decided the final load-carrying capacity of the corroded gusset plate connection, compared to other methods.

(3) The experimental results provided that there was virtually no change in the initial stiffness of the gusset plate connection with the corrosion level of 50% of the gusset plate thickness. However, the significant increase of the out-of-plane deformation of the corroded gusset plate was seen because the local buckling on the corroded section occurred. This is understood to be as a result of eccentricity, due to the decreased thickness of the corroded section. On the other hand, by using the proposed repair methods, the out-of-plane deformation of the corroded gusset plate connection was prevented completely. Therefore, in all of the repaired cases, local buckling on the corroded section did not occur.

(4) For all of the proposed repaired methods; in the both-sides bonding methods, the bending moment in the compressive direction of the corroded section due to eccentricity was improved considerably compared to the out-side bonding methods.

(5) In the repair methods added CFRP sheets to the area around the diagonal member of the gusset plate connection; the plate area underneath the diagonal member was reinforced by CFRP sheets, so the buckling load on this area was grown up by 10%, compared to the other methods.

APPENDIX: CALCULATING STRENGTH OF GUSSET PLATE CONNECTION (AASHTO)

In this study, calculation of the strength of the gusset plate connection was conducted by using the load rating guidance of the gusset plate, as suggested by AASHTO^{3,20}. In particular, the buckling strength (compressive strength) at the plate area underneath the diagonal member of the gusset plate connection was calculated in accordance with ref. 3.21. The limit state of the gusset plate and the diagonal members of the gusset plate connection were assumed as follows, and shown in **Fig. 3.14**. This calculation process is shown in **Table 3.7**.

- 1) Strength of fasteners in compression, tension
- 2) Cross-section yielding or net section fracture resistance of gusset plate
- 3) Block shear rupture strength in tension
- 4) Cross-section yielding or net section fracture strength of diagonal member
- 5) Compressive strength
- 6) Shear fracture strength

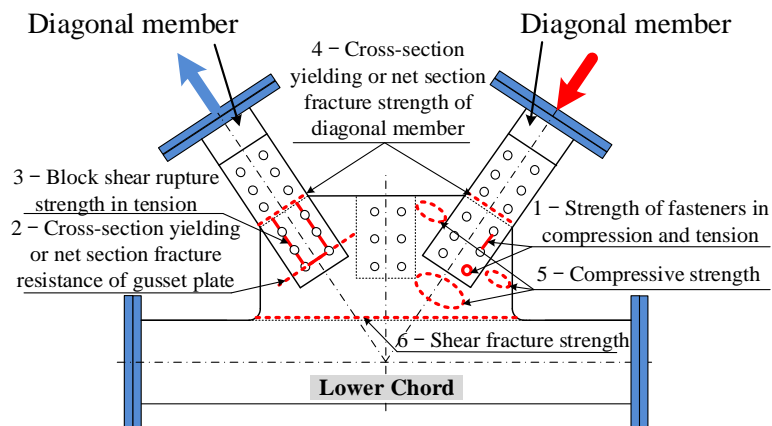


Fig. 3.14 Limit state of the gusset plate connection.

Table 3.7 Calculating the strength of the gusset plate connection (AASHTO).

Limit state of gusset plate connection	Structural parameters		Calculated value	
			N	S
1a - Shear fracture strength of bolts $P_{ru} = \frac{1}{\sqrt{3}} f_u n A_r$	f_u : Tensile strength of bolt (M20(F10T)) (MPa)		1100	1100
	A_r : Cross-sectional area of bolt ($\phi = 22$) (mm ²)		380.1	380.1
	n : The number of shear planes		6	6
	P_{ru} : Shear fracture strength of bolts (kN)		2897	2897
1b - Block shear rupture strength of bolts $P_{ru} = L_c t f_u$	ΣL_c : Clear distance between holes (mm)		438	438
	t : Thickness of gusset plate (mm)		8	8
	f_u : Tensile strength of gusset plate (SS400) (MPa)		457	457
	P_{ru} : Block shear rupture strength of bolts (kN)		3203	3203
2a - Cross-section yielding strength of gusset plate at the closest bolt part $P_{gy} = A_e f_y$	L_e : Whitmore width (mm)		438.0	438.0
	t : Thickness of gusset plate (mm)		8	8
	A_e : Gross cross-sectional area of Whitmore effective width of gusset plate (mm ²)		3503.7	3503.7
	f_y : Yield strength of gusset plate (SS400) (MPa)		317	317
	P_{gy} : Cross-section yielding strength of gusset plate at the closest bolt part (kN)		2221	2221
2b - Net section fracture resistance of gusset plate at the closest bolt part $P_{gu} = A_s f_u$	L_e : Whitmore width (mm)		438.0	438.0
	t : Thickness of gusset plate (mm)		8	8
	A_s : Net cross-sectional area of Whitmore effective width of gusset plate (mm ²)		3151.7	3151.7
	f_u : Tensile strength of gusset plate (SS400) (MPa)		457	457
	P_{gu} : Net section fracture resistance of gusset plate at the closest bolt part (kN)		2881	2881
3 - Block shear rupture strength in tension $P_{gbs} = \frac{1}{\sqrt{3}} f_y A_{vg} + f_u A_{tm}$	A_m : Net cross-sectional area along the plane resisting tension stress (mm ²)		464	464
	A_{tg} : Gross cross-sectional area along the plane resisting tension stress (mm ²)		640	640
	A_{vm} : Net cross-sectional area along the plane resisting shear stress (mm ²)		3808	3808
	A_{vg} : Gross cross-sectional area along the plane resisting shear stress (mm ²)		5920	5920
	f_y : Yield strength of gusset plate (SS400) (MPa)		317	317
	f_u : Tensile strength of gusset plate (SS400) (MPa)		457	457
	P_{gbs} : Block shear rupture strength in tension (kN)		2415	2415
4a - Cross-section yielding strength of diagonal member $P_{dy} = f_y A_g$	A_g : Gross cross-sectional area of diagonal member (mm ²)		5983	5983
	f_y : Yield strength of gusset plate (SM490Y) (MPa)		365	365
	P_{dy} : Cross-section yielding strength of diagonal member (mm ²)		2184	2184
4b - Net section fracture strength of diagonal member $P_{du} = f_u A_s$	A_s : Net cross-sectional area of diagonal member (mm ²)		5983	5983
	f_u : Tensile strength of gusset plate (SM490Y) (MPa)		457	457
	P_{du} : Net section fracture strength of diagonal member (kN)		2734	2734
5 - Compressive strength (Buckling at the area underneath diagonal member) $P_{gr1} = f_y A_0 \quad (\bar{\lambda} \leq 1.0)$ $P_{gr1} = \frac{1}{\bar{\lambda}^2} f_y A_0 \quad (1.0 < \bar{\lambda})$ $P_{gy1} = f_y A_1 \sin \theta_1$ $P_{gy2} = f_y A_2 \sin \theta_2$ $P_{gr} = P_{gr1} + P_{gy1} + P_{gy2}$	L_0 : Width of diagonal member (mm)		80	80
	t : Thickness of gusset plate (mm)		8	8
	A_0 : Gross cross-section area of diagonal width (mm ²)		640	640
	I_g : Moment of inertia (mm ⁴)		3413.3	3413.3
	r_g : Radius of gyration about the plane of buckling (mm)		2.3	2.3
	L_c : The distance from center of the width of diagonal end to the edge of the closest adjacent member (mm)		159.1	159.1
	β : effective length factor		0.65	0.65
	$\bar{\lambda}$: The column slenderness ratio		0.6	0.6
	f_y : Yield strength of gusset plate (SS400) (MPa)		317	317
	P_{gr1} : Local buckling at unbraced area underneath diagonal (kN)		405.8	405.8
	A_1 : Cross-sectional area of 1 free edge section (mm ²)		1375.7	1375.7
	A_2 : Cross-sectional area of 2 free edge section (mm ²)		2063.5	2063.5
	P_{gy1} : Cross-section yielding strength of free edge area (kN)		362.8	362.8
	P_{gy2} : Cross-section yielding strength of free edge area (kN)		362.8	362.8
P_{gr} : Compressive strength (kN)		1131	1131	
6 - Shear fracture strength of gusset plate $V_{gsy}^0 = \frac{1}{\sqrt{3}} f_y A_g$	A_g : Gross cross-sectional area along the plane resisting shear stress (mm ²)		4800	2400
	f_y : Yield strength of gusset plate (SS400) (MPa)		317	317
	V_{gsy}^0 : Shear fracture strength of gusset plate (kN)		1757	878

REFERENCES

- 3.1) National Transportation Safety Board: Collapse of I-35W highway bridge Minneapolis, Minnesota, Accident report, NTSB/HAR-08/03, PB2008-916203, August 2007.
- 3.2) Hatano, H., Murakami, S., Rokugou, Y. and Yoda, T.: Summary of NTSB report on I-35W bridge in Minneapolis, *Bridge and Foundation*, pp. 37-42, 2010.7.
- 3.3) Kasano, H. and Yoda, T.: Collapse mechanism and evaluation of node damages of I-35W Bridge, Minneapolis, USA, *Proceedings of Japan Civil Engineering Association-A*, Vol. 66, No. 2, pp. 312-323, 2010 (in Japanese).
- 3.4) Astaneh-Asla, A.: Progressive collapse of steel truss bridges, the case of I-35W collapse, *Invited Keynote Paper, Proceedings of the 7th International Conference on Steel Bridges*, University of California, Berkeley, USA, pp.1-10, 4-6 June 2008.
- 3.5) Manda, A. and Nakamura, S.: Progressive collapse analysis of steel truss bridges, *Proc. Schl. Eng. Tokai Univ.*, Ser. E, Vol. 35, pp. 27-34, 2010.
- 3.6) Nguyen, X. T., Nogami, K., Yoda, T., Kasano, H., Murakoshi, J., Honda, H. and Tashiro, D.: Evaluation of corrosion at contact surface on gusset plate connections of steel truss bridge, *Proceedings of the 22nd Steel Structure*, Article No. 85, pp. 161-171, 2015.
- 3.7) Murakoshi, J., Arimura, K., Sawada, M., Toyama, N., Yoda, T., Nogami, K. and Kasano, H.: Field loading test and loading-capacity evaluation of a corroded steel truss bridge, *Journal of Structural Engineering*, Vol. 59, pp.736-746, 2013.3 (in Japanese).
- 3.8) Nguyen, X. T., Nogami, K., Yoda, T., Kasano, H., Murakoshi, J., Honda, H. and Tashiro, D.: Evaluation of corrosion state of gusset plate connections of steel truss bridge, *Proceedings of the 21st Steel Structure*, Article No. 83, pp. 71-83, September 2014.
- 3.9) Bridge repair manual (revised in 2003) 3 - 3 Steel member (in Japanese).
- 3.10) ACI-440, 2008: Guide for the design and construction of externally bonded FRP systems for strengthening concrete structures, American Concrete Institute.
- 3.11) FRP in China: The state of FRP research, design guidelines and application in construction, *FRP Composites in Civil Engineering – CICE 2004*.

- 3.12) Nippon Expressway Research Institute: Repair and reinforcement method for corroded steel members by using CFRP sheet, October 2013 (in Japanese).
- 3.13) Nagai, M., Hidekuma, Y., Miyashita, T., Okuyama, Y., Kudo, A. and Kobayashi, A.: Bonding characteristics and flexural stiffening effect of CFRP strand sheets bonded to steel beams, *Procedia Engineering*, Vol. 40, pp. 137–142, 2012.
- 3.14) Hidekuma, Y., Miyashita, T., Okuyama, Y., Ishikawa, T. and Kobayashi, A.: Repairing method for steel member with cross-section loss by CFRP bonding, *IABSE Symposium Report*, Vol. 104, No. 12, pp. 1-5, 2015.
- 3.15) Wakabayashi, D., Miyashita, T., Okuyama, Y., Nagai, M., Koide, N., Kobayashi, A., Hidekuma, Y. and Horimoto, W.: Experimental study on repair and reinforcement method for web in steel girder bridge using FRP, *the 9th Symposium on Research and Application of Hybrid Structures*, pp. 371-378, 2011 (in Japanese).
- 3.16) Miyashita, T. and Nagai, M.: Repair method for corroded steel girder ends using CFRP sheet, *IABSE-JSCE Joint Conference on Advances in Bridge Engineering-III*, 21-22 August, 2015, Dhaka, Bangladesh.
- 3.17) Okuyama, Y., Miyashita, T., Wakabayashi, D., Hidekuma, Y., Kobayashi, A., Koide, N., Horimoto, W. and Nagai, M.: A study on optimum design method of repair and reinforcement method using carbon fiber sheets for corroded web in steel girder bridge, *Proceedings of Structural Engineering*, Vol. 60A, pp. 541–553, March 2014 (in Japanese).
- 3.18) Wakabayashi, D., Miyashita, T., Okuyama, Y., Kobayashi, A. and Hidekuma, Y.: Repair method using CFRP for corroded steel girder ends, *Fourth Asia-Pacific Conference on FRP in Structures (APFIS 2013)*, pp.1-6, 11-13 December 2013.
- 3.19) Miyashita, T., Wakabayashi, D., Hidekuma, Y., Kobayashi, A., Okuyama, Y., Koide, N., Horimoto, W. and Nagai, M.: CFRP repair method for corroded steel girder ends, *IABSE Symposium Report*, Vol. 104, No. 12, pp. 1-7, August 2015.
- 3.20) Federal Highway Administration: Load rating guidance and examples for bolted and riveted gusset plate in truss bridges, Publication No. FHWA-IF-09-014, 2009.

- 3.21) Murakoshi, J., Tashiro, D., Enomoto, T., Nogami, K., Yoda, T. and Kasano, H.: Study on evaluation equation for local buckling strength of gusset plate connection in truss bridge, *JSCE 69th Annual Conference*, pp. 1223-1224, 2014.9 (in Japanese).
- 3.22) Miyashita, T., Iwasaki, E., Nagai, M. and Khanh, T. D.: On-site loading test and short-term monitoring for Gerber steel truss bridges being used for 76 years, *Journal of Structural Engineering*, Vol. 61A, pp. 439-450, 2015 (in Japanese).
- 3.23) Okuyama, Y., Miyashita, T., Ogata, T., Ohgaki, K., Hidekuma, Y., Horimoto, W. and Nagai, M.: Mechanical behavior of plate bonded FRP sheets under uniaxial compression load, *Proceedings of the 3rd Asia Pacific Conference on FRP*, p. 13, 2012.
- 3.24) Potyrala, P. B.: Use of fibre reinforced polymer composites in bridge construction. State of the art in hybrid and all-composite structures, Doctoral dissertation, Universitat Politècnica de Catalunya. Escola Tècnica Superior d'Enginyers de Camins, Canals i Ports de Barcelona, 2011.
- 3.25) Tamon, U.: FRP for construction in Japan, *Joint Seminar on Concrete Engineering, Mongolia*, pp.1-15, May 2005.
- 3.26) Wang, H., Wu, G. and Wu, Z.: Effect of FRP configurations on the fatigue repair effectiveness of cracked steel plates, *Journal of Composites for Construction*, 10.1061/ (ASCE) CC.1943-5614.0000422, 04013023, pp.1-11, 2013.
- 3.27) Wang, H., Wu, G. and Jiang, J.: Fatigue behavior of cracked steel plates strengthened with different CFRP systems and configurations, *Journal of Composites for Construction*, 10.1061/ (ASCE) CC.1943-5614.0000647, 04015078, pp.1-9, 2015.
- 3.28) Japan Road Association: Specification for highway bridges, Part-2 Steel Bridges, Tokyo, Maruzen Publication, 2012 (in Japanese).
- 3.29) Manie, J. and Kikstra, W. P.: DIANA Finite Element User's Manual, Analysis Procedures (release 9.6), TNO DIANA b.v., 2016.

CHAPTER 4

FINITE ELEMENT ANALYSIS OF GUSSET PLATE CONNECTION BONDING CFRP SHEETS

4.1. INTRODUCTION

The applicability of carbon fiber-reinforced polymers (CFRP) as materials for repairing and strengthening aging or damaged structures is being intensively investigated worldwide, typically for example in the USA from the 1970s, or in Japan and China from the 1980s. CFRP in sheet form is usually applied to repair and strengthen steel structures which have reduced load-carrying capacity due to natural hazards, human errors, accidents, corrosion damages, and fatigue damage. In particular, to maximize the effectiveness of repair and reinforcement methods using CFRP sheets, and to prevent the peeling failure of CFRP layers under large deformations such as buckling, polyurea putty with a low elastic modulus (54.7 MPa) and high elongation (300%-500%) is usually inserted between steel members and CFRP sheet. Therefore, it is clear that maximum strength of steel members repaired or reinforced is often determined by the peeling failure of the interface between structural member and CFRP sheet. For this reason, in order to perform the most effective repair and reinforcement; it is necessary to grasp the mechanical behavior, the peeling mechanism and the peeling strength of adhesion layer inserted between steel member and CFRP sheet. However, previous studies proposed linear theoretical analysis to determine the peeling strength of adhesion layer by calculating the principal stress on adhesion layer, and there is no study in which nonlinear analysis has been mentioned. Moreover, even in finite element analysis, modeling is difficult because the thickness of CFRP sheets and adhesive layer are so thin. There is almost no research on an analysis method that fully considers the orthotropic material properties of CFRP sheets and material model (shear direction and normal direction) of adhesion layer.

Therefore, Chapter 4 established a nonlinear theoretical analysis method considering the peeling condition of adhesion layer, and the nonlinear material condition of all members on an analytical model; for a steel plate bonding a layer of CFRP sheet under uniaxial tensile loading. Moreover, after grasping the peeling mechanism of adhesion layer from the proposed nonlinear theoretical analysis, finite element analyses were implemented

on the repaired gusset plate connection to reproduce the experimental results obtained in Chapter 3. Finally, a parametric analysis was carried out on the repaired gusset plate connection by varying the number of bonding CFRP sheets calculated from the equation of steel conversion, to clarify the necessary number of CFRP sheets bonding into the corroded gusset plate.

4.2. THEORETICAL ANALYSIS

4.2.1. Differential equation

a) Analytical object

As the first premise of nonlinear theoretical analysis method, this study used a steel plate (see Fig. 4.1) bonding only one layer of CFRP sheet under uniaxial tensile loading, to determine the mechanical behavior, the peeling mechanism and the peeling strength of adhesion layer inserted between steel plate and CFRP sheet. In this analytical object, the width of CFRP sheet was taken at the same that of steel plate. In addition, the direction of CFRP sheet bonded was matched with that of the applied force. Further, as a base metal, a normal type of steel was used in this study.

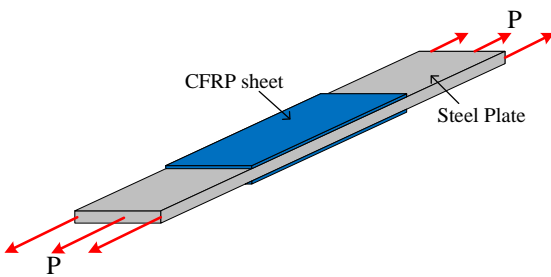


Fig. 4.1 Analytical object

(Steel plate bonding a layer of CFRP).

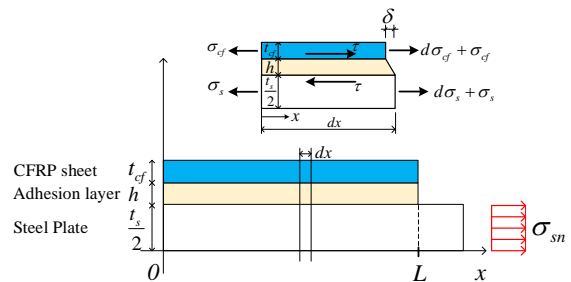
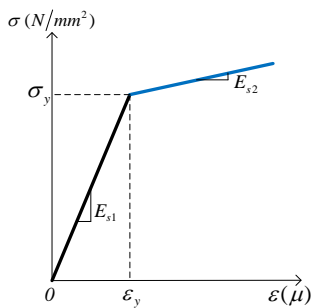
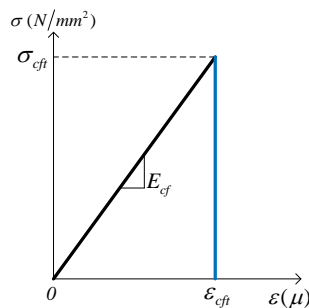


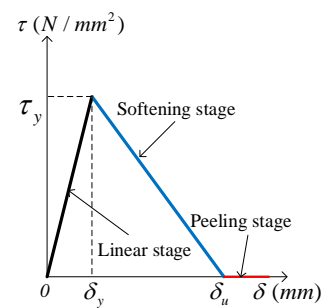
Fig. 4.2 Modeling (1/4 model).



(a) Steel (σ - ϵ)



(b) CFRP sheet (σ - ϵ)



(c) Adhesion layer (τ - δ)

Fig. 4.3 Constitutive models of materials.

b) Modeling

The calculated model is described as a quarter model of the CFRP-sheet-bonded steel plate (see **Fig. 4.2**); and considered the nonlinear material model of steel, CFRP sheet, and adhesion layer as shown in **Fig. 4.3**. Here, as a bonding constitution rule, it is generally assumed that the material model of adhesion layer is considered by the relationship between shear stress and relative displacement, as shown in **Fig. 4.3(c)**. Additionally, the elastic modulus of adhesion layer is smaller by two orders of magnitude than that of steel and CFRP sheet, hence the stress of adhesion layer is assumed only shear stress, and steel plate and CFRP sheet is assumed only tensile stress.

In **Fig. 4.2**; t_s , h , and t_{cf} are the thickness of steel plate, adhesion layer, and CFRP sheet, respectively; L is the length of the original area bonding CFRP sheet; b is the width of steel plate and CFRP sheet; σ_{sn} is the stress at the top location of steel plate, in which CFRP sheet is not bonded; σ_s , τ , and σ_{cf} are the axial stress of steel plate bonding CFRP sheet, the shear stress of adhesion layer, and the axial stress of CFRP sheet, respectively; and δ is the relative displacement between steel plate and CFRP sheet in infinitesimal region dx .

In **Fig. 4.3**; σ_y , ε_y , E_{s1} , and E_{s2} are the yield stress, the yield strain, the primary Young's modulus and the secondary modulus after yield of steel, in that order; σ_{cft} , ε_{cft} , and E_{cf} are the tensile strength, the strain at the tensile strength, the primary Young's modulus of CFRP sheet, respectively; τ_y , δ_y , and δ_u are the shear strength, the relative displacement at the shear strength, the relative displacement at the peeling stage of adhesion layer, respectively.

c) Relationship between stress and strain

When considering a location in the direction along the length of steel plate, with the coordinate being x ; the relationship between stress and strain on steel plate and CFRP sheet, and the relationship between shear stress and relative displacement on adhesion layer are described as the following.

$$\sigma_s = \begin{cases} E_{s1} \frac{du_s}{dx} & (\varepsilon_s \leq \varepsilon_y) \\ (E_{s1} - E_{s2})\varepsilon_y + E_{s2} \frac{du_s}{dx} & (\varepsilon_s > \varepsilon_y) \end{cases} \quad (4.1)$$

$$\sigma_{cf} = \begin{cases} E_{cf} \frac{du_{cf}}{dx} & (\varepsilon_{cf} \leq \varepsilon_{cft}) \\ 0 & (\varepsilon_{cf} > \varepsilon_{cft}) \end{cases} \quad (4.2)$$

$$\tau = \begin{cases} \frac{\tau_y}{\delta_y} \delta & (0 \leq \delta \leq \delta_y) \\ \frac{\tau_y}{\delta_u - \delta_y} (\delta_u - \delta) & (\delta_y < \delta \leq \delta_u) \end{cases} \quad (4.3)$$

where, x is the coordinate in the direction along the length of steel plate; u_s and u_{cf} are the displacement of steel plate, and CFRP sheet, respectively; and δ is the relative displacement between steel plate and CFRP sheet in the infinitesimal region dx .

From **Fig. 4.2**, when considering the balance condition of force in the infinitesimal region dx , the balance equations are obtained as the following.

$$\frac{t_s}{2} \frac{d\sigma_s}{dx} - \tau = 0 \quad (4.4)$$

$$\tau_{cf} \frac{d\sigma_{cf}}{dx} + \tau = 0 \quad (4.5)$$

d) Differential equation

By implementing some basic transformations on Equations (4.4) and (4.5) together with the material properties of Equations (4.1)-(4.3); the differential equations described the mechanical behavior of steel plate, CFRP sheet and adhesion layer were obtained as Equations (4.6) and (4.7). Moreover, as a basic theoretical method, by solving Equations (4.6) and (4.7) under the corresponding boundary conditions; the relative displacement and the shear stress of adhesion layer are able to be found at each loaded step.

In case of $0 \leq \delta \leq \delta_y$:

$$\frac{d^2 \delta(x)}{dx^2} - \left(\frac{2}{E_{s1} t_s} + \frac{1}{E_{cf} t_{cf}} \right) \frac{\tau_y}{\delta_y} \delta(x) = 0 \quad \text{if} \quad (\varepsilon_s \leq \varepsilon_y) \quad (4.6a)$$

$$\frac{d^2 \delta(x)}{dx^2} - \left(\frac{2}{E_{s2} t_s} + \frac{1}{E_{cf} t_{cf}} \right) \frac{\tau_y}{\delta_y} \delta(x) = 0 \quad \text{if} \quad (\varepsilon_s > \varepsilon_y) \quad (4.6b)$$

In case of $\delta_y < \delta \leq \delta_u$:

$$\frac{d^2 \delta(x)}{dx^2} - \left(\frac{2}{E_{s1} t_s} + \frac{1}{E_{cf} t_{cf}} \right) \frac{\tau_y}{\delta_u - \delta_y} (\delta_u - \delta(x)) = 0 \quad \text{if} \quad (\varepsilon_s \leq \varepsilon_y) \quad (4.7a)$$

$$\frac{d^2 \delta(x)}{dx^2} - \left(\frac{2}{E_{s2} t_s} + \frac{1}{E_{cf} t_{cf}} \right) \frac{\tau_y}{\delta_u - \delta_y} (\delta_u - \delta(x)) = 0 \quad \text{if} \quad (\varepsilon_s > \varepsilon_y) \quad (4.7b)$$

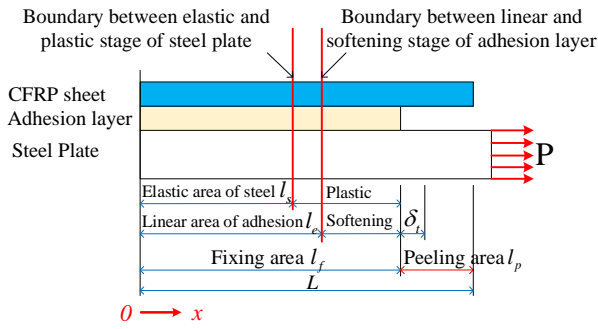


Table 4.1 Cases implemented in calculated program.

Steel / Adhesion	Elastic	Elastic + Plastic	Completely plastic
Linear	Case 1	Case 2	Case 3
Softening	Case 4	Case 5 + Case 6	Case 7

Note:

+ In case 5: $l_e \leq l_s$

+ In case 6: $l_e > l_s$

Fig. 4.4 The peeling mechanism of CFRP sheet.

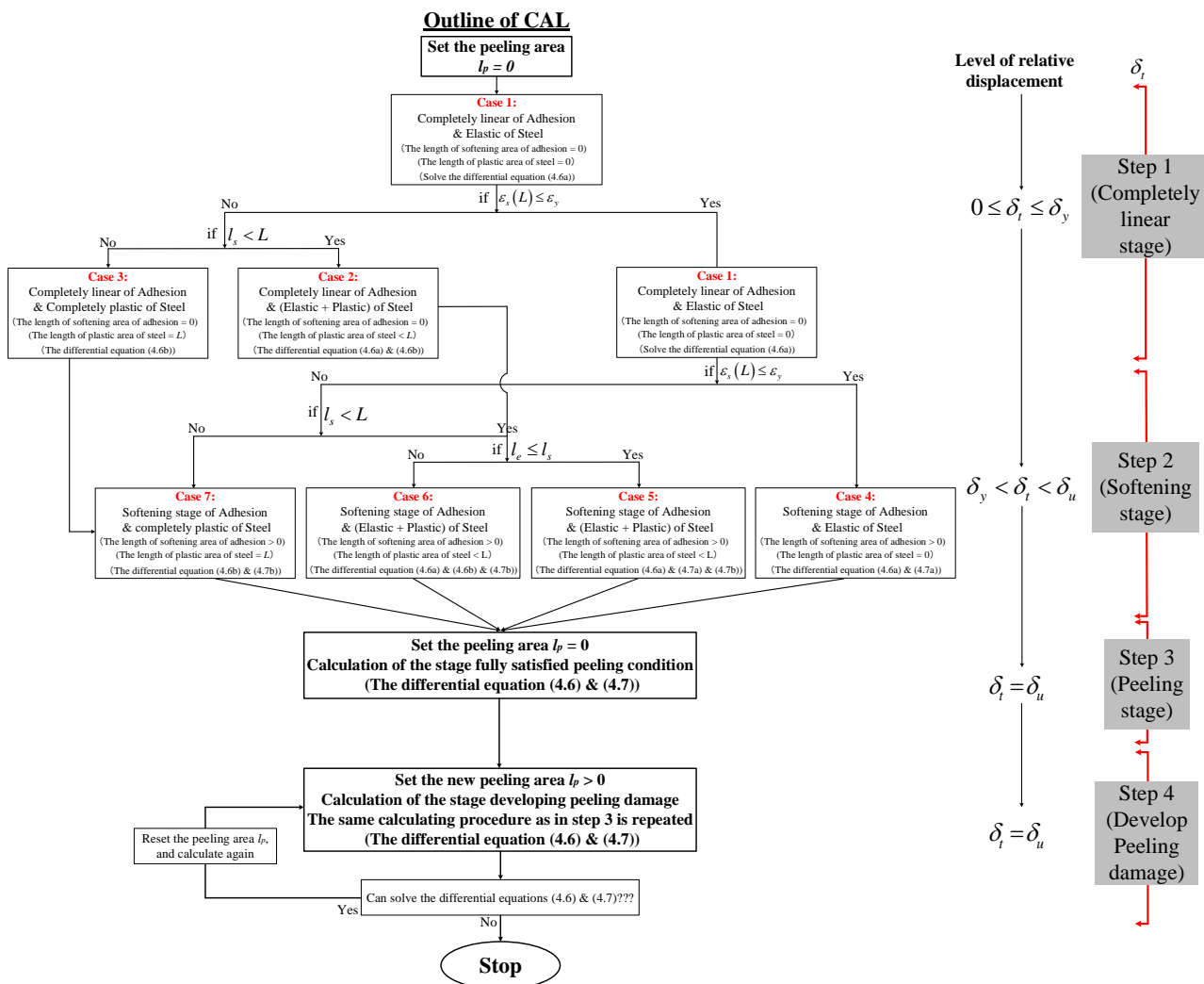


Fig. 4.5 Flowchart of calculation process.

4.2.2. Calculation process

In terms of calculation process, this study has referred to the calculation process of linear analysis of Prof. KAMIHARAKO^{4.1)}. According to the study of Prof. KAMIHARAKO, a theoretical analysis was proposed to simulate bonding and peeling behavior of continuous fiber sheet (CF sheet), with a model of concrete bonding a layer of CF sheet. In Prof. KAMIHARAKO's study, it is assumed that concrete member was the complete rigid body, and CF sheet worked only at the linear phase of material. In addition, the constitutive model of material on adhesion layer was taken as the relationship between shear stress and relative displacement. This study developed the calculation process of Prof. KAMIHARAKO by considering the nonlinear material properties of all members on the analytical object.

The peeling mechanism of CFRP sheet on the analytical object of this study is shown in **Fig. 4.4**. In this analytical object, the peeling damage occurs when the maximum value of the relative displacement on adhesion layer exceeds the value of δ_i of adhesion material. Further, this maximum value is reached at the location of the top of the fixing section of bonded CFRP sheet. Therefore, to simplify the process of calculation, the applied load type is the relative displacement. This means that the calculation process in the proposed theoretical analysis is conducted by gradually increasing the relative displacement of δ_i at the top of the fixing section of CFRP sheet (see **Fig. 4.4**).

In **Fig. 4.4**, L , l_f , and l_p are the length of the original area bonding CFRP sheet, the length of fixing area of CFRP sheet, and the length of peeled area of CFRP sheet, respectively; l_s , and l_e are the length of the elastic area on steel plate, and the length of linear area on adhesion layer, respectively; δ_i is the relative displacement applied to the top of the fixing section of CFRP sheet.

Based on the level of the applied relative displacement and the material model of adhesion layer, the calculation program is classified into the four stages; including the completely linear stage, softening stage, peeling stage, and the developing stage of peeling damage of adhesion layer. Furthermore, **Table 4.1** lists all cases implemented in the calculated program, and **Fig. 4.5** shows the flowchart of this program. The stress and strain values on steel plate, CFRP layer, and adhesion layer were obtained by solving the differential conditions (4.6) and (4.7), along with the corresponding boundary conditions. Additionally, at each step of the applied relative displacement load, the calculation program is stopped if the stress on CFRP layer is greater than the tensile strength of CFRP sheet. Further, the content of each stage in the calculation program is described in the

details as the following.

In step 1 ($0 \leq \delta_t \leq \delta_y$): the mechanical behavior of adhesion layer along the length of CFRP sheet behaves in the completely linear. In this stage, the mechanical behavior on steel plate is classified into three potential cases; including elastic (Case 1), elastic + plastic (Case 2), and completely plastic (Case 3) (see **Table 4.1**).

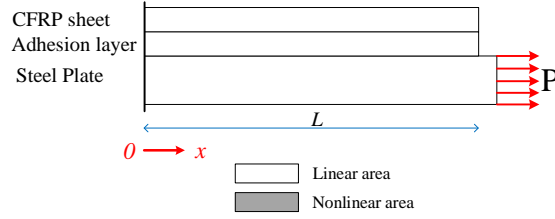
In step 2 ($\delta_y < \delta_t < \delta_u$): there is a part of adhesion layer nearest the top of the fixing location of CFRP sheet which reaches a softening condition. In this stage, the mechanical behavior on steel plate comprises of three potential cases; including elastic (Case 4), elastic + plastic (Case 5 + Case 6), and completely plastic (Case 7) (see **Table 4.1**).

In step 3 ($\delta_t = \delta_u$): the mechanical properties of adhesion layer fully satisfy the peeling condition, and begin to develop the peeling damage at the top of the fixing location of CFRP sheet. In this stage, the mechanical behavior on steel plate is also considered with three potential cases; including elastic (Case 4), elastic + plastic (Case 5 + Case 6), and completely plastic (Case 7) (see **Table 4.1**).

In step 4 ($\delta_t = \delta_u$): in order to express the progress of peeling damage on CFRP sheet, after the peeling condition is fully satisfied in step 3, the length of peeling and fixing areas are newly set, and the same calculating procedure as in step 3 is repeated. Furthermore, the calculation is ended when the length of the set fixing area of CFRP sheet becomes so short, or it is impossible to solve the differential equations (4.6) and (4.7).

In each step of the calculating procedure, the equations used in all of the seven potential cases are summarized as the following.

A) Step 1 ($0 \leq \delta_t \leq \delta_y$)

(a) In case of $\varepsilon_s(L) \leq \varepsilon_y$: **(Case 1)**

Fig. 4.6 Stress constitution in Case 1.

Stress constitution on each member in Case 1 is shown in **Fig. 4.6**.

$$+ \text{ Differential equation (4.6a): } \frac{d^2 \delta(x)}{dx^2} - \left(\frac{2}{E_{s1} t_s} + \frac{1}{E_{cf} t_{cf}} \right) \frac{\tau_y}{\delta_y} \delta(x) = 0$$

$$\text{If } \lambda_1 = \left(\frac{2}{E_{s1} t_s} + \frac{1}{E_{cf} t_{cf}} \right) \frac{\tau_y}{\delta_y}, \text{ then equation (4.6a) is } \frac{d^2 \delta(x)}{dx^2} - \lambda_1 \delta(x) = 0$$

$$+ \text{ Solution of differential equation (4.6a): } \delta(x) = C_1 e^{\sqrt{\lambda_1} x} + C_2 e^{-\sqrt{\lambda_1} x}$$

$$+ \text{ Boundary condition: } x=0 \Rightarrow \delta(0)=0; \quad x=L \Rightarrow \delta(L)=\delta_t \text{ and } \varepsilon_{cf}(L)=0$$

Equation expressed the stress, strain, and relative displacement on steel plate, CFRP sheet, and adhesion layer are shown as the following:

$$\delta(x) = C_{01} \sinh(\sqrt{\lambda_1} x) \quad (4.8a)$$

$$\tau(x) = \frac{\tau_y}{\delta_y} C_{01} \sinh(\sqrt{\lambda_1} x) \quad (4.8b)$$

$$\varepsilon_{cf}(x) = C_{0cf} \left(\cosh(\sqrt{\lambda_1} x) - \cosh(\sqrt{\lambda_1} L) \right) \quad (4.8c)$$

$$\sigma_{cf}(x) = E_{cf} C_{0cf} \left(\cosh(\sqrt{\lambda_1} x) - \cosh(\sqrt{\lambda_1} L) \right) \quad (4.8d)$$

$$\varepsilon_s(x) = C_{0s} \cosh(\sqrt{\lambda_1} x) - C_{0cf} \cosh(\sqrt{\lambda_1} L) \quad (4.8e)$$

$$\sigma_s(x) = E_{s1} C_{0s} \cosh(\sqrt{\lambda_1} x) - E_{s1} C_{0cf} \cosh(\sqrt{\lambda_1} L) \quad (4.8f)$$

$$P = t_s \sigma_s(L) b \quad (4.8g)$$

$$\text{where, } C_{01} = \frac{\delta_t}{\sinh(\sqrt{\lambda_1} L)}, \quad C_{0cf} = \left(-\frac{\tau_y}{\delta_y t_{cf} E_{cf} \sqrt{\lambda_1}} \right) \frac{\delta_t}{\sinh(\sqrt{\lambda_1} L)}, \quad C_{0s} = \left(\sqrt{\lambda_1} - \frac{\tau_y}{\delta_y t_{cf} E_{cf} \sqrt{\lambda_1}} \right) \frac{\delta_t}{\sinh(\sqrt{\lambda_1} L)}.$$

(b) In case of $\varepsilon_s(L) > \varepsilon_y$: (Case 2 + Case 3)

(b.1) Case 2 ($0 < l_s < L$)

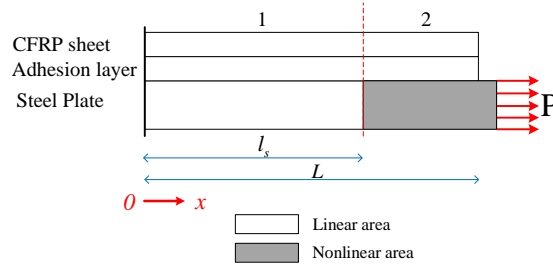


Fig. 4.7 Stress constitution in Case 2.

Stress constitution on each member in Case 2 is shown in Fig. 4.7.

❖ Plastic area of steel plate ($l_s \leq x \leq L$)

$$+ \text{ Differential equation (4.6b): } \frac{d^2 \delta(x)}{dx^2} - \left(\frac{2}{E_{s1} t_s} + \frac{1}{E_{cf} t_{cf}} \right) \frac{\tau_y}{\delta_y} \delta(x) = 0$$

$$\text{If } \lambda_2 = \left(\frac{2}{E_{s2} t_s} + \frac{1}{E_{cf} t_{cf}} \right) \frac{\tau_y}{\delta_y}, \text{ then equation (4.6b) is } \frac{d^2 \delta(x)}{dx^2} - \lambda_2 \delta(x) = 0$$

$$+ \text{ Solution of differential equation (4.6b): } \delta(x) = C_1 e^{\sqrt{\lambda_2} x} + C_2 e^{-\sqrt{\lambda_2} x}$$

$$+ \text{ Boundary condition: } x = L \Rightarrow \delta(L) = \delta_l \text{ and } \varepsilon_{cf}(L) = 0;$$

$$+ \text{ Condition of convergence calculation: } \sigma_s(l_s) = \sigma_y$$

Equations expressed the stress, strain, and relative displacement on steel plate, CFRP sheet, and adhesion layer are shown as the following:

$$\delta(x) = C_1 e^{\sqrt{\lambda_2} x} + C_2 e^{-\sqrt{\lambda_2} x} \quad (4.9a)$$

$$\tau(x) = \frac{\tau_y}{\delta_y} \left(C_1 e^{\sqrt{\lambda_2} x} + C_2 e^{-\sqrt{\lambda_2} x} \right) \quad (4.9b)$$

$$\varepsilon_{cf}(x) = C_{0cf2} \left(C_1 e^{\sqrt{\lambda_2} x} - C_2 e^{-\sqrt{\lambda_2} x} \right) + k_1 \quad (4.9c)$$

$$\sigma_{cf}(x) = E_{cf} C_{0cf2} \left(C_1 e^{\sqrt{\lambda_2} x} - C_2 e^{-\sqrt{\lambda_2} x} \right) + E_{cf} k_1 \quad (4.9d)$$

$$\varepsilon_s(x) = \left(C_{0cf2} + \sqrt{\lambda_2} \right) \left(C_1 e^{\sqrt{\lambda_2} x} - C_2 e^{-\sqrt{\lambda_2} x} \right) + k_1 \quad (4.9e)$$

$$\sigma_s(x) = (E_{s1} - E_{s2}) \varepsilon_y + E_{s2} \left(C_{0cf2} + \sqrt{\lambda_2} \right) \left(C_1 e^{\sqrt{\lambda_2} x} - C_2 e^{-\sqrt{\lambda_2} x} \right) + E_{s2} k_1 \quad (4.9f)$$

$$P = t_s \sigma_s(L)b \quad (4.9g)$$

❖ Elastic area of steel plate ($0 \leq x \leq l_s$)

+ Differential equation (4.6a): $\frac{d^2 \delta(x)}{dx^2} - \lambda_1 \delta(x) = 0$

+ Boundary condition: $x=0 \Rightarrow \delta(0)=0$; $x=l_s \Rightarrow \delta_1(l_s)=\delta_2(l_s)$, $\varepsilon_{cf1}(l_s)=\varepsilon_{cf2}(l_s)$, and $\varepsilon_{s1}(l_s)=\varepsilon_{s2}(l_s)$

Equations expressed the stress, strain, and relative displacement on steel plate, CFRP sheet, and adhesion layer are shown as the following:

$$\delta(x) = C_3 \left(e^{\sqrt{\lambda_1}x} - e^{-\sqrt{\lambda_1}x} \right) \quad (4.10a)$$

$$\tau(x) = \frac{\tau_y}{\delta_y} C_3 \left(e^{\sqrt{\lambda_1}x} - e^{-\sqrt{\lambda_1}x} \right) \quad (4.10b)$$

$$\varepsilon_{cf}(x) = C_{0cf1} C_3 \left(e^{\sqrt{\lambda_1}x} + e^{-\sqrt{\lambda_1}x} \right) + k_2 \quad (4.10c)$$

$$\sigma_{cf}(x) = E_{cf} C_{0cf1} C_3 \left(e^{\sqrt{\lambda_1}x} + e^{-\sqrt{\lambda_1}x} \right) + E_{cf} k_2 \quad (4.10d)$$

$$\varepsilon_s(x) = C_3 \left(C_{0cf1} + \sqrt{\lambda_1} \right) \left(e^{\sqrt{\lambda_1}x} + e^{-\sqrt{\lambda_1}x} \right) + k_2 \quad (4.10e)$$

$$\sigma_s(x) = E_{s1} C_3 \left(C_{0cf1} + \sqrt{\lambda_1} \right) \left(e^{\sqrt{\lambda_1}x} + e^{-\sqrt{\lambda_1}x} \right) + E_{s1} k_2 \quad (4.10f)$$

where, $C_{0cf1} = \left(-\frac{\tau_y}{\delta_y E_{cf} t_{cf} \sqrt{\lambda_1}} \right)$, $C_{0cf2} = \left(-\frac{\tau_y}{\delta_y E_{cf} t_{cf} \sqrt{\lambda_2}} \right)$,

$$D = -2e^{-\sqrt{\lambda_2}(L-l_s)} \left[\sinh(\sqrt{\lambda_1} l_s) - \frac{\sqrt{\lambda_1}}{\sqrt{\lambda_2}} \cosh(\sqrt{\lambda_1} l_s) \right] - 2e^{\sqrt{\lambda_2}(L-l_s)} \left[\sinh(\sqrt{\lambda_1} l_s) + \frac{\sqrt{\lambda_1}}{\sqrt{\lambda_2}} \cosh(\sqrt{\lambda_1} l_s) \right],$$

$$D_1 = -2\delta_t e^{-\sqrt{\lambda_2} l_s} \left[\sinh(\sqrt{\lambda_1} l_s) + \frac{\sqrt{\lambda_1}}{\sqrt{\lambda_2}} \cosh(\sqrt{\lambda_1} l_s) \right],$$

$$D_2 = -2\delta_t e^{\sqrt{\lambda_2} l_s} \left[\sinh(\sqrt{\lambda_1} l_s) - \frac{\sqrt{\lambda_1}}{\sqrt{\lambda_2}} \cosh(\sqrt{\lambda_1} l_s) \right],$$

$$D_3 = -2\delta_t,$$

$$C_1 = \frac{D_1}{D}, \quad C_2 = \frac{D_2}{D}, \quad C_3 = \frac{D_3}{D},$$

$$k_1 = -C_{0cf2} \left[C_1 e^{\sqrt{\lambda_2} L} - C_2 e^{-\sqrt{\lambda_2} L} \right], \quad k_2 = C_{0cf2} \left[C_1 e^{\sqrt{\lambda_2} L_s} - C_2 e^{-\sqrt{\lambda_2} L_s} \right] + k_1 - 2C_3 C_{0cf1} \cosh\left(\sqrt{\lambda_1} l_s\right).$$

(b.2) Case 3 ($l_s = 0$)

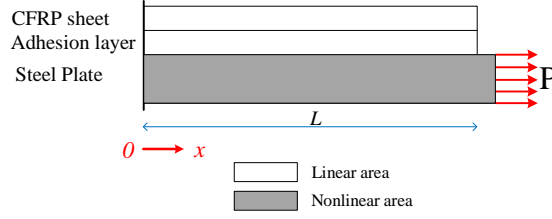


Fig. 4.8 Stress constitution in Case 3.

Stress constitution on each member in Case 3 is shown in **Fig. 4.8**.

+ Differential equation (4.6b): $\frac{d^2 \delta(x)}{dx^2} - \lambda_2 \delta(x) = 0$

+ Boundary condition: $x=0 \Rightarrow \delta(0)=0$; $x=L \Rightarrow \delta(L)=\delta_t$, and $\varepsilon_{cf}(L)=0$

Equations expressed the stress, strain, and relative displacement on steel plate, CFRP sheet, and adhesion layer are shown as the following:

$$\delta(x) = C_{01} \sinh\left(\sqrt{\lambda_2} x\right) \quad (4.11a)$$

$$\tau(x) = \frac{\tau_y}{\delta_y} C_{01} \sinh\left(\sqrt{\lambda_2} x\right) \quad (4.11b)$$

$$\varepsilon_{cf}(x) = C_{0cf1} \left(\cosh\left(\sqrt{\lambda_2} x\right) - \cosh\left(\sqrt{\lambda_2} L\right) \right) \quad (4.11c)$$

$$\sigma_{cf}(x) = E_{cf} C_{0cf1} \left(\cosh\left(\sqrt{\lambda_2} x\right) - \cosh\left(\sqrt{\lambda_2} L\right) \right) \quad (4.11d)$$

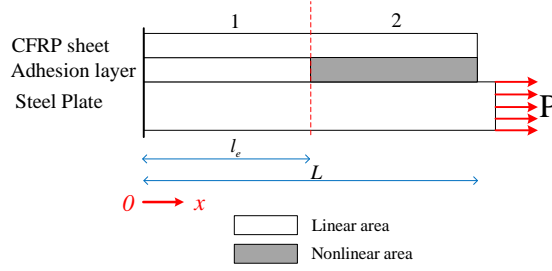
$$\varepsilon_s(x) = C_{0s1} \cosh\left(\sqrt{\lambda_2} x\right) - C_{0cf1} \cosh\left(\sqrt{\lambda_2} L\right) \quad (4.11e)$$

$$\sigma_s(x) = (E_{s1} - E_{s2}) \varepsilon_y + E_{s2} C_{0s1} \cosh\left(\sqrt{\lambda_2} x\right) - E_{s2} C_{0cf1} \cosh\left(\sqrt{\lambda_2} L\right) \quad (4.11f)$$

$$P = t_s \sigma_s(L) b \quad (4.11g)$$

where, $C_{01} = \frac{\delta_t}{\sinh\left(\sqrt{\lambda_2} L\right)}$, $C_{0cf1} = -\frac{\tau_y}{\delta_y t_{cf} E_{cf} \sqrt{\lambda_2}} \frac{\delta_t}{\sinh\left(\sqrt{\lambda_2} L\right)}$, $C_{0s1} = \left(\sqrt{\lambda_2} - \frac{\tau_y}{\delta_y t_{cf} E_{cf} \sqrt{\lambda_2}} \right) \frac{\delta_t}{\sinh\left(\sqrt{\lambda_2} L\right)}$.

B) Step 2 + Step 3 ($\delta_y < \delta_t \leq \delta_u$)

(a) In case of $\varepsilon_s(L) \leq \varepsilon_y$: **(Case 4)**

Fig. 4.9 Stress constitution in Case 4.

Stress constitution on each member in Case 4 is shown in **Fig. 4.9**.

 ❖ Softening area of adhesion layer ($l_e \leq x \leq L$)

$$+ \text{ Differential equation (4.7a): } \frac{d^2 \delta(x)}{dx^2} - \left(\frac{2}{E_{s1} t_s} + \frac{1}{E_{cf} t_{cf}} \right) \frac{\tau_y}{\delta_u - \delta_y} (\delta_u - \delta(x)) = 0$$

$$\text{If } \lambda_1' = \left(\frac{2}{E_{s1} t_s} + \frac{1}{E_{cf} t_{cf}} \right) \frac{\tau_y}{\delta_u - \delta_y}, \text{ then equation (4.7a) is } \frac{d^2 \delta(x)}{dx^2} - \lambda_1' (\delta_u - \delta(x)) = 0$$

$$+ \text{ Solution of differential equation (4.7a): } \delta(x) = \delta_u - \left(C_1 \cos(\sqrt{\lambda_1'} x) + C_2 \sin(\sqrt{\lambda_1'} x) \right)$$

$$+ \text{ Boundary condition: } x = L \Rightarrow \delta(L) = \delta_t, \text{ and } \varepsilon_{cf}(L) = 0; \quad x = l_e \Rightarrow \delta(l_e) = \delta_y$$

Equations expressed the stress, strain, and relative displacement on steel plate, CFRP sheet, and adhesion layer are shown as the following:

$$\delta(x) = \delta_u - \left(C_1 \cos(\sqrt{\lambda_1'} x) + C_2 \sin(\sqrt{\lambda_1'} x) \right) \quad (4.12a)$$

$$\tau(x) = \frac{\tau_y}{\delta_u - \delta_y} \left(C_1 \cos(\sqrt{\lambda_1'} x) + C_2 \sin(\sqrt{\lambda_1'} x) \right) \quad (4.12b)$$

$$\varepsilon_{cf} = C'_{ocf1} \left(C_1 \sin \sqrt{\lambda_1'} x - C_2 \cos \sqrt{\lambda_1'} x \right) + k_1 \quad (4.12c)$$

$$\sigma_{cf} = E_{cf} C'_{ocf1} \left(C_1 \sin \sqrt{\lambda_1'} x - C_2 \cos \sqrt{\lambda_1'} x \right) + E_{cf} k_1 \quad (4.12d)$$

$$\varepsilon_s = \left(C'_{ocf1} + \sqrt{\lambda_1'} \right) \left(C_1 \sin \sqrt{\lambda_1'} x - C_2 \cos \sqrt{\lambda_1'} x \right) + k_1 \quad (4.12e)$$

$$\sigma_s = E_{s1} \left(C'_{ocf1} + \sqrt{\lambda_1'} \right) \left(C_1 \sin \sqrt{\lambda_1'} x - C_2 \cos \sqrt{\lambda_1'} x \right) + E_{s1} k_1 \quad (4.12f)$$

$$P = t_s \sigma_s(L) b \quad (4.12g)$$

❖ Linear area of adhesion layer ($0 \leq x \leq l_e$)

+ Differential equation (4.6a): $\frac{d^2\delta(x)}{dx^2} - \lambda_1\delta(x) = 0$

+ Boundary condition: $x=0 \Rightarrow \delta(0)=0$; $x=l_e \Rightarrow \delta(l_e)=\delta_y$, and $\varepsilon_{s1}(l_e)=\varepsilon_{s2}(l_e)$

+ Condition of convergence calculation: $\varepsilon_{cf1}(l_e)=\varepsilon_{cf2}(l_e)$

Equations expressed the stress, strain, and relative displacement on steel plate, CFRP sheet, and adhesion layer are shown as the following:

$$\delta(x) = C_3 \left(e^{\sqrt{\lambda_1}x} - e^{-\sqrt{\lambda_1}x} \right) \quad (4.13a)$$

$$\tau(x) = \frac{\tau_y}{\delta_y} C_3 \left(e^{\sqrt{\lambda_1}x} - e^{-\sqrt{\lambda_1}x} \right) \quad (4.13b)$$

$$\varepsilon_{cf}(x) = C_3 C_{0cf1} \left(e^{\sqrt{\lambda_1}x} + e^{-\sqrt{\lambda_1}x} \right) + k_2 \quad (4.13c)$$

$$\sigma_{cf}(x) = E_{cf} C_3 C_{0cf1} \left(e^{\sqrt{\lambda_1}x} + e^{-\sqrt{\lambda_1}x} \right) + E_{cf} k_2 \quad (4.13d)$$

$$\varepsilon_s(x) = C_3 \left(C_{0cf1} + \sqrt{\lambda_1} \right) \left(e^{\sqrt{\lambda_1}x} + e^{-\sqrt{\lambda_1}x} \right) + k_2 \quad (4.13e)$$

$$\sigma_s(x) = E_{s1} C_3 \left(C_{0cf1} + \sqrt{\lambda_1} \right) \left(e^{\sqrt{\lambda_1}x} + e^{-\sqrt{\lambda_1}x} \right) + E_{s1} k_2 \quad (4.13f)$$

$$P = t_s \sigma_s(L) b \quad (4.13g)$$

where, $C_{0cf1} = \left(-\frac{\tau_y}{\delta_y E_{cf} t_{cf} \sqrt{\lambda_1}} \right)$, $C'_{0cf1} = \left(-\frac{\tau_y}{(\delta_u - \delta_y) E_{cf} t_{cf} \sqrt{\lambda'_1}} \right)$,

$$D = 2 \sinh(\sqrt{\lambda_1} l_e) \left[\cos(\sqrt{\lambda_1} L) \sin(\sqrt{\lambda_1} l_e) - \cos(\sqrt{\lambda_1} l_e) \sin(\sqrt{\lambda_1} L) \right],$$

$$D_1 = 2 \sinh(\sqrt{\lambda_1} l_e) \left[(\delta_u - \delta_t) \sin(\sqrt{\lambda_1} l_e) - (\delta_u - \delta_y) \sin(\sqrt{\lambda_1} L) \right],$$

$$D_2 = 2 \sinh(\sqrt{\lambda_1} l_e) \left[(\delta_u - \delta_y) \cos(\sqrt{\lambda_1} L) - (\delta_u - \delta_t) \cos(\sqrt{\lambda_1} l_e) \right],$$

$$D_3 = \delta_y \left[\cos(\sqrt{\lambda_1} L) \sin(\sqrt{\lambda_1} l_e) - \cos(\sqrt{\lambda_1} l_e) \sin(\sqrt{\lambda_1} L) \right],$$

$$C_1 = \frac{D_1}{D}, \quad C_2 = \frac{D_2}{D}, \quad C_3 = \frac{D_3}{D}, \quad k_1 = -C'_{0cf1} \left[C_1 \sin(\sqrt{\lambda_1} L) - C_2 \cos(\sqrt{\lambda_1} L) \right],$$

$$k_2 = \left(C'_{0cf1} + \sqrt{\lambda_1} \right) \left[C_1 \sin(\sqrt{\lambda_1} l_e) - C_2 \cos(\sqrt{\lambda_1} l_e) \right] + k_1 - 2C_3 \left(C_{0cf1} + \sqrt{\lambda_1} \right) \cosh(\sqrt{\lambda_1} l_e).$$

(b) In case of $\varepsilon_s(L) > \varepsilon_y$: (Case 5 + Case 6 + Case 7)

(b.1) Case 5 ($l_e \leq l_s < L$)

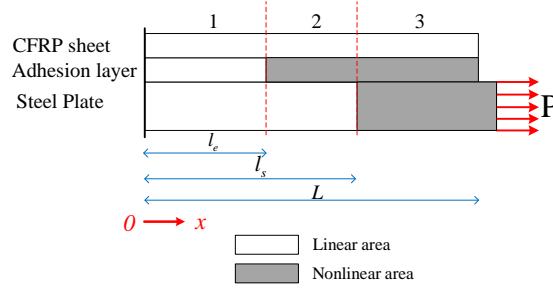


Fig. 4.10 Stress constitution in Case 5.

Stress constitution on each member in Case 5 is shown in Fig. 4.10.

❖ Plastic area of steel plate, and softening area of adhesion layer ($l_s \leq x \leq L$)

+ Differential equation (4.7b):
$$\frac{d^2 \delta(x)}{dx^2} - \left(\frac{2}{E_{s2} t_s} + \frac{1}{E_{cf} t_{cf}} \right) \frac{\tau_y}{\delta_u - \delta_y} (\delta_u - \delta(x)) = 0$$

If $\lambda'_2 = \left(\frac{2}{E_{s2} t_s} + \frac{1}{E_{cf} t_{cf}} \right) \frac{\tau_y}{\delta_u - \delta_y}$, then equation (4.7b) is
$$\frac{d^2 \delta(x)}{dx^2} - \lambda'_2 (\delta_u - \delta(x)) = 0$$

+ Solution of differential equation (4.7b):
$$\delta(x) = \delta_u - (C_1 \cos(\sqrt{\lambda'_2} x) + C_2 \sin(\sqrt{\lambda'_2} x))$$

+ Boundary condition: $x = L \Rightarrow \delta(L) = \delta_l$, and $\varepsilon_{cf}(L) = 0$

Equations expressed the stress, strain, and relative displacement on steel plate, CFRP sheet, and adhesion layer are shown as the following:

$$\delta(x) = \delta_u - (C_1 \cos(\sqrt{\lambda'_2} x) + C_2 \sin(\sqrt{\lambda'_2} x)) \quad (4.14a)$$

$$\tau = \frac{\tau_y}{\delta_u - \delta_y} (C_1 \cos(\sqrt{\lambda'_2} x) + C_2 \sin(\sqrt{\lambda'_2} x)) \quad (4.14b)$$

$$\varepsilon_{cf}(x) = C'_{ocf2} (C_1 \sin(\sqrt{\lambda'_2} x) - C_2 \cos(\sqrt{\lambda'_2} x)) + k_1 \quad (4.14c)$$

$$\sigma_{cf}(x) = E_{cf} C'_{ocf2} (C_1 \sin(\sqrt{\lambda'_2} x) - C_2 \cos(\sqrt{\lambda'_2} x)) + E_{cf} k_1 \quad (4.14d)$$

$$\varepsilon_s(x) = (C'_{ocf2} + \sqrt{\lambda'_2}) (C_1 \sin(\sqrt{\lambda'_2} x) - C_2 \cos(\sqrt{\lambda'_2} x)) + k_1 \quad (4.14e)$$

$$\sigma_s(x) = (E_{s1} - E_{s2}) \varepsilon_y + E_{s2} (C'_{ocf2} + \sqrt{\lambda'_2}) (C_1 \sin(\sqrt{\lambda'_2} x) - C_2 \cos(\sqrt{\lambda'_2} x)) + E_{s2} k_1 \quad (4.14f)$$

$$P = t_s \sigma_s (L) b \quad (4.14g)$$

❖ Elastic area of steel plate, and softening area of adhesion layer ($l_e \leq x \leq l_s$)

+ Differential equation (4.7a): $\frac{d^2 \delta(x)}{dx^2} - \lambda_1' (\delta_u - \delta(x)) = 0$

+ Boundary condition: $x = l_s \Rightarrow \delta_3(l_s) = \delta_2(l_s)$, $\varepsilon_{cf3}(l_s) = \varepsilon_{cf2}(l_s)$, and $\varepsilon_{s3}(l_s) = \varepsilon_{s2}(l_s)$

+ Condition of convergence calculation: $\sigma_s(l_s) = \sigma_y$

Equations expressed the stress, strain, and relative displacement on steel plate, CFRP sheet, and adhesion layer are shown as the following:

$$\delta(x) = \delta_u - \left(C_3 \cos(\sqrt{\lambda_1'} x) + C_4 \sin(\sqrt{\lambda_1'} x) \right) \quad (4.15a)$$

$$\tau = \frac{\tau_y}{\delta_u - \delta_y} \left(C_3 \cos(\sqrt{\lambda_1'} x) + C_4 \sin(\sqrt{\lambda_1'} x) \right) \quad (4.15b)$$

$$\varepsilon_{cf}(x) = C'_{ocf1} \left(C_3 \sin(\sqrt{\lambda_1'} x) - C_4 \cos(\sqrt{\lambda_1'} x) \right) + k_2 \quad (4.15c)$$

$$\sigma_{cf}(x) = E_{cf} C'_{ocf1} \left(C_3 \sin(\sqrt{\lambda_1'} x) - C_4 \cos(\sqrt{\lambda_1'} x) \right) + E_{cf} k_2 \quad (4.15d)$$

$$\varepsilon_s(x) = \left(C'_{ocf1} + \sqrt{\lambda_1'} \right) \left(C_3 \sin(\sqrt{\lambda_1'} x) - C_4 \cos(\sqrt{\lambda_1'} x) \right) + k_2 \quad (4.15e)$$

$$\sigma_s(x) = E_{s1} \left(C'_{ocf1} + \sqrt{\lambda_1'} \right) \left(C_3 \sin(\sqrt{\lambda_1'} x) - C_4 \cos(\sqrt{\lambda_1'} x) \right) + E_{s1} k_2 \quad (4.15f)$$

❖ Elastic area of steel plate, and linear area of adhesion layer ($0 \leq x \leq l_e$)

+ Differential equation (4.6a): $\frac{d^2 \delta(x)}{dx^2} - \lambda_1 \delta(x) = 0$

+ Boundary condition: $x = 0 \Rightarrow \delta(0) = 0$; $x = l_e \Rightarrow \delta_1(l_e) = \delta_y$, $\delta_2(l_e) = \delta_y$, and

$$\varepsilon_{s1}(l_e) = \varepsilon_{s2}(l_e)$$

+ Condition of convergence calculation: $\varepsilon_{cf1}(l_e) = \varepsilon_{cf2}(l_e)$

Equations expressed the stress, strain, and relative displacement on steel plate, CFRP sheet, and adhesion layer are shown as the following:

$$\delta(x) = C_5 \left(e^{\sqrt{\lambda_1} x} - e^{-\sqrt{\lambda_1} x} \right) \quad (4.16a)$$

$$\tau = \frac{\tau_y}{\delta_y} C_5 \left(e^{\sqrt{\lambda_1} x} - e^{-\sqrt{\lambda_1} x} \right) \quad (4.16b)$$

$$\varepsilon_{cf}(x) = C_{ocf1} C_5 \left(e^{\sqrt{\lambda_1} x} + e^{-\sqrt{\lambda_1} x} \right) + k_3 \quad (4.16c)$$

$$\sigma_{cf}(x) = E_{cf} C_{ocf1} C_5 \left(e^{\sqrt{\lambda_1} x} + e^{-\sqrt{\lambda_1} x} \right) + E_{cf} k_3 \quad (4.16d)$$

$$\varepsilon_s(x) = \left(C_{ocf1} + \sqrt{\lambda_1} \right) C_5 \left(e^{\sqrt{\lambda_1} x} + e^{-\sqrt{\lambda_1} x} \right) + k_3 \quad (4.16e)$$

$$\sigma_s(x) = E_{s1} \left(C_{ocf1} + \sqrt{\lambda_1} \right) C_5 \left(e^{\sqrt{\lambda_1} x} + e^{-\sqrt{\lambda_1} x} \right) + E_{s1} k_3 \quad (4.16f)$$

where, $C_{0cf1} = \left(-\frac{\tau_y}{\delta_y E_{cf} t_{cf} \sqrt{\lambda_1}} \right)$, $C'_{0cf1} = \left(-\frac{\tau_y}{(\delta_u - \delta_y) E_{cf} t_{cf} \sqrt{\lambda_1'}} \right)$, $C'_{0cf2} = \left(-\frac{\tau_y}{(\delta_u - \delta_y) E_{cf} t_{cf} \sqrt{\lambda_2'}} \right)$,

$$q_1 = \sin(\sqrt{\lambda_1'} l_s) \cot(\sqrt{\lambda_1'} l_e) - \cos(\sqrt{\lambda_1'} l_s),$$

$$q_2 = \frac{\sin(\sqrt{\lambda_1'} l_s)}{\sin(\sqrt{\lambda_1'} l_e)} (\delta_u - \delta_y),$$

$$q_3 = -\sqrt{\frac{\lambda_1'}{\lambda_2'}} \left[\sin(\sqrt{\lambda_1'} l_s) + \cos(\sqrt{\lambda_1'} l_s) \cot(\sqrt{\lambda_1'} l_e) \right],$$

$$q_4 = -\sqrt{\frac{\lambda_1'}{\lambda_2'}} \frac{\cos(\sqrt{\lambda_1'} l_s)}{\sin(\sqrt{\lambda_1'} l_e)} (\delta_u - \delta_y),$$

$$D = q_1 \cos[\sqrt{\lambda_2'} (L - l_s)] - q_3 \sin[\sqrt{\lambda_2'} (L - l_s)],$$

$$D_1 = (\delta_u - \delta_i) \left[q_1 \cos(\sqrt{\lambda_2'} l_s) + q_3 \sin(\sqrt{\lambda_2'} l_s) \right] - \sin(\sqrt{\lambda_2'} L) (q_2 \cdot q_3 - q_1 \cdot q_4),$$

$$D_2 = \cos(\sqrt{\lambda_2'} L) (q_2 \cdot q_3 - q_1 \cdot q_4) - (\delta_u - \delta_i) \left[q_3 \cos(\sqrt{\lambda_2'} l_s) - q_1 \sin(\sqrt{\lambda_2'} l_s) \right],$$

$$D_3 = -(\delta_u - \delta_i) + q_2 \cos[\sqrt{\lambda_2'} (L - l_s)] - q_4 \sin[\sqrt{\lambda_2'} (L - l_s)],$$

$$C_1 = \frac{D_1}{D}, \quad C_2 = \frac{D_2}{D}, \quad C_3 = \frac{D_3}{D}, \quad C_4 = \frac{1}{\sin(\sqrt{\lambda_1'} l_e)} \left[(\delta_u - \delta_y) - C_3 \cos(\sqrt{\lambda_1'} l_e) \right], \quad C_5 = \frac{\delta_y}{e^{\sqrt{\lambda_1} l_e} - e^{-\sqrt{\lambda_1} l_e}},$$

$$k_1 = -C'_{ocf2} \left[C_1 \sin(\sqrt{\lambda_2'} L) - C_2 \cos(\sqrt{\lambda_2'} L) \right],$$

$$k_2 = C'_{ocf2} \left[C_1 \sin(\sqrt{\lambda_2'} l_s) - C_2 \cos(\sqrt{\lambda_2'} l_s) \right] + k_1 - C'_{ocf1} \left[C_3 \sin(\sqrt{\lambda_1'} l_s) - C_4 \cos(\sqrt{\lambda_1'} l_s) \right],$$

$$k_3 = (C'_{ocf1} + \sqrt{\lambda'_1}) [C_3 \sin(\sqrt{\lambda'_1} l_e) - C_4 \cos(\sqrt{\lambda'_1} l_e)] + k_2 - 2C_5 (C_{ocf1} + \sqrt{\lambda_1}) \cosh \sqrt{\lambda_1} l_e.$$

(b.2) Case 6 ($l_s \leq l_e < L$)

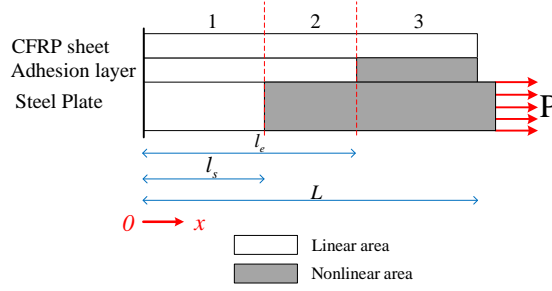


Fig. 4.11 Stress constitution in Case 6.

Stress constitution on each member in Case 6 is shown in **Fig. 4.11**.

❖ Plastic area of steel plate, and softening area of adhesion layer ($l_e \leq x \leq L$)

+ Differential equation (4.7b): $\frac{d^2 \delta(x)}{dx^2} - \lambda'_2 (\delta_u - \delta(x)) = 0$

+ Boundary condition: $x = L \Rightarrow \delta(L) = \delta_t$, and $\varepsilon_{cf}(L) = 0$

Equations expressed the stress, strain, and relative displacement on the steel plate, CFRP sheet, and adhesion layer are shown as the following:

$$\delta(x) = \delta_u - (C_1 \cos(\sqrt{\lambda'_2} x) + C_2 \sin(\sqrt{\lambda'_2} x)) \quad (4.17a)$$

$$\tau = \frac{\tau_y}{\delta_u - \delta_y} (C_1 \cos(\sqrt{\lambda'_2} x) + C_2 \sin(\sqrt{\lambda'_2} x)) \quad (4.17b)$$

$$\varepsilon_{cf}(x) = C'_{ocf2} (C_1 \sin(\sqrt{\lambda'_2} x) - C_2 \cos(\sqrt{\lambda'_2} x)) + k_1 \quad (4.17c)$$

$$\sigma_{cf}(x) = E_{cf} C'_{ocf2} (C_1 \sin(\sqrt{\lambda'_2} x) - C_2 \cos(\sqrt{\lambda'_2} x)) + E_{cf} k_1 \quad (4.17d)$$

$$\varepsilon_s(x) = (C'_{ocf2} + \sqrt{\lambda'_2}) (C_1 \sin(\sqrt{\lambda'_2} x) - C_2 \cos(\sqrt{\lambda'_2} x)) + k_1 \quad (4.17e)$$

$$\sigma_s(x) = (E_{s1} - E_{s2}) \varepsilon_y + E_{s2} (C'_{ocf2} + \sqrt{\lambda'_2}) (C_1 \sin(\sqrt{\lambda'_2} x) - C_2 \cos(\sqrt{\lambda'_2} x)) + E_{s2} k_1 \quad (4.17f)$$

$$P = t_s \sigma_s(L) b \quad (4.17g)$$

❖ Plastic area of steel plate, and linear area of adhesion layer ($l_s \leq x \leq l_e$)

+ Differential equation (4.6b): $\frac{d^2 \delta(x)}{dx^2} - \lambda_2 \delta(x) = 0$

+ Boundary condition: $x = l_e \Rightarrow \delta_2(l_e) = \delta_y$, $\delta_3(l_e) = \delta_y$, and $\varepsilon_{s2}(l_e) = \varepsilon_{s3}(l_e)$

+ Condition of convergence calculation: $\varepsilon_{cf2}(l_e) = \varepsilon_{cf3}(l_e)$

Equations expressed the stress, strain, and relative displacement on steel plate, CFRP sheet, and adhesion layer are shown as the following:

$$\delta(x) = C_3 e^{\sqrt{\lambda_2} x} + C_4 e^{-\sqrt{\lambda_2} x} \quad (4.18a)$$

$$\tau(x) = \frac{\tau_y}{\delta_y} \left(C_3 e^{\sqrt{\lambda_2} x} + C_4 e^{-\sqrt{\lambda_2} x} \right) \quad (4.18b)$$

$$\varepsilon_{cf}(x) = C_{0cf2} \left(C_3 e^{\sqrt{\lambda_2} x} - C_4 e^{-\sqrt{\lambda_2} x} \right) + k_2 \quad (4.18c)$$

$$\sigma_{cf}(x) = E_{cf} C_{0cf2} \left(C_3 e^{\sqrt{\lambda_2} x} - C_4 e^{-\sqrt{\lambda_2} x} \right) + E_{cf} k_2 \quad (4.18d)$$

$$\varepsilon_s(x) = \left(C_{0cf2} + \sqrt{\lambda_2} \right) \left(C_3 e^{\sqrt{\lambda_2} x} - C_4 e^{-\sqrt{\lambda_2} x} \right) + k_2 \quad (4.18e)$$

$$\sigma_s(x) = (E_{s1} - E_{s2}) \varepsilon_y + E_{s2} \left(C_{0cf2} + \sqrt{\lambda_2} \right) \left(C_3 e^{\sqrt{\lambda_2} x} - C_4 e^{-\sqrt{\lambda_2} x} \right) + E_{s2} k_2 \quad (4.18f)$$

❖ Elastic area of steel plate, and linear area of adhesion layer ($0 \leq x \leq l_s$)

+ Differential equation (4.6a): $\frac{d^2 \delta(x)}{dx^2} - \lambda_1 \delta(x) = 0$

+ Boundary condition: $x = 0 \Rightarrow \delta(0) = 0$; $x = l_s \Rightarrow \delta_1(l_s) = \delta_2(l_s)$, $\varepsilon_{cf1}(l_s) = \varepsilon_{cf2}(l_s)$, and

$$\varepsilon_{s1}(l_s) = \varepsilon_{s2}(l_s)$$

+ Condition of convergence calculation: $\sigma_s(l_s) = \sigma_y$

Equations expressed the stress, strain, and relative displacement on steel plate, CFRP sheet, and adhesion layer are shown as the following:

$$\delta(x) = C_5 \left(e^{\sqrt{\lambda_1} x} - e^{-\sqrt{\lambda_1} x} \right) \quad (4.19a)$$

$$\tau = \frac{\tau_y}{\delta_y} C_5 \left(e^{\sqrt{\lambda_1} x} - e^{-\sqrt{\lambda_1} x} \right) \quad (4.19b)$$

$$\varepsilon_{cf}(x) = C_{ocf1} C_5 \left(e^{\sqrt{\lambda_1} x} + e^{-\sqrt{\lambda_1} x} \right) + k_3 \quad (4.19c)$$

$$\sigma_{cf}(x) = E_{cf} C_{ocf1} C_5 \left(e^{\sqrt{\lambda_1} x} + e^{-\sqrt{\lambda_1} x} \right) + E_{cf} k_3 \quad (4.19d)$$

$$\varepsilon_s(x) = \left(C_{ocf1} + \sqrt{\lambda_1} \right) C_5 \left(e^{\sqrt{\lambda_1} x} + e^{-\sqrt{\lambda_1} x} \right) + k_3 \quad (4.19e)$$

$$\sigma_s(x) = E_{s1} \left(C_{ocf1} + \sqrt{\lambda_1} \right) C_5 \left(e^{\sqrt{\lambda_1} x} + e^{-\sqrt{\lambda_1} x} \right) + E_{s1} k_3 \quad (4.19f)$$

where, $C_{ocf1} = \left(-\frac{\tau_y}{\delta_y E_{cf} t_{cf} \sqrt{\lambda_1}} \right)$, $C_{ocf2} = \left(-\frac{\tau_y}{\delta_y E_{cf} t_{cf} \sqrt{\lambda_2}} \right)$, $C'_{ocf2} = \left(-\frac{\tau_y}{(\delta_u - \delta_y) E_{cf} t_{cf} \sqrt{\lambda'_2}} \right)$

$$C_1 = \frac{\frac{\delta_u - \delta_t}{\sin(\sqrt{\lambda'_2} L)} - \frac{\delta_u - \delta_y}{\sin(\sqrt{\lambda'_2} l_e)}}{\cot(\sqrt{\lambda'_2} L) - \cot(\sqrt{\lambda'_2} l_e)}, \quad C_2 = \frac{\frac{\delta_u - \delta_t}{\cos(\sqrt{\lambda'_2} L)} - \frac{\delta_u - \delta_y}{\cos(\sqrt{\lambda'_2} l_e)}}{\tan(\sqrt{\lambda'_2} L) - \tan(\sqrt{\lambda'_2} l_e)},$$

$$D = -2e^{-\sqrt{\lambda_2}(l_e - l_s)} \left[\sinh(\sqrt{\lambda_1} l_s) - \frac{\sqrt{\lambda_1}}{\sqrt{\lambda_2}} \cosh(\sqrt{\lambda_1} l_s) \right] - 2e^{\sqrt{\lambda_2}(l_e - l_s)} \left[\sinh(\sqrt{\lambda_1} l_s) + \frac{\sqrt{\lambda_1}}{\sqrt{\lambda_2}} \cosh(\sqrt{\lambda_1} l_s) \right],$$

$$D_1 = -2\delta_y e^{-\sqrt{\lambda_2} l_s} \left[\sinh(\sqrt{\lambda_1} l_s) + \frac{\sqrt{\lambda_1}}{\sqrt{\lambda_2}} \cosh(\sqrt{\lambda_1} l_s) \right],$$

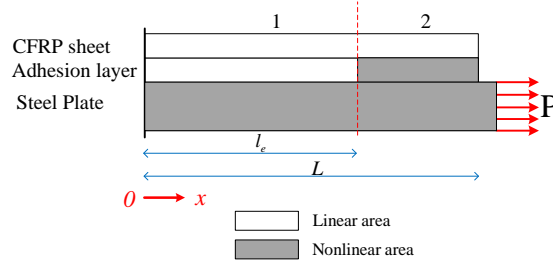
$$D_2 = -2\delta_y e^{\sqrt{\lambda_2} l_s} \left[\sinh(\sqrt{\lambda_1} l_s) - \frac{\sqrt{\lambda_1}}{\sqrt{\lambda_2}} \cosh(\sqrt{\lambda_1} l_s) \right],$$

$$D_3 = -2\delta_y, \quad C_3 = \frac{D_1}{D}, \quad C_4 = \frac{D_2}{D}, \quad C_5 = \frac{D_3}{D},$$

$$k_1 = -C'_{ocf2} \left[C_1 \sin(\sqrt{\lambda'_2} L) - C_2 \cos(\sqrt{\lambda'_2} L) \right],$$

$$k_2 = \left(C'_{ocf2} + \sqrt{\lambda'_2} \right) \left[C_1 \sin(\sqrt{\lambda'_2} l_e) - C_2 \cos(\sqrt{\lambda'_2} l_e) \right] + k_1 - \left(C_{ocf2} + \sqrt{\lambda_2} \right) \left[C_3 e^{\sqrt{\lambda_2} l_e} - C_4 e^{-\sqrt{\lambda_2} l_e} \right],$$

$$k_3 = \left(C_{ocf2} + \sqrt{\lambda_2} \right) \left[C_3 e^{\sqrt{\lambda_2} l_s} - C_4 e^{-\sqrt{\lambda_2} l_s} \right] + k_2 - 2C_5 \left(C_{ocf1} + \sqrt{\lambda_1} \right) \cosh(\sqrt{\lambda_1} l_s).$$

(b.3) Case 7 ($l_s = 0$)

Fig. 4.12 Stress constitution in Case 7.

Stress constitution on each member in Case 7 is shown in **Fig. 4.12**.

❖ Plastic area of steel plate, and softening area of adhesion layer ($l_e \leq x \leq L$)

+ Differential equation (4.7b):
$$\frac{d^2 \delta(x)}{dx^2} - \lambda_2' (\delta_u - \delta(x)) = 0$$

+ Boundary condition: $x = L \Rightarrow \delta(L) = \delta_t$, and $\varepsilon_{cf}(L) = 0$

Equations expressed the stress, strain, and relative displacement on steel plate, CFRP sheet, and adhesion layer are shown as the following:

$$\delta(x) = \delta_u - \left(C_1 \cos(\sqrt{\lambda_2'} x) + C_2 \sin(\sqrt{\lambda_2'} x) \right) \quad (4.20a)$$

$$\tau = \frac{\tau_y}{\delta_u - \delta_y} \left(C_1 \cos(\sqrt{\lambda_2'} x) + C_2 \sin(\sqrt{\lambda_2'} x) \right) \quad (4.20b)$$

$$\varepsilon_{cf}(x) = C'_{ocf2} \left(C_1 \sin(\sqrt{\lambda_2'} x) - C_2 \cos(\sqrt{\lambda_2'} x) \right) + k_1 \quad (4.20c)$$

$$\sigma_{cf}(x) = E_{cf} C'_{ocf2} \left(C_1 \sin(\sqrt{\lambda_2'} x) - C_2 \cos(\sqrt{\lambda_2'} x) \right) + E_{cf} k_1 \quad (4.20d)$$

$$\varepsilon_s(x) = \left(C'_{ocf2} + \sqrt{\lambda_2'} \right) \left(C_1 \sin(\sqrt{\lambda_2'} x) - C_2 \cos(\sqrt{\lambda_2'} x) \right) + k_1 \quad (4.20e)$$

$$\sigma_s(x) = (E_{s1} - E_{s2}) \varepsilon_y + E_{s2} \left(C'_{ocf2} + \sqrt{\lambda_2'} \right) \left(C_1 \sin(\sqrt{\lambda_2'} x) - C_2 \cos(\sqrt{\lambda_2'} x) \right) + E_{s2} k_1 \quad (4.20f)$$

$$P = t_s \sigma_s(L) b \quad (4.20g)$$

❖ Plastic area of steel plate, and linear area of adhesion layer ($0 \leq x \leq l_e$)

+ Differential equation (4.6b):
$$\frac{d^2 \delta(x)}{dx^2} - \lambda_2 \delta(x) = 0$$

+ Boundary condition: $x = l_e \Rightarrow \delta_1(l_e) = \delta_y$, $\delta_2(l_e) = \delta_y$, and $\varepsilon_{s1}(l_e) = \varepsilon_{s2}(l_e)$

+ Condition of convergence calculation: $\varepsilon_{cf1}(l_e) = \varepsilon_{cf2}(l_e)$

Equations expressed the stress, strain, and relative displacement on the steel plate, CFRP sheet, and adhesion layer are shown as the following:

$$\delta(x) = C_3 e^{\sqrt{\lambda_2} x} + C_4 e^{-\sqrt{\lambda_2} x} \quad (4.21a)$$

$$\tau(x) = \frac{\tau_y}{\delta_y} \left(C_3 e^{\sqrt{\lambda_2} x} + C_4 e^{-\sqrt{\lambda_2} x} \right) \quad (4.21b)$$

$$\varepsilon_{cf}(x) = C_{0cf2} \left(C_3 e^{\sqrt{\lambda_2} x} - C_4 e^{-\sqrt{\lambda_2} x} \right) + k_2 \quad (4.21c)$$

$$\sigma_{cf}(x) = E_{cf} C_{0cf2} \left(C_3 e^{\sqrt{\lambda_2} x} - C_4 e^{-\sqrt{\lambda_2} x} \right) + E_{cf} k_2 \quad (4.21d)$$

$$\varepsilon_s(x) = \left(C_{0cf2} + \sqrt{\lambda_2} \right) \left(C_3 e^{\sqrt{\lambda_2} x} - C_4 e^{-\sqrt{\lambda_2} x} \right) + k_2 \quad (4.21e)$$

$$\sigma_s(x) = (E_{s1} - E_{s2}) \varepsilon_y + E_{s2} \left(C_{0cf2} + \sqrt{\lambda_2} \right) \left(C_3 e^{\sqrt{\lambda_2} x} - C_4 e^{-\sqrt{\lambda_2} x} \right) + E_{s2} k_2 \quad (4.21f)$$

where, $C_{0cf2} = \left(-\frac{\tau_y}{\delta_y E_{cf} t_{cf} \sqrt{\lambda_2}} \right)$, $C'_{0cf2} = \left(-\frac{\tau_y}{(\delta_u - \delta_y) E_{cf} t_{cf} \sqrt{\lambda'_2}} \right)$,

$$C_1 = \frac{\frac{\delta_u - \delta_t}{\sin(\sqrt{\lambda'_2} L)} - \frac{\delta_u - \delta_y}{\sin(\sqrt{\lambda'_2} l_e)}}{\cot(\sqrt{\lambda'_2} L) - \cot(\sqrt{\lambda'_2} l_e)}, \quad C_2 = \frac{\frac{\delta_u - \delta_t}{\cos(\sqrt{\lambda'_2} L)} - \frac{\delta_u - \delta_y}{\cos(\sqrt{\lambda'_2} l_e)}}{\tan(\sqrt{\lambda'_2} L) - \tan(\sqrt{\lambda'_2} l_e)},$$

$$C_3 = \frac{\delta_y}{e^{\sqrt{\lambda_2} l_e} - e^{-\sqrt{\lambda_2} l_e}}, \quad k_1 = -C'_{0cf2} \left[C_1 \sin(\sqrt{\lambda'_2} L) - C_2 \cos(\sqrt{\lambda'_2} L) \right],$$

$$k_2 = \left(C'_{0cf2} + \sqrt{\lambda'_2} \right) \left[C_1 \sin(\sqrt{\lambda'_2} l_e) - C_2 \cos(\sqrt{\lambda'_2} l_e) \right] + k_1 - 2C_3 \left(C_{0cf2} + \sqrt{\lambda_2} \right) \cosh(\sqrt{\lambda_2} l_e).$$

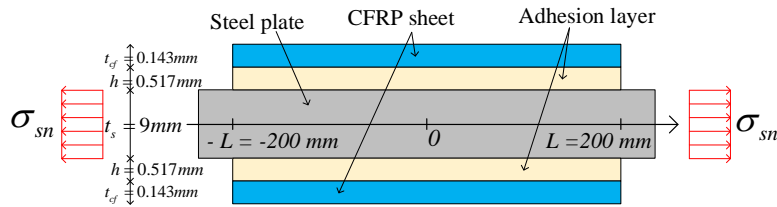


Fig. 4.13 Calculated model of example.

Table 4.2 Material properties of steel, CFRP sheet, and adhesive layer.

Steel (SS400)	Elastic modulus	E_{s1}	(MPa)	2×10^5
	Secondary modulus after yield	$E_{s2} = E_{s1}/100$	(MPa)	2×10^3
	Yield stress	σ_y	(MPa)	317
	Thickness	t_s	(mm)	9
	Width	b	(mm)	60
	Poisson's ratio	ν		0.3
CFRP sheet	Elastic modulus	E_{cf}	(MPa)	6.4×10^5
	Tensile strength	σ_{cft}	(MPa)	2430
	Thickness	t_{cf}	(mm)	0.143
	Anchoring length	L	(mm)	200
	Width	b	(mm)	60
	Poisson's ratio	ν		0.49
Adhesion layer	Thickness	h	(mm)	0.517
	Width	b	(mm)	60
	Shear strength	τ_y	(MPa)	4.3
	Relative displacement at shear strength	δ_y	(mm)	0.15
	Relative displacement at peeling stage	δ_u	(mm)	0.34

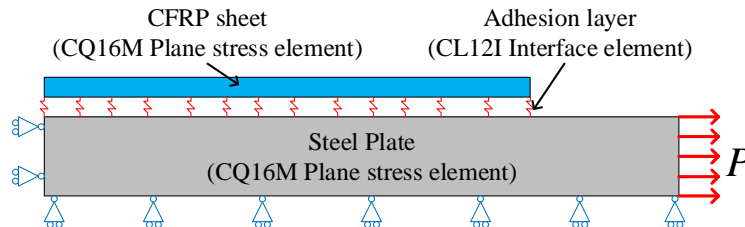


Fig. 4.14 Finite element analysis model of steel plate bonding a CFRP sheet.

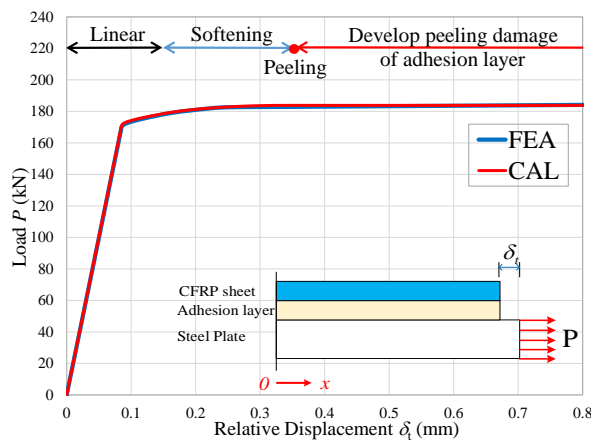
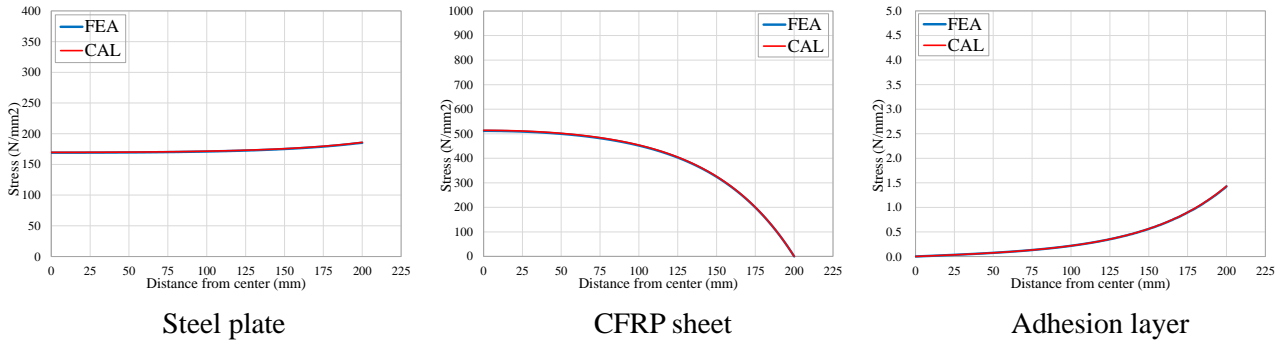
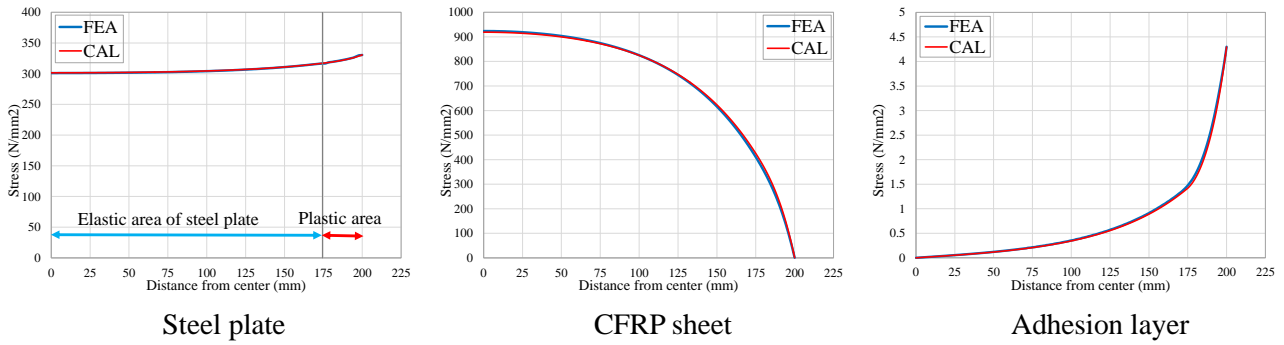


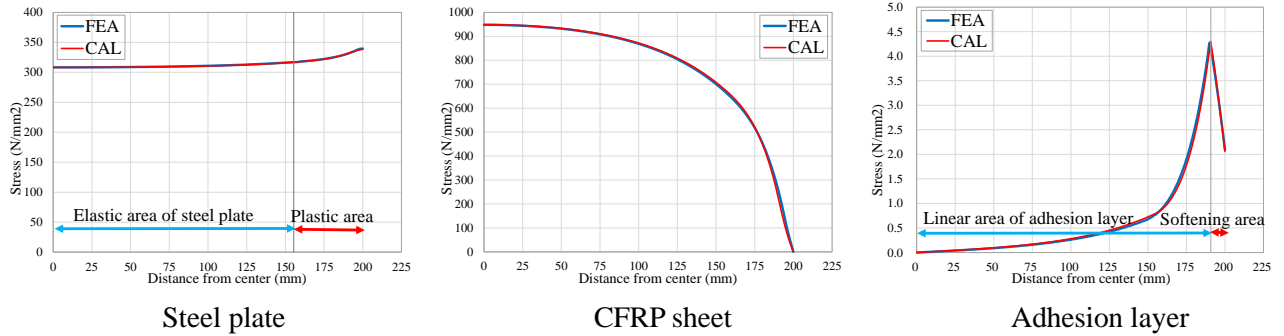
Fig. 4.15 Load – relative displacement relationship.



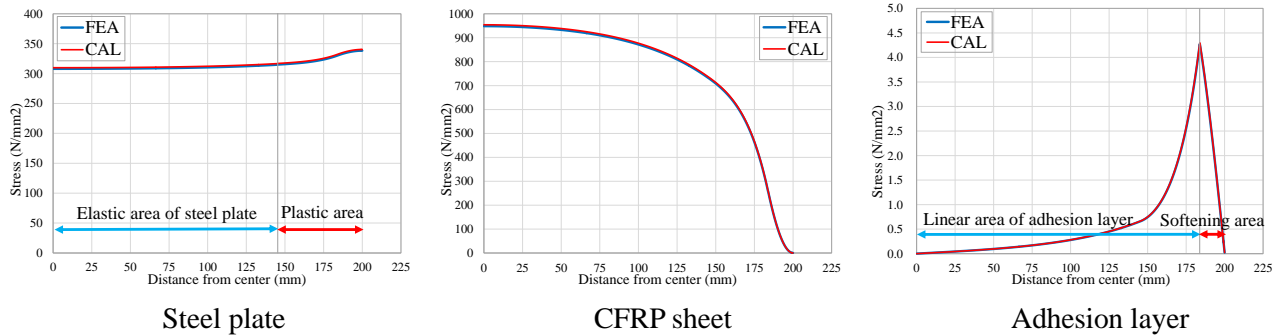
(a) At the load of 100 kN
(behaving the linear stage for all of members)



(b) At the load of 178.6 kN
(behaving elastic + plastic stage for steel plate, and linear stage for adhesion layer)



(c) At the load of 182.9 kN
(behaving elastic + plastic stage for steel plate, and linear + Softening stage for adhesion layer)



(d) At the load of 183.825 kN
(behaving elastic + plastic stage for steel plate, and fully satisfied peeling condition on adhesion layer)

Fig. 4.16 Comparison of stress distribution between FEA and CAL.

4.2.3. Example and discussion

a) Calculated model

In the example, the calculated model and the mechanical properties of all of members are shown in **Fig. 4.13** and **Table 4.2**, respectively. The length and thickness of steel plate were 400 mm and 9 mm, respectively; and 400 mm and 0.143 mm, respectively, regarding CFRP sheet. In this calculated model, the width of CFRP sheet was taken at the same that of steel plate with 60 mm. CFRP sheet was bonded to steel plate by using an adhesion layer with the thickness of 0.517 mm. Moreover, SS400 steel was used as a base metal. The stress-strain curve relationship of the SS400 steel used in this calculated model was bilinear, in which the primary Young's modulus was $E_{s1} = 2 \times 10^5$ MPa, and secondary modulus after yield was $E_{s2} = E_{s1}/100 = 2000$ MPa. The Poisson ratio was 0.3, the yield stress was 317 MPa. The employed FTS-C8-30 CFRP, in sheet form, is lightweight (2.1 g/cm³), has a large tensile strength (2430 MPa), and is durable in harsh environments. In particular, the FTS-C8-30 CFRP sheet has an elastic modulus that is 3.2 times higher than that of the steel with the elastic modulus of 6.4×10^5 MPa. Turning to the adhesion layer, its shear strength τ_y , relative displacement δ_y at shear strength, and relative displacement δ_u at peeling stage were 4.3 MP, 0.15 mm, and 0.34 mm, respectively. By using the proposed method of the nonlinear theoretical analysis; the stress, strain of steel plate, CFRP sheet and adhesion layer on the model of example were obtained.

b) Finite element analysis

In order to confirm the accuracy of the proposed nonlinear theoretical method, a two-dimensional geometric nonlinear FEM analysis was implemented with a quarter model of the steel plate bonding a CFRP layer, using a distribution load as shown in **Fig. 4.14**. Steel plate and CFRP sheet were constructed of plane stress element (the eight-node CQ16M in DIANA analysis software). Moreover, adhesion layer was simulated by using the interface element (CL12I element in DIANA analysis software). The boundary conditions are considered on two symmetrical sides, with a fixed perpendicular direction, and free in the other direction, as shown in **Fig. 4.14**. The resolution of the finite element mesh was 2 mm for the direction along the length of model. Further, division of the thickness of steel plate and CFRP sheet was taken as 10 divisions. As the default, the division of the interface element, which simulated adhesion layer was 1 division. All of mechanical properties applied to the FEM model were taken as values listed in **Table 4.2**. In addition, the material model of adhesion layer in the normal direction was considered to be completely hard. The Von Mises yield condition

was applied to simulate the steel material, and geometric nonlinearity was considered.

c) Calculated results of proposed method

The relationship between load and relative displacement at the top of the fixing location of CFRP sheet is shown in **Fig. 4.14**, to provide a comparison between the FEM analytical and proposed theoretical analytical results. From the proposed theoretical analysis, it is clear that the load-relative displacement curve begins to change at a load of 171 kN (initial plastic load) because the stress on a part of steel plate reached to plastic condition. Meanwhile at this load level, CFRP sheet and adhesion layer still work at the linear stage. This trend is consistent with the behavior obtained in the FEM analysis. Furthermore, the FEM analytical and theoretical analytical initial stiffness of steel plate bonding CFRP sheet is in complete agreement. After overcoming the initial plastic load, the load-relative displacement curve is gradually bent until appearing the peeling damage at the top of the fixing location of CFRP sheet, under a load of 183.825 kN. Moreover, load value of steel plate bonding CFRP is almost no change after occurring peeling damage on CFRP sheet. All of the trend described above are exactly the same as those obtained in the FEM analysis.

Figure 4.16 described the stress distribution of steel plate, CFRP sheet, and adhesion layer; which obtained in the proposed theoretical analysis and FEM analysis; at the load of 100 kN, 178.6 kN, 182.9 kN and 183.825 kN. From **Fig. 4.16**, the stress of CFRP sheet is so small compared to its tensile strength during the loading process. Further, the comparison of the CAL and FEA results shown in **Fig. 4.16** indicates consistent agreement between both results. Under the load value of 100 kN, the mechanical behavior on all of members of the calculated model is linear stage (see **Fig. 4.16(a)**). At the load of 178.6 kN, a part of steel plate on the calculated model reached to plastic condition, while the stress of adhesion layer is still smaller than its shear strength (see **Fig. 4.16(b)**). At the load of 182.9 kN, the plastic area on steel plate is extended, and a part of adhesion layer reached to softening condition (see **Fig. 4.16(c)**). Then, when the applied relative displacement value continues to increase to the value of $\delta_t = 0.34$ mm, the peeling damage of CFRP sheet begin to appear at the load of 183.825 kN. This also means that the peeling strength of CFRP sheet is determined when the shear stress of adhesion layer at the top of the fixing location of CFRP sheet reaches to the value of zero (see **Fig. 4.16(d)**). In this example, the peeling load of the calculated model is 183.825 kN.

As a result, the mechanical behavior of steel plate, CFRP sheet, and adhesion layer could be evaluated accurately by using the proposed theoretical analysis. Additionally, the peeling strength of the calculated model

in the proposed method is determined when the shear stress of adhesion layer at the fixing location of CFRP sheet reaches to the value of zero.

In short, in Section 4.2, for the steel member bonding a layer of CFRP sheet in uniaxial-tensile-stress condition; it was possible to accurately evaluate the peeling strength and the mechanical behavior of steel plate, CFRP sheet, and adhesion layer, by developing the nonlinear theoretical analysis. In future, it will be necessary to develop the nonlinear analysis method for the steel plate with multilayered CFRP sheet under uniaxial loading and bending. Moreover, in order to reproduce the peeling failure of CFRP sheets under the environment of FEM analysis, the use of the interface element is strongly preferred to simulate adhesion layer, in which the peeling failure occurred.

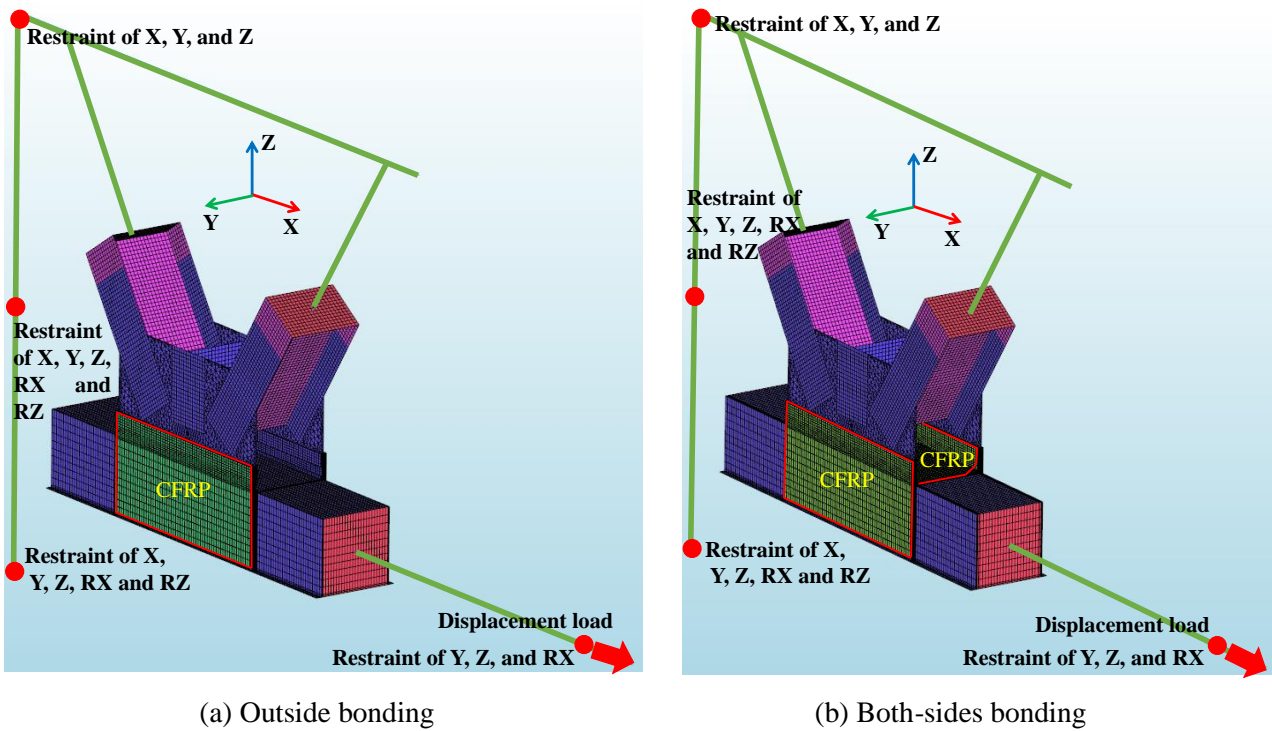


Fig. 4.17 Finite element analysis model of corroded gusset plate connection bonding CFRP sheets.

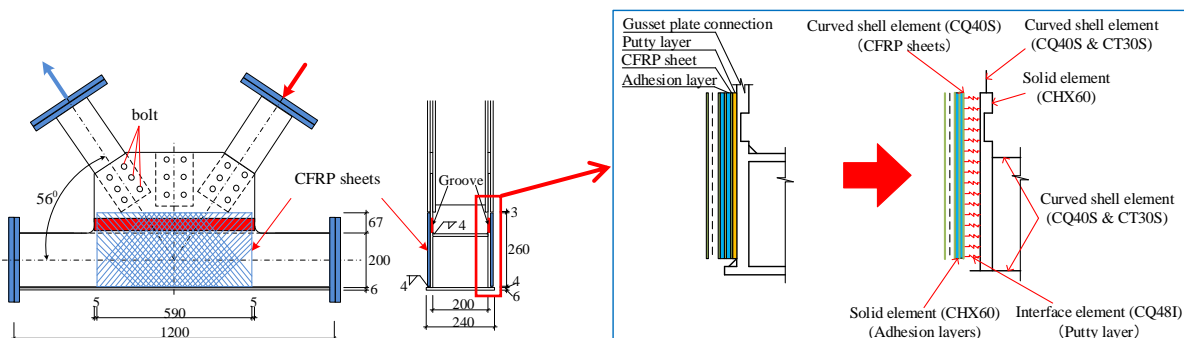


Fig. 4.18 Element types used for simulation.

Table 4.3 Element types and material types used for simulation.

Member	Element type	Material
Gusset plate	Curved shell element (CQ40S & CT30S)	Multilinear (Steel)
Diagonal member		
Lower chord member		
Groove section	Solid element (CHX60)	
Connecting plates	Curved shell element (CQ40S)	Elastic (Steel)
Adhesion layer	Solid element (CHX60)	Elastic
CFRP sheets	Curved shell element (CQ40S & CT30S)	Orthotropic
Putty layer	Interface element (CQ48I)	Nonlinear (Stress-relative displacement)
Groove section putty	Solid element (CHX60)	Elastic
Members of loading frame	3D-beam element (L13BE)	Elastic

Table 4.4 Material properties of steel, and adhesion layer for simulation.

	Steel (SS400)	Adhesion (Resin)	Groove section putty
Young's modulus (MPa)	2×10^5	2533	4021
Poisson's ratio	0.3	0.38	0.38
Yield stress (MPa)	317	–	–
Tensile strength (MPa)	436	–	–
Second-order modulus (MPa)	2000	–	–

Table 4.5 Material properties (orthotropic) of CFRP sheet for simulation.

CFRP sheet (FTS-C8-30)	
Young's modulus x-direction (MPa)	640000
Young's modulus y-direction (MPa)	2412.5
Young's modulus z-direction (MPa)	2412.5
Poisson's ratio xy	0.3
Poisson's ratio yz	0.3
Poisson's ratio zx	0.3
Shear modulus xy (MPa)	927.9
Shear modulus yz (MPa)	927.9
Shear modulus zx (MPa)	866.9

where, x is the main working direction of CFRP sheet.

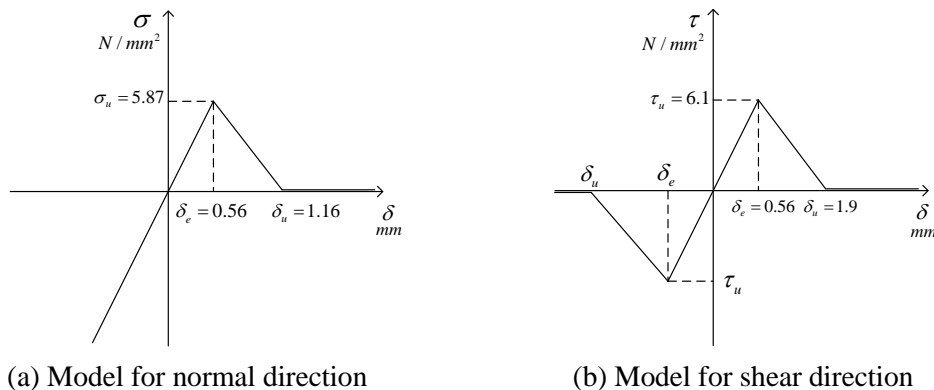


Fig. 4.19 Constitutive model of material for interface element (Polyurea putty layer).

4.3. FINITE ELEMENT ANALYSIS

After grasping the peeling mechanism of CFRP sheets from the proposed nonlinear theoretical analysis, finite element analyses were implemented on the repaired gusset plate connection to reproduce the experimental results obtained in Chapter 3.

4.3.1. Analysis model

A three-dimensional geometric nonlinear analysis was conducted to simulate the corroded gusset plate connection bonding CFRP sheets, using a displacement load as shown in **Fig. 4.17**. All of the element types used for simulation of the gusset plate connection with are shown and listed in **Fig. 4.18** and **Table 4.3**. In which, the gusset plate, diagonal member, lower chord member, and connecting plates were constructed of curved shell elements (the eight-node CQ40S and six-node CT30S). The Groove section itself was modeled by using the solid brick element (the twenty-node CHX60). Further, the sections connecting this solid element to the shell element were considered to be in the central plane of the cross-section of the gusset plate. The dimensions of the members of the loading link frame were designed such that they would operate within their elastic phase during the loading test process. Therefore, the members of loading frame were simulated using the three-dimensional beam element (the two-node L13BE). As the result obtained in the loading tests conducted in Chapter 3, it is confirmed that peeling failure of the gusset plate connection bonding CFRP sheets occurred only on the polyurea putty layer, which was inserted between the steel members and the first layer of CFRP sheets. Hence, this polyurea putty layer, in which peeling damage appeared, was simulated by using the interface element (CQ48I element). Further, adhesion layers, which was used to bond CFRP sheets together, were constructed of the solid brick element (the twenty-node CHX60). In addition, CFRP sheets were modeled using curved shell elements (the eight-node CQ40S and six-node CT30S). Moreover, to enable easier simulation of the connecting sections between the gusset plate and the diagonal members, these connections were modeled as being monolithic. This means that the high-tension bolts were not modeled in the FEM analysis, and the gusset plate and flange of the diagonal member was the same plane.

The resolution of the finite element mesh in all of the models was 1 mm for the Groove section and 5 mm in other members. The division of the thickness of steel plate and adhesion layers was taken as 10 divisions. As the default, the division of the interface element (CQ48I element), which simulated polyurea putty layer was 1 division. Therefore, the total number of nodes and elements was approximately 498547 and 208888,

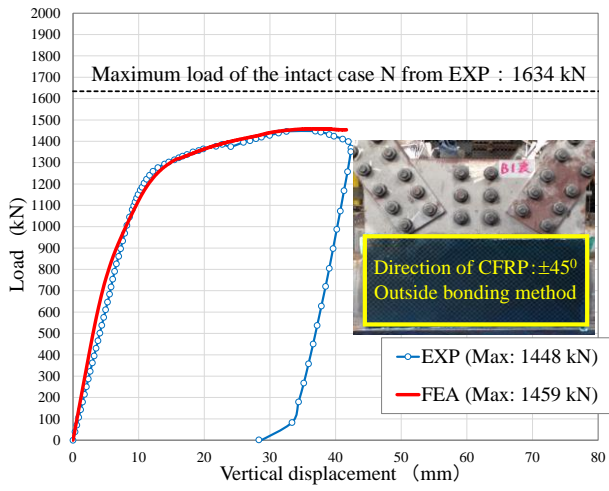
respectively, in cases with outside bonding, and 502906 and 209508, respectively, in cases with both-sides bonding.

4.3.2. Material

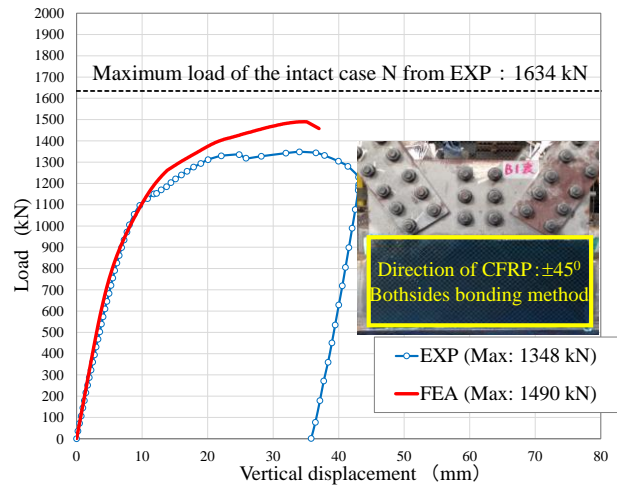
The mechanical properties of steel, adhesion layer, and CFRP sheets used in the simulation are listed in **Table 4.4** and **Table 4.5**. The stress-strain curve relationship of the SS400 steel used in this analysis was bilinear, in which the primary Young's modulus was 200 GPa, and the secondary modulus after yield was $E/100 = 2$ GPa. The Poisson ratio was 0.3, the yield stress and tensile strength were 317 MPa and 436 MPa, respectively, as declared on the mill sheet certificate. In addition, the yield stress and tensile strength of the SS400 steel were also reconfirmed through the tensile experiment in the laboratory. The Von Mises yield condition was applied to simulate the steel material, and geometric nonlinearity was considered. In this analysis, all members of the gusset plate connection were simulated as a multilinear material, and the loading members and connecting plates were considered to be elastic materials.

Adhesion layers and the epoxy-type putty, which filled the cross-sectional loss part of the Groove, were considered elastic materials with the material information shown in **Table 4.4**. This is because, during the process of the loading tests, there was no damage to these locations. The employed FTS-C8-30 CFRP, in sheet form, is lightweight (2.1 g/cm^3), and has a large tensile strength (2430 MPa). Among all of the simulated models of the gusset plate connections bonding CFRP sheets, CFRP sheets were considered as an orthotropic material, with a primary elastic modulus of 640 GPa, and the other modulus of 2412.5 MPa. All of the material information related to CFRP sheets is listed in **Table 4.5**.

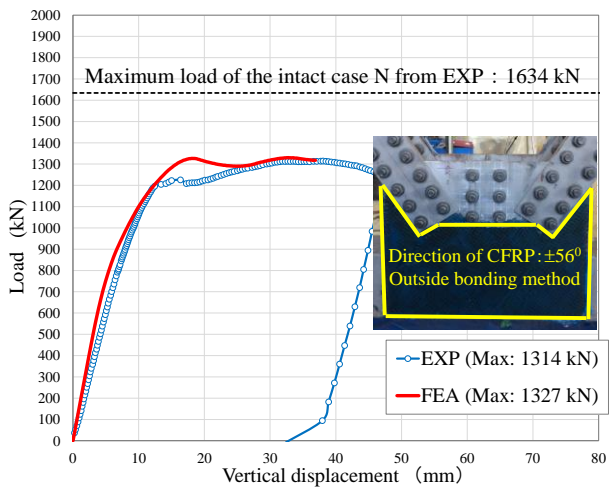
On the other hand, in order to reproduce the peeling failure between the gusset plate and CFRP sheets at the polyurea putty layer, this putty layer was modeled using the interface element of CQ48I in the analysis models. Further, as basic material properties of the interface element of CQ48I, its material model was considered by the relationship between stress and relative displacement in the two directions: including normal direction and shear direction. Moreover, by conducting the material tests of the polyurea putty in the laboratory, its material models for normal direction and shear direction are shown in **Fig. 4.19**.



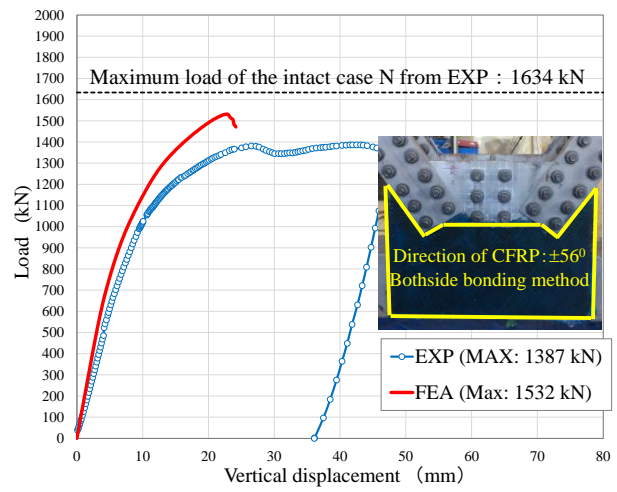
(a) Case of S1_45



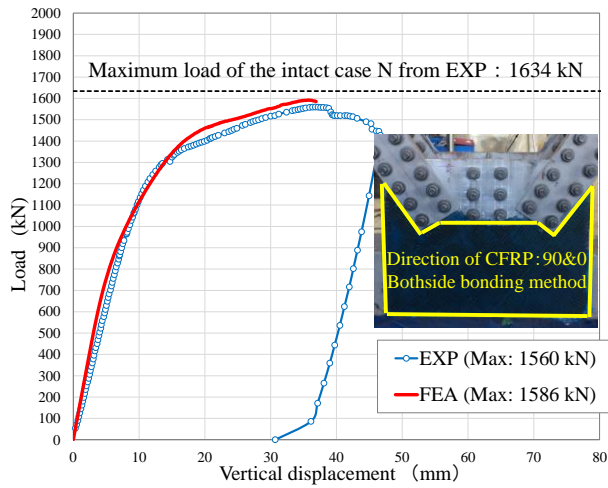
(b) Case of S2_45



(c) Case of S1_56

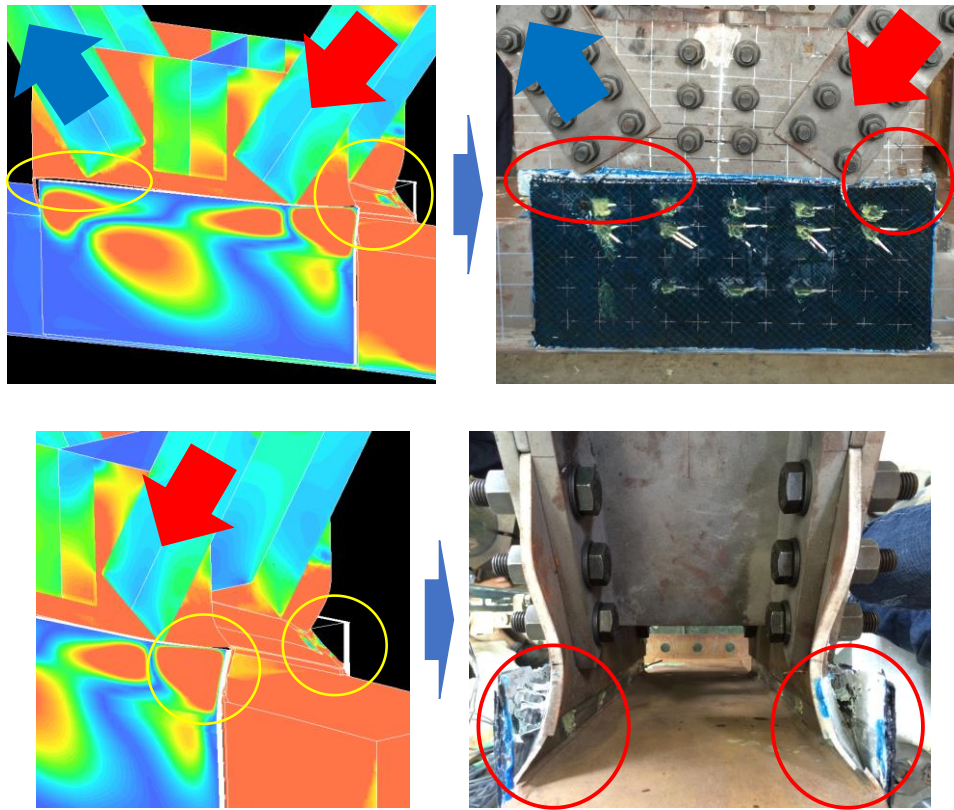


(d) Case of S2_56

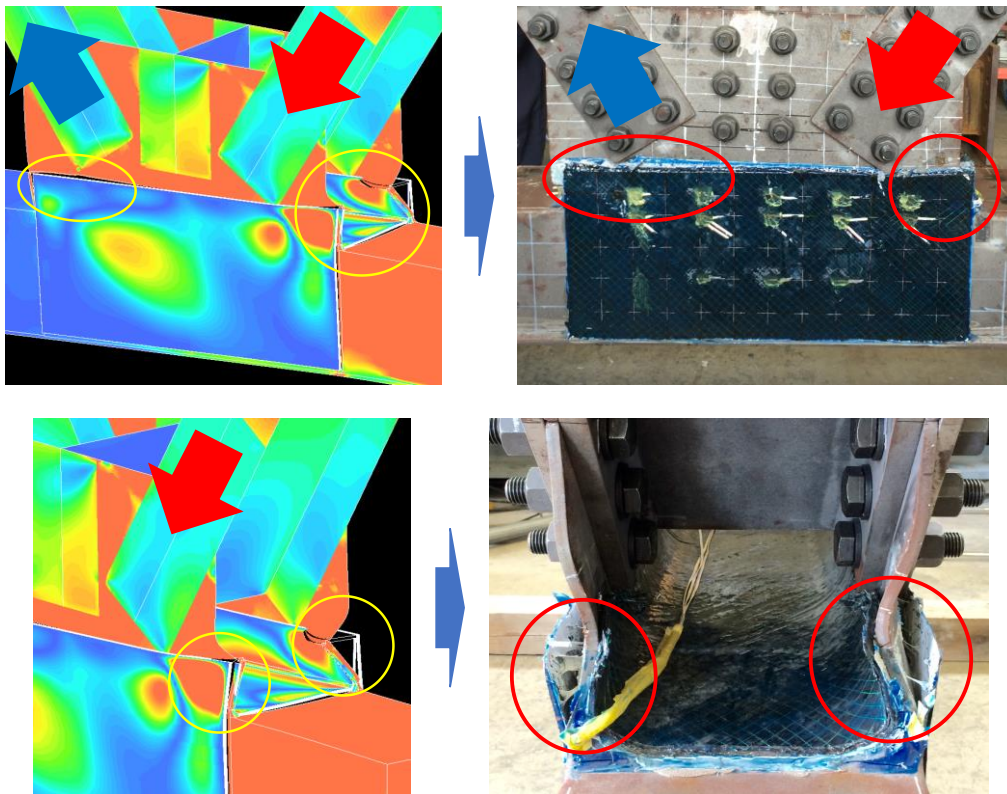


(e) Case of S2_90

Fig. 4.20 Load-Vertical displacement relationship.

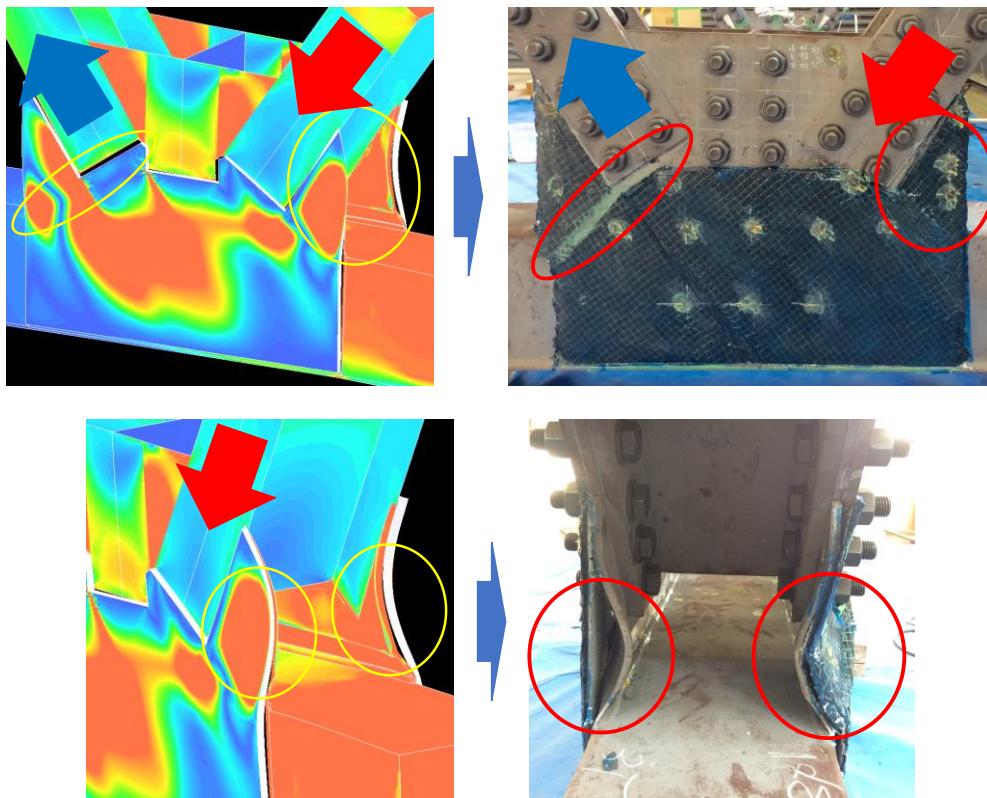


(a) Case of S1_45

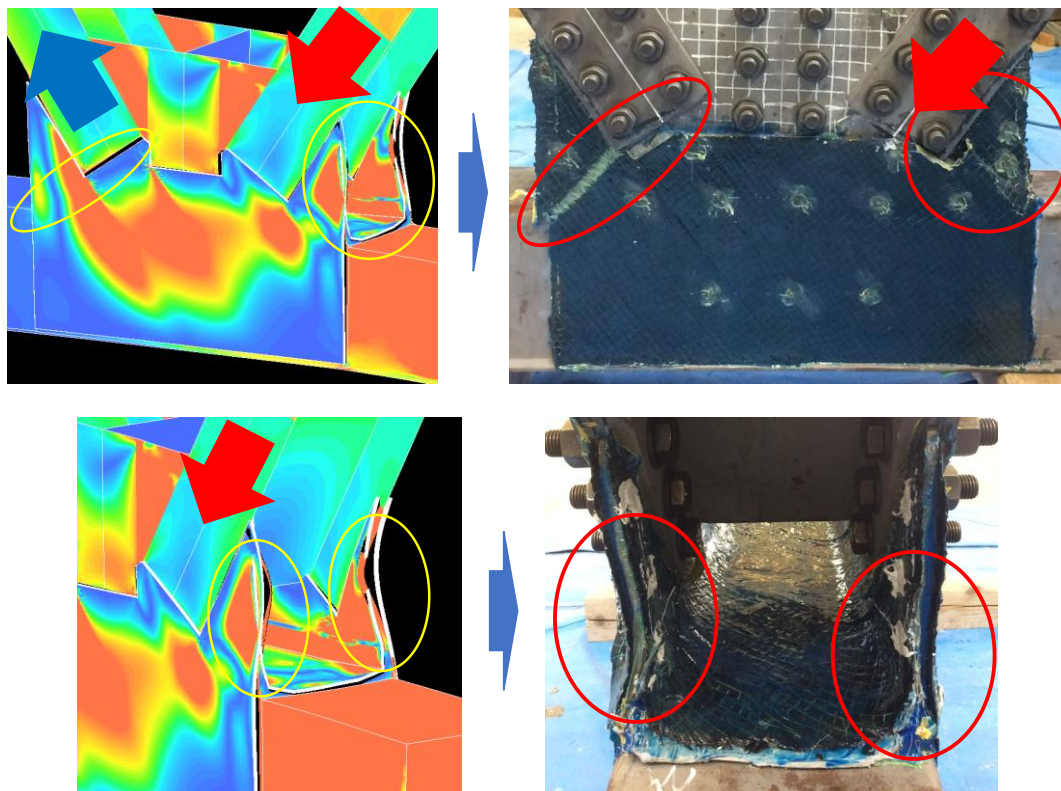


(b) Case of S2_45

Fig. 4.21 Analytical contours of out-of-plane deformation and physical deformation of the corroded gusset plate connection bonding CFRP sheets.

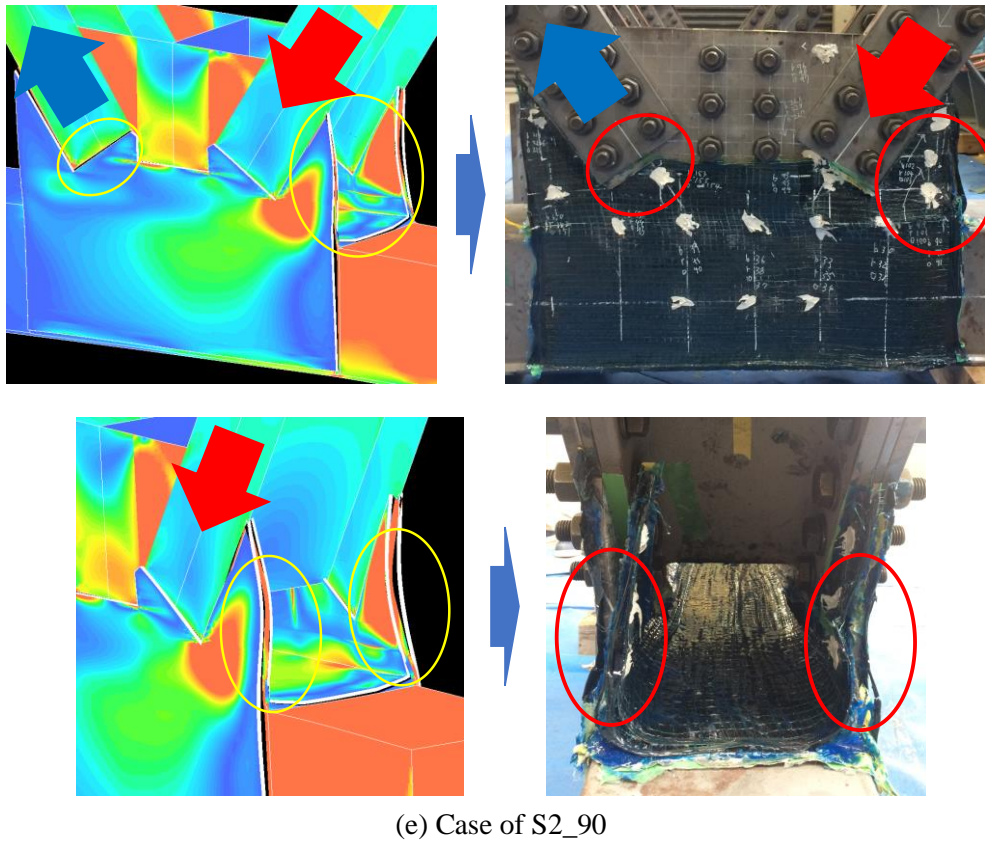


(c) Case of S1_56



(d) Case of S2_56

Fig. 4.21 Analytical contours of Von Mises stress and physical deformation of the corroded gusset plate connections bonding CFRP sheets.



(e) Case of S2_90

Fig. 4.21 Analytical contours of Von Mises stress and physical deformation of the corroded gusset plate connections bonding CFRP sheets.

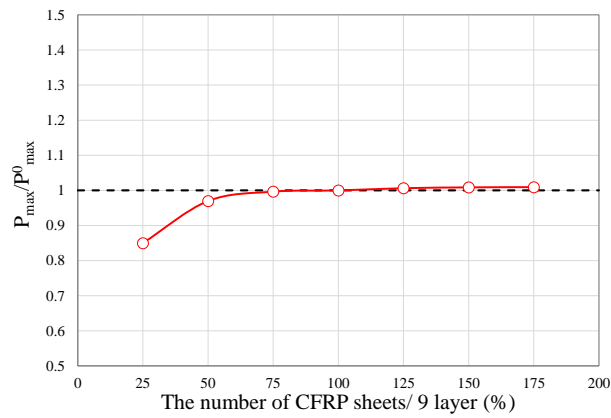


Fig. 4.22 Maximum load-the number of bonding CFRP sheets relationship.

4.3.3. Analysis results and discussion

The relationships between load and vertical displacement at the highest point of the tensile link member of the link frame in all of the repaired cases, are shown in **Fig. 4.20**. The black dashed lines (1634 kN) indicate the load-carrying capacity of intact Specimen N, obtained by loading test and described in Chapter 2. From the FEM analytical results, it is confirmed that the load-displacement curves begin to change due to the buckling of the plate area underneath the diagonal member; at the load of approximately 1100 kN in the cases of S1_45 and S2_45, and at the load of approximately 1200 kN in the cases of S1_56, S2_56, and S2_90.

These trends were consistent with the behavior obtained in the experiment. Furthermore, the experimental and analytical initial stiffness of the repaired gusset plate connections was almost in agreement. After overcoming the buckling load, the load-displacement curves diverged slightly from the experimental results.

The maximum load determined by analysis was 1459 kN for Specimen S1_45, 1490 kN for Specimen S2_45, 1327 kN for Specimen S1_56, 1532 kN for Specimen S2_56, and 1586 kN for Specimen S2_90. Based on this information, it can be observed that the difference in maximum load between -10% and -1%, indicating that the analytical model provides a high level of accuracy. The small differences observed can be mainly attributed to the influence of the mechanical properties of the polyurea putty layer, as clarified in many of the existing studies^{4.1), 4.25)-4.27)}. The comparisons described above confirm that the load-displacement curve and the maximum load provided by the analytical results agreed with those of the experiment results in all of the corroded gusset plate connections bonding CFRP sheets.

The overall shape of the gusset plate connections bonding is compared in **Fig. 4.21**: the deformation shown with the Von Mises distribution under the simulated contours was quite similar to the final shape of the experimental specimens after achieving maximum load. Specifically, the locations appeared the peeling failure were observed at the compressive free edges and the Groove section in tensile direction in cases of S1_45, and S2_45; at the compressive free edges and the area underneath the tensile diagonal member in case of S1_56, S2_56, and S2_90. As a result of these comparisons, the failure behavior of the corroded gusset plate connection bonding observed in the loading test can also clearly be accurately reproduced using an FEM analysis.

4.4. PARAMETRIC ANALYSIS

Once the FEM analysis had been confirmed as accurate by comparison with the experimental results, a parametric FEM analysis was conducted to investigate the relationship between the number of bonding CFRP sheets and the load-carrying capacity of the repaired gusset plate connection in the case of S2_90 (both-sides bonding, direction of CFRP sheets of 90 degrees). In this parametric analysis, the number of bonding CFRP sheets was varied from 25% to 175% of the number of CFRP sheets (9 layers) calculated by using Equation (4.1) of the steel conversion. This means that the number of CFRP sheets in the parametric analysis was changed from 3 layers to 16 layers.

$$E_{cf} \times t_{cf} \times n \geq E_s \times t_{sd} \quad (4.1)$$

where, E_{cf} is the elastic modulus of CFRP sheet; t_{cf} is the thickness of a CFRP sheet; n is the number of CFRP sheets; E_s is the elastic modulus of the steel; and t_{sd} is the required thickness of the cross-sectional loss part of the gusset plate.

The maximum loads, which are determined by using the parametric analysis of the change in the number of bonding CFRP sheets, are shown in **Fig. 4.22**, in which the vertical axis and horizontal axis depict P_{max}/P_{max}^0 and the number of bonding CFRP sheets (%), respectively. In this figure, P_{max} and P_{max}^0 are the maximum loads carried by the parametric analysis and the maximum load of case S2_90. As shown in **Fig. 4.22**, there is almost no change in the maximum load of the repaired gusset plate connection, when bonding over 75% of the calculated number of CFRP sheets. This is because when the number of bonding CFRP sheets is increased, the shear stress concentration at the top of the locations of bonding CFRP sheets is larger. Therefore, it is easy to occur the peeling failure in cases bonding so much of CFRP layers. As a result, for the safety, Equation (4.1) of the steel conversion is strongly preferred to determine the necessary number of CFRP sheets.

4.5. CONCLUSION

In short, this study proposed a nonlinear theoretical analysis method for a steel plate bonding a layer of CFRP sheet under uniaxial tensile loading, to determine the peeling strength and the mechanical behavior of adhesion layer. In this theoretical analysis, the peeling condition of CFRP sheet and the nonlinear material condition of all members on an analytical model were considered. Moreover, after the peeling mechanism of CFRP sheet was clarified clearly by the nonlinear theoretical analysis, finite element analyses were carried out on the repaired gusset plate connection to reproduce the load testing results obtained in Chapter3. In addition to the reproduced FEM analysis, a parametric analysis was implemented on the repaired gusset plate connection by varying the number of bonding CFRP sheets calculated from the equation of steel conversion, to clarify the necessary number of CFRP sheets bonding into the corroded gusset plate. The results obtained from this study are summarized as follows:

(1) Under the uniaxial-tensile-stress condition, it is possible to accurately evaluate the peeling strength and the mechanical behavior of adhesion layer, by proposing the nonlinear theoretical analysis.

(2) In order to reproduce the peeling failure of CFRP sheets under the environment of FEM analysis, the use

of the interface element is strongly preferred to simulate adhesion layer, in which the peeling failure occurs.

(3) By simulating the polyurea putty layer using the interface element, and CFRP sheets using the orthotropic material in models of FEM analysis; the load-carrying capacity, failure behavior, and deformation performance of the repaired gusset plate connection in the loading tests are reproduced.

(4) For the safety, the equation of the steel conversion is strongly preferred to determine the necessary number of CFRP sheets.

REFERENCES

- 4.1) Kamiharako, A., Shimomura, T., Maruyama, K., and Nishida, H.: Analysis of Bond and Debonding Behavior of Continuous Fiber Sheet Bonded on Concrete, *Journal of Japan Society of Civil Engineer (JSCE)*, No. 634/V-45, pp. 197-208, 1999.11 (in Japanese).
- 4.2) Miyashita, T., Nagai, M.: Stress Analysis for Steel Plate with Multilayered CFRP under Uni-axial Loading, *Journal of Japan Society of Civil Engineer (JSCE)*, Vol. 66, No. 2, pp. 378-392, 2010.6 (in Japanese).
- 4.3) Miyashita, T., Hidekuma, Y., Kobayashi, A., Okuyama, Y., Kudo, A., and Nagai, M.: Tensile Test of Steel Plate Bonded CFRP Strand Sheet with Joint, *Journal of Japan Society of Civil Engineer (JSCE)*, Vol. 69, No. 2, pp. 257-274, 2013 (in Japanese).
- 4.4) Sugiura, H., Kobayashi, A., Ohgaki, K., Inaba, N., Tomita Y., and Nagai, M.: Analytical Study on The Bonding Method of Carbon Fiber sSheets in The Repair of Corroded Steel Members, *Journal of Japan Society of Civil Engineer (JSCE)*, Vol. 64, No. 4, pp. 806-813, 2008 (in Japanese).
- 4.5) Ishikawa, T., Okura, I., and Komura, K.: Theoretical Analysis on Increase in Debonding Load by Stepping Ends of CFRP Strips, *Journal of Japan Society of Civil Engineer (JSCE)*, Vol. 64, No. 2, pp. 362-367, 2009 (in Japanese).
- 4.6) Ishikawa, T. Okura, I., Nishida, T., Yokota, S., and Saito, M.: Reduction of Debonding Shear Stress by Using a Low Elastic Modulus Adhesive Around The ends of CFRP Strips, *Journal of Structural Engineering*, Vol. 54A, pp. 842-849, 2008 (in Japanese).
- 4.7) Okuda, I., and Nagai, K.: Required Length and Debonding Shear Stress of Multiple CFRP Strips Bonded to steel Plate, *Journal of Japan Society of Civil Engineer (JSCE)*, Vol. 67, No. 1, pp. 72-85, 2011 (in Japanese).
- 4.8) Ishikawa, T., and Kitane, Y.: Required Length and Thickness of CFRP Plate for Bond Repair of Steel Plate with a Partial Loss of Cross-sectional Area, *Journal of Applied Mechanics*, Vol. 13, pp. 911-920, 2010 (in Japanese).
- 4.9) Ishikawa, T., and Okuda, I.: Theoretical Analysis of Debonding Behavior of CFRP Plates Adhered to Butted Steel Plates, *Journal of Structural Engineering*, Vol. 53A, pp. 1313-1320, 2007 (in Japanese).
- 4.10) Ishikawa, T., and Okuda, I.: Required Length and Optimum Stiffness of Multiple-Stepped CFRP Strips

- Bonded to Steel Plate, *Journal of Japan Society of Civil Engineer (JSCE)*, Vol. 66, No. 2, pp. 368-377, 2010.6 (in Japanese).
- 4.11) Ishikawa, T., and Miyashita, T.: Step Design for CFRP Bonded onto Steel Plate under Uni-axial Load, *Journal of Japan Society of Civil Engineer (JSCE)*, Vol. 67, No. 2, pp. 351-359, 2011 (in Japanese).
- 4.12) Ishikawa, T., Sasaki, Y., and Yamada, K.: Debonding strength of CFRP Strips Glued to Steel Plate Subjected to Bending, *Journal of Applied Mechanics*, Vol. 11, pp. 903-910, 2008 (in Japanese).
- 4.13) Okuda, I., Fukui, T., Nakamura, K., and Matsugami, T.: Decrease in Stress in Steel Plates by Carbon Fiber Sheets and Debonding Shearing Stress, *Journal of Japan Society of Civil Engineer (JSCE)*, No. 689/I-57, pp. 239-249, 2001 (in Japanese).
- 4.14) Sagawa, Y., Matsushita, H., and Takeo, K.: A Study on Bond Characteristics and Improvement of Ultimate Strength in Carbon Fiber Sheet Adhesion Method, *Journal of Japan Society of Civil Engineer (JSCE)*, No. 669/V-50, pp. 71-83, 2001. 2 (in Japanese).
- 4.15) Sato, Y., Kimura, K., and Kobatake, Y.: Bond Behavior Between CFRP Sheet and Concrete (Part 1), *Journal of Structural and Construction Engineering (Transactions of AIJ)*, Vol. 62, pp. 75-82, 1997.10 (in Japanese).
- 4.16) Sato, Y., Kimura, K., and Kobatake, Y.: Bond Behavior Between CFRP Sheet and Concrete (Part 1), *Journal of Structural and Construction Engineering (Transactions of AIJ)*, Vol. 63, pp. 75-82, 1997.10 (in Japanese).
- 4.17) Ishikawa, T.: The Current Situation and Issues of Repair and Strengthening of Steel Bridges by Bonding CFRP Strips, *Journal of The Adhesion Society of Japan*, Vol. 45, No. 4, pp. 139-144, 2009 (in Japanese).
- 4.18) Varastehpour, H. and Hamelin, P.: Strengthening of Concrete Beams Using Fiber-reinforced Plastics, *Material and Structural*, Vol.30, pp. 160-166, 1997.
- 4.19) Arduini, M., Di Tommaso, A., and Nanni, A.: Brittle Failure in FRP Plate and Sheet Bonded Beams, *ACI Structural Journal*, V. 94, No. 4, pp. 363-370, 1997.
- 4.20) E. Dehghani, F. Daneshjoo, A. Aghakouchak, N. Khaji, A new bond-slip model for adhesive in CFRP steel composite systems, *Eng. Struct.* 34 (2012) 447–454.
- 4.21) Jun He, Guijin Xian: Bond-slip behavior of fiber reinforced polymer strips-steel interface, *Journal of*

Construction and Building Materials, pp. 250-258, 2017.

- 4.22) X. Z. Lu, J. G. Teng, L. P. Ye, and J. J. Jiang: Intermediate Crack Debonding in FRP-Strengthened RC Beams: FE Analysis and Strength Model, *Journal of composites for construction*, pp. 161-174, 2007.
- 4.23) Rami A. Hawileh, Mohannad Z. Naser, Jamal A. Abdalla: Finite element simulation of reinforced concrete beams externally strengthened with short-length CFRP plates, *Composites Part B Engineering*, pp. 17722-17730, 2013.
- 4.24) Yasmeen Tableb Obaidat, Susanne Heyden, Ola Dahlblom: The effect of CFRP and CFRP/concrete interface models when modelling retrofitted RC beams with FEM, *Composite Structures*, pp. 1391-1398, 2010.
- 4.25) Takeda, K., Tanaka, K., Shimomura, T., and Ishida M.: Loading test and numerical simulation of the residual strength of post-tension PC bridge damaged by chloride attack, *Journal of Structural Engineering*, Vol. 63A, pp. 820-833, 2017 (in Japanese).
- 4.26) Kishi, N., Mikami, H., and Zhang, G.: Numerical analysis of debonding behavior of FRP sheet for flexural strengthening RC beams, *Journal of Japan Society of Civil Engineer (JSCE)*, Vol. 58, No. 725, pp. 255-272, 2003 (in Japanese).
- 4.27) Satoh, A., Sakagami, A., Mitarai, S., and Takeda, K.: Finite element analysis on pull-out behavior of post-installed adhesive anchor, *Cement Science and Concrete Technology*, Vol. 70, pp. 526-532 (in Japanese).

CHAPTER 5

DESIGN METHOD FOR CORRODED GUSSET PLATE CONNECTION

5.1. INTRODUCTION

The applicability of carbon fiber reinforced polymers (CFRP), in sheet form, as a material for repairing and strengthening corroded steel structures is being intensively investigated worldwide^{5.1)}, because of its light weight, high strength and superior durability. Numerous studies have already verified the effectiveness of using the CFRP sheets to reinforce the corroded members; specifically, the members subjected to axial stress such as the chord members of the truss bridge and the lower flange of I-girder steel bridges^{5.1), 5.2)}, and the members subjected to reaction force (compressive stress) such as the vertical stiffener at the supports of I-girder steel bridges^{5.1), 5.3)}. In addition, recovering from the shear buckling strength of the corroded web in steel girder bridges by using the CFRP sheets was also investigated^{5.1), 5.4)}. However, to the best of our knowledge, up to date there have been no cases in which CFRP sheets are applied for the corroded gusset plate connections. This chapter proposed a design method to repair the corroded gusset plate connection, after the effectiveness of the repair method using CFRP sheets were investigated by conducting loading tests and FEM analysis in Chapter 3 and Chapter 4.

Table 5.1 Material properties of CFRP sheets.

	Tensile strength (MPa)	Elastic modulus (GPa)	Fiber mass per unit area (g/mm ²)
High-strength	3400	245	200 ~ 600
Intermediate modulus	2900	390	300
	2400	450	
High modulus	1900	540	
		640	
Steel	400 ~ 570	200	—

Table 5.2 Primer quality standards.

Item	Standard value	Testing method
Tensile strength	29 N/mm ² or more	JIS K 7161
Tensile shear strength	9.8 N/mm ² or more	JIS K 6850
Steel bond strength	1.5 N/mm ² or more (23/50°C)	JIS A 6909
Glass transition temperature	70°C or more	JIS K 7121

Table 5.3 Smoothing agent quality standard.

Item	Standard value	Testing method
Tensile shear strength	9.8 N/mm ² or more	JIS K 6850
Steel bond strength	1.5 N/mm ² or more (23/50°C)	JIS A 6909
Compressive elastic modulus	1500 N/mm ²	JIS K 7181
Glass transition temperature	70°C or more	JIS K 7121

Table 5.4 Impregnation adhesive resin.

Item	Standard value	Testing method
Tensile strength	29 N/mm ² or more	JIS K 7161
Tensile shear strength	9.8 N/mm ² or more	JIS K 6850
Steel bond strength	1.5 N/mm ² or more (23/50°C)	JIS A 6909
CFRP tensile strength	1900 N/mm ² or more (23/50°C)	JIS A 1191
Glass transition temperature	70°C or more	JIS K 7121

Table 5.5 Primer for highly expansive elastic putty.

Item	Standard value	Testing method
Blend viscosity	Less than 2000 Pa·s	Type-B viscometer
Steel bond strength	1.5 N/mm ² or more (23/50°C)	JIS A 6909
Glass transition temperature	70°C or more	JIS K 7121

Table 5.6 Highly expansive elastic putty.

Item	Standard value	Testing method
Tensile strength	8 N/mm ² or more	JIS K 7161
Tensile elastic modulus	55 N/mm ² or more, less than 75 N/mm ²	JIS K 7161
Elongation	300% or more, less than 500%	JIS K 7161
Steel bond strength	1.5 N/mm ² or more (23/50°C)	JIS A 6909
Glass transition temperature	-15°C or more	JIS K 7121

5.2. DESIGN METHOD

5.2.1. Used materials^{5.1)}

This section described the mechanical properties of all materials used in the design method to repair corroded gusset plate connections, including carbon fiber reinforced polymers (CFRP) sheet, primer, smoothing agent, impregnation adhesive resin, primer for highly expansive elastic putty, and highly expansive elastic putty.

a) Carbon fiber reinforced polymers (CFRP) sheet

The Carbon fiber reinforced polymer (CFRP) sheets are classified on the aspects of strength, flexibility, and fiber mass per unit area, as shown in **Table 5.1**. In general, the carbon fiber sheets with high-strength are

widely used when the high tensile strength is required for the upgrades such as a seismic reinforcement of reinforced concrete piers. When the reduction of stress and/or deflection level under regular loads (without seismic force) is required, the number of layers could be minimized by using the high modulus carbon fiber.

The repair method proposed in this study is intended to improve the load-carrying capacity of the corroded gusset plate with cross-sectional loss by preventing local buckling and resisting the horizontal shear stress of the corroded section. It is confirmed by previous evaluation tests that using the high modulus CFRP sheet could reduce the number of layers, which becomes advantageous for the reduction of costs and duration of application; therefore, the high modulus CFRP sheet is specified as a standard fiber material in this study. The required value of elastic modulus is set to 640 GPa or more that is the highest among high modulus CFRP sheets to commercially available, and materials with this value were used for the past evaluation tests.

b) Primer

The primer is applied to the steel surface to secure sufficient bonding strength between steel members and CFRP sheets, creating a composite material. In the proposed repair method, epoxy resin is specified as a standard primer, its quality standards being based on the strengths of different primers used by past evaluation tests. Primer quality standards are shown in **Table 5.2**. When using other resins as an alternative primer, the quality of the resin should be confirmed by the necessary tests. Because the steel bonding strength depends on the secure adhesion of each interlayer (for example, between the primer and steel surface or smoothing agent), it should be examined after all necessary layers are applied, except for the protective layer and coating.

c) Smoothing agent

Flatten uneven or pitted areas by using the resin putty after the application of the primer, since flatness influences the bonding capability. Apply the resin putty. When covering a corner portion (inner curve), mold into an arch-like shape. Surface smoothing should be carried out after confirming the primer is dry to the touch. Material properties of smoothing agent quality standard is shown in **Table 5.3**.

d) Impregnation adhesive resin

The carbon fiber sheet could be well performed at a required strength and elastic modulus as a composite material (CFRP) consisting of carbon fiber and resin. The adhesive resin ensures its steel bonding strength, and tensile and joint strength as CFRP. The material properties of the impregnation adhesive resin are shown in **Table 5.4**.

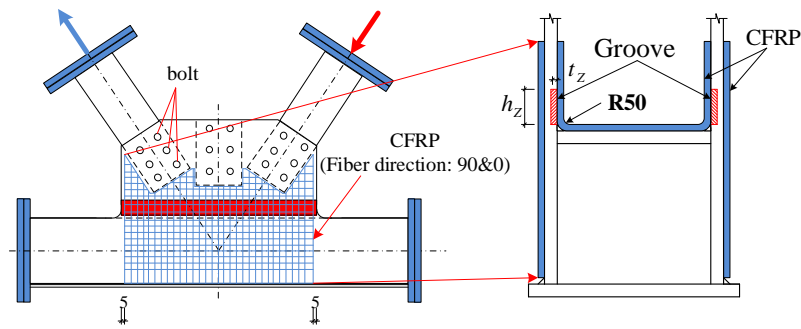


Fig. 5.1 Design method for corroded gusset plate connection.

e) Primer for highly expansive elastic putty

The primer for highly expansive elastic putty shall have capability to ensure the bonding between the putty and both of the steel and the smoothing agent with sufficient strength of bonding to both the steel and the smoothing agent to create composite structure. The material properties of primer for highly expansive elastic putty are shown in **Table 5.5**.

f) Highly expansive elastic putty

The highly expansive elastic putty is capable of bonding steel plate to CFRP in order to perform the required reinforcing effects without debonding, even if the steel plates are subjected to high stress or out-of-plane deformation due to local buckling. The material properties of highly expansive elastic putty are shown in **Table 5.6**.

5.2.2. Design method

This Section proposed a design method to repair the corroded gusset plate connection, after the effectiveness of the repair method using CFRP sheets were investigated by conducting loading tests and FEM analysis in Chapter 3 and Chapter 4 (see **Fig. 5.1**). Specifically, the direction of bonding CFRP sheets, the area of bonding CFRP sheets, and the location of bonding CFRP sheets are decided by using results obtained in Chapter 3. Furthermore, the necessary number of CFRP sheets is decided by using the results obtained in Chapter 3 and Chapter 4. The details of each item in the proposed repair method are expressed as the following:

- (1) The object gusset plate connection in the design method of this study is of the monolith-type, denoting that the projected web-plates of the lower chord member are employed as a gusset plate. The direction of bonding CFRP sheets is interwoven at an angle of 90 & 0 degrees compared to the axis of the lower chord members. This is understood that the method bonding CFRP sheets with the direction of 90 degrees achieved better effectiveness in resisting the horizontal shear stress of the corroded section, which decided

the final load-carrying capacity of the corroded gusset plate connection.

- (2) The necessary number of CFRP layers for each direction (in terms of compression and tension) is calculated such that the layers bonded to be thicker than the thickness reduced by the cross-sectional loss, which is calculated using the steel equivalent thickness of the CFRP sheet using Equation (5.1).

$$E_{cf} \times t_{cf} \times n \geq E_s \times t_{sd} \quad (5.1)$$

where, E_{cf} is the elastic modulus of CFRP sheet; t_{cf} is the thickness of a CFRP sheet; n is the necessary number of CFRP sheets; E_s is the elastic modulus of the steel; and t_{sd} is the required thickness of the cross-sectional loss part of the gusset plate.

- (3) The required thickness t_{sd} of the cross-sectional loss part for the repaired steel gusset plate should be larger than the thickness of the cross-sectional loss part due to corrosion. Moreover, the remaining thickness of the corroded gusset plate should satisfy the following conditions.

- The corroded gusset plate connection needs to be repaired if its remaining thickness is less than the value calculated based on the provisions of “Design Manual for Road Bridges II 13.3.2”^{5.5)}.
- Dead load which load acted on the steel member prior to the application of CFRP supported by the existing cross-section of the gusset plate.
- Live load and dead load which acts on the steel member after the application of CFRP supported by the composite cross-section of the gusset plate and CFRP sheets.

- (4) CFRP sheets are bonded to the outside and inside of the corroded gusset plate, with the same number of CFRP sheets. Inside of the gusset plate, CFRP sheets is connected continuously to the upper flange of the lower chord member by an R-shape (R50) (see **Fig. 5.1**).

- (5) The area bonding CFRP sheets to the gusset plate must be over 5 mm from the edge of the other members. Further, CFRP sheets must also be added to the locations around the diagonal members and the free edges of the gusset plate (see **Fig. 5.1**).

5.3. CONCLUSION

Based on the efficacy of the repair method using CFRP sheets by conducting loading tests and parametric FEM analysis (in Chapter 3 and Chapter 4), a design method is proposed to repair the corroded gusset plate connection. Additionally, the details and the mechanical properties of all the applied materials are described in the proposed design method.

REFERENCES

- 5.1) Nippon Expressway Research Institute: Manual to repair and reinforce steel structures using CFRP sheet, October 2013 (in Japanese).
- 5.2) Miyashita, T., Nagai M.: Stress analysis for steel plate with multilayered CFRP under uni-axial loading, *Journal of Japan Society of Civil Engineer (JSCE)*, Vol. 66, No. 2, pp.378-392, June 2010 (in Japanese).
- 5.3) Okuyama, Y., Miyashita, T., Ogata, T., Fujino, K., Ohgaki, K., Hidekuma, Y., Horimoto, W., Nagai, M.: Uniaxial compression test of steel plate bonded FRP sheet for rational repair and reinforcement of web in steel girder bridge, *Journal of Structural Engineering*, Vol. 57A, pp. 735-746, March 2011 (in Japanese).
- 5.4) Okuyama, Y., Miyashita, T., Wakabayashi, D., Koide, N., Kobayashi, A., Hidekuma, Y., Horimoto, W., Nagai, M.: Shear buckling test and prediction of shear load carrying capacity for steel girder bonded CFRP on its web, *Journal of Japan Society of Civil Engineer (JSCE)*, Vol. 68, No. 3, pp. 635-654, 2012 (in Japanese).
- 5.5) Japan Road Association: *Specification for highway bridges, Part-2 Steel Bridges*, Tokyo, Maruzen Publication, 2012 (in Japanese).
- 5.6) Ishikawa, T., Miyashita, T.: High-precision solution of steel plate strengthened with CFRP plates under uniaxial loading, *Journal of Japan Society of Civil Engineer (JSCE)*, Vol. 69, No. 1, pp. 89-100, 2013 (in Japanese).
- 5.7) Ishikawa, T., and Miyashita, T.: Step Design for CFRP Bonded onto Steel Plate under Uni-axial Load, *Journal of Japan Society of Civil Engineer (JSCE)*, Vol. 67, No. 2, pp. 351-359, 2011 (in Japanese).
- 5.8) Miyashita, T., Hidekuma, Y., Kobayashi, A., Okuyama, Y., Kudo, A., and Nagai, M.: Tensile Test of Steel Plate Bonded CFRP Strand Sheet with Joint, *Journal of Japan Society of Civil Engineer (JSCE)*, Vol. 69, No. 2, pp. 257-274, 2013 (in Japanese).
- 5.9) Okuyama, Y., Miyashita, T., Wakabayashi, D., Koide, N., Hidekuma, Y., Horimoto, W., Nagai, M.: Experimental study on repair method using CFRP for corroded web in steel girder bridge, *Journal of Structural Engineering*, Vol. 58A, pp. 710-720, 2012 (in Japanese).
- 5.10) Okuyama, Y., Miyashita, T., Wakabayashi, D., Koide, N., Hidekuma, Y., Horimoto, W., Nagai, M.: A study on optimum design method of repair and reinforcement method using carbon fiber sheets for

corroded web in steel girder bridge, *Journal of Structural Engineering*, Vol. 60A, pp. 541-553, 2014 (in Japanese).

- 5.11) Okuyama, Y., Miyashita, T., Wakabayashi, D., Koide, N., Hidekuma, Y., Horimoto, W., Nagai, M.: Uniaxial compression test of steel plate bonded FRP sheet for rational repair and reinforcement of web in steel girder bridge, *Journal of Structural Engineering*, Vol. 57A, pp. 735-746, 2011 (in Japanese).
- 5.12) Miyashita, T., Wakabayashi, D., Hidekuma, Y., Kobayashi, A., Koide, N., Horimoto, W., Nagai, M.: Repair for axial member in steel bridge by bonding CFRP sheet through high-elongation and low elastic putty, *Journal of Japan Society of Civil Engineer (JSCE)*, Vol. 71, No. 5, pp. 23-38, 2015 (in Japanese).
- 5.13) Wakabayashi, D., Miyashita, T., Okuyama, Y., Hidekuma, Y., Kobayashi, A., Koide, N., Horimoto, W., Nagai, M.: Repair method for steel girder by bonding carbon fiber sheet using high elongation elastic putty, *Journal of Japan Society of Civil Engineer (JSCE)*, Vol. 71, No. 1, pp. 44-63, 2015 (in Japanese).
- 5.14) Miyashita, T., Ishikawa, T.: Stress analysis for steel member multilayered CFRP plates under bending, *Journal of Japan Society of Civil Engineer (JSCE)*, Vol. 69, No. 1, pp. 26-39, 2013 (in Japanese).
- 5.15) Okuyama, Y., Miyashita, T., Wakabayashi, D., Koide, N., Kobayashi, A., Hidekuma, Y., Horimoto, W., Nagai, M.: Shear buckling test and prediction of shear load carrying capacity for steel girder bonded CFRP on its web, *Journal of Japan Society of Civil Engineer (JSCE)*, Vol. 68, No. 3, pp. 635-654, 2012 (in Japanese).

CHAPTER 6

CONCLUSION AND FURTHER RESEARCH

6.1. CONCLUSION

Numerous studies have shown that in steel truss bridges, corrosion is frequently found on the gusset plates which connect members, particularly where the plate connects to the upper flange of the lower chord member. The corrosion is simply caused due to the complex shapes in this region, which readily accumulate debris and water. The corrosion of gusset plate connections has been confirmed to decrease load-carrying capacity, and it can lead to the collapse of the entire bridge. Therefore, it has come to a critical subject of research to evaluate the remaining load-carrying capacity of gusset plate connections, accounting for the corroded section of the gusset plate. As a matter of fact, the attachment of stiffening plate and member replacement are some of the traditional methods which are often applied to repair corroded structures. However, these repair works lack efficacy because of the heavy machinery and welding facilities required. Therefore, a simple and effective repair method for the corroded gusset plate connection is urgently needed.

This study focuses on the following main objectives: 1) evaluating the remaining load-carrying capacity of the corroded gusset plate connection by using loading tests and FEM analyses; 2) establishing a proper repair method for the corroded gusset plate connection using CFRP sheets. The results obtained from this study are summarized as follows:

In chapter 2, loading tests performed in the laboratory and an FEM analysis were conducted on an existing bridge configuration using an approximately half-scale model. The gusset plate connections were tested in cases of 50% and 75% corrosion of the gusset plate thickness, and 50% corrosion of the length of the flange-to-gusset weld in compression. This study then conducted parametric FEM analyses by changing the size of the corroded sections to verify the relationship between the remaining load-carrying capacity and corrosion levels with the model of specimen and the full-scale model of an actual bridge. Additionally, based on the results of the parametric FEM analysis of the cases with the corrosion loss of the gusset plate thickness, an evaluation method for determining the local buckling strength of the corroded section was proposed. The primary results of this chapter could be summarized as follows.

- Based on the loading tests and FEM parametric analysis, as the dimensions of the corroded sections were increased, the load-carrying capacity of the gusset plate connection decreased. Specifically, for each cross-sectional corrosion height evaluated, the load-carrying capacity of the gusset plate connection exhibited nearly the same linear decrease with the increasing thickness of the cross-sectional corrosion of the section. Furthermore, the load-carrying capacity of the gusset plate connection was found to sharply drop when there was a change in the failure condition of the corroded section. Only a slight reduction in capacity, in the range of 5% to 7%, was found as the length of the flange-to-gusset weld corrosion increased from 50% to 100% of the gusset plate width.
- The parametric analysis results with the dimensions of the actual gusset plate connection indicated that the load-carrying capacity of corroded gusset plate connection on real bridges could be effectively determined, by using the remaining load-carrying capacity curves, normalized to the horizontal shear yield strength of the intact gusset plate. In addition, the failure behavior and the deformation performance of the actual gusset plate connection agreed completely with that of the gusset plate connection under the dimensions of the specimen.
- This study proposed an accurate method to evaluate the local buckling strength of cross-sectional corrosion section, and to determine the change in the failure condition of the corroded section (from local buckling to shear buckling).

In chapter 3, this study focused on investigating the effectiveness of repair method by using carbon fiber reinforced polymers (CFRP) for the corroded gusset plate connection. Loading tests were conducted with a model of approximately 50% the size of an actual bridge and the degree of corrosion assumed to be approximately 50% of the gusset plate thickness. Further, the loading tests were carried out with three parameters of the repair method including the area of the bonded CFRP sheets, the direction (± 45 , ± 56 , and 90 & 0 degrees) of the bonded CFRP sheets, and the location of the bonded CFRP sheets (out-side bonding and both-sides bonding). The primary results of this chapter could be summarized as follows.

- In the proposed repair method of CFRP sheets with the direction of 90 degrees, the load-carrying capacity of the corroded gusset plate connection recovered to that of the intact gusset plate connection. This is understood that the method bonding the CFRP sheets with the direction of 90 degrees achieved

a better effectiveness in resisting the horizontal shear stress of the corroded section, which decided the final load-carrying capacity of the corroded gusset plate connection, compared to other methods.

- The significant increase of the out-of-plane deformation of the corroded gusset plate was seen because the local buckling on the corroded section occurred. This is understood to be as a result of eccentricity, owing to the decreased thickness of the corroded section. However, by using the proposed repair methods, the out-of-plane deformation of the corroded gusset plate connection was prevented completely. Therefore, in all of the repaired cases, local buckling on the corroded section did not occur.
- For all of the proposed repaired methods, in the both-sides bonding methods, the bending moment in the compressive direction of the corroded section due to eccentricity was improved considerably compared to the out-side bonding methods.
- In the repair methods added the CFRP sheets to the area around the diagonal member of the gusset plate connection, the plate area underneath the diagonal member was reinforced by the CFRP sheets; therefore, the buckling load on this area grew up by 10%, compared to the other methods.

In chapter 4, this study established a nonlinear theoretical analysis method considering the peeling condition of CFRP sheet, and the nonlinear material condition of all member on the analytical model; for a steel plate bonding a layer of CFRP sheet under uniaxial tensile loading. Moreover, after grasping the peeling mechanism of CFRP sheet from the proposed nonlinear theoretical analysis, finite element analyses were implemented on the repaired gusset plate connection to reproduce the experimental results obtained in Chapter 3. Finally, a parametric analysis was carried out on the repaired gusset plate connection by varying the number of bonding CFRP sheets calculated from the equation of steel conversion, to clarify the necessary number of CFRP sheets bonding into the corroded gusset plate. The primary results of this chapter could be summarized as follows.

- In uniaxial-tensile-stress condition, it is possible to accurately evaluate the peeling strength and the mechanical behavior of adhesion layer, by developing the nonlinear theoretical analysis.
- In order to reproduce the peeling failure of CFRP sheets under the environment of FEM analysis, the use of the interface element is strongly preferred to simulate adhesion layer, in which the peeling failure occurred.
- By simulating the polyurea putty layer using the interface element, and CFRP sheets using the

orthotropic material in models of FEM analysis; the load-carrying capacity, failure behavior, and deformation performance of the repaired gusset plate connection in loading tests are reproduced

- For the safety, the equation of the steel conversion is strongly preferred to determine the necessary number of CFRP sheets in the repair method using CFRP sheets.

In chapter 5, this study proposed a design method to repair the corroded gusset plate connection, after the effectiveness of the repair method using CFRP sheets were investigated by conducting loading tests and FEM analysis in Chapter 3 and Chapter 4. The primary results of this chapter could be summarized as follows.

- The object gusset plate connection is monolithic with the chord member.
- The direction of bonding CFRP sheets is interwoven at an angle of 90 & 0 degrees compared to the axis of the lower chord members.
- The CFRP sheets are bonded to the outside and inside of the gusset plate, with the same number of CFRP sheets. Inside of gusset plate, CFRP sheets in connected continuously to the upper flange of the lower chord member by an R-shape (R50).
- The area bonding CFRP sheets into the gusset plate must be over 5 mm from the edge of the other members. Further, CFRP sheets must also add to the locations around the diagonal members and the free edges of the gusset plate.
- The equation is used to determine the number of CFRP sheets for each direction.

$$E_{cf} \times t_{cf} \times n \geq E_s \times t_{sd} \quad (6.1)$$

where, E_{cf} is the elastic modulus of CFRP sheet; t_{cf} is the thickness of a CFRP sheet; n is the necessary number of CFRP sheets; E_s is the elastic modulus of the steel; and t_{sd} is the thickness of the cross-sectional loss part of the steel.

- The required thickness t_{sd} of the cross-sectional loss part for the repaired steel gusset plate should be larger than the thickness of the cross-sectional loss part due to corrosion. Moreover, the remaining thickness of the corroded gusset plate should satisfy the following conditions.
 - + The corroded gusset plate connection needs to be repaired if its remaining thickness is less than the value calculated based on the provisions of “Design Manual for Road Bridges II 13.3.2”.
 - + Dead load which load acted on the steel member prior to the application of CFRP supported by

- the existing cross-section of the gusset plate.
- + Live load and dead load which acts on the steel member after the application of CFRP supported by the composite cross-section of the gusset plate and CFRP sheets.

6.2. FURTHER RESEARCH

This study attempts to address as many objectives related to the corroded gusset plate connection in steel truss bridges as possible. This study aims at consistently evaluating the remaining load-carrying capacity of the corroded gusset plate connection, and establishing a proper repair method for the corroded gusset plate connection. However, within the framework of this study, there are still some issues to be further investigated. Those are as the following:

In chapter 2 with the evaluation for the load-carrying capacity of the corroded gusset plate connection, the author recommends a need to clarify the remaining capacity of corroded gusset plate connection with the various shapes of connection and the various angle of diagonal member, and to investigate the influences of corroded gusset plate connection on the capacity of an entire bridge.

In chapter 3, investigating the effectiveness of repair method using CFRP sheets, the author recommends a need to conduct further parametric FEM analyses for the repair method bonding CFRP sheets with some parameters such as area bonding CFRP sheets, direction bonding CFRP sheets, and anchoring length of CFRP sheets.

In chapter 4, the nonlinear theoretical analysis, the author recommends a need to develop the nonlinear theoretical analysis method for the steel plate with multilayered CFRP sheets under uniaxial loading and bending; and the analytical object being able to fully consider the material model (shear direction and normal direction) of adhesion layer.

In chapter 5, the proposed design method repairing the corroded gusset plate connection, the author recommends a need to clarify the maximum thickness of the cross-sectional loss part due to corrosion, which can be repaired by using the proposed method. In other words, it will be necessary to investigate the maximum number of CFRP sheet can be bonded to the corroded gusset plate.

LIST OF PUBLICATIONS

Some parts of the results in this thesis have been published, presented, and submitted for publications and presentations in peer-reviewed international and domestic journals as well as conferences. Details of these publications are summarized as the following.

Peer Reviewed Journals:

- (1) Ngoc Vinh PHAM, Takeshi MIYASHITA, Kazuo OHGAKI, Yusuke OKUYAMA, Akira KOBAYASHI, Yuya HIDEKUMA, Takeshi HIROSE, and Takuya HARADA: Repair method using CFRP sheet for corroded gusset plate connection in truss bridges, *Journal of Japan Society of Civil Engineer (JSCE)*, Vol. 6, pp. 91-109, 2018.
- (2) Ngoc Vinh PHAM, Takeshi MIYASHITA, Kazuo OHGAKI, Yusuke OKUYAMA, Akira KOBAYASHI, Yuya HIDEKUMA, Takeshi HIROSE, and Takuya HARADA: Analytical study on remaining capacity of corroded gusset plate connection in truss bridges, *Journal of Japan Society of Civil Engineer (JSCE)*, Vol. 6, pp. 127-146, 2018.
- (3) Ngoc Vinh PHAM, Takeshi MIYASHITA: Nonlinear stress analysis for steel plate bonding CFRP sheet under uniaxial tensile loading. (In preparation).
- (4) Ngoc Vinh PHAM, Takeshi MIYASHITA: Remaining strength of corroded gusset plate connection and its repair method using CFRP sheet. (In preparation).
- (5) Ngoc Vinh PHAM, Takeshi MIYASHITA: Repair method and finite element analysis for corroded gusset plate connection bonding CFRP sheets. (In preparation).

Full Paper Peer Reviewed Proceedings

- (1) Ngoc Vinh PHAM, Takeshi MIYASHITA, Kazuo OHGAKI, Yusuke OKUYAMA, Akira KOBAYASHI, Yuya HIDEKUMA, Takeshi HIROSE, and Takuya HARADA: Study on repair method for corroded gusset plate connection by bonding CFRP sheet, *Proceedings of the 9th international conference on FRP composites in Civil Engineering (CICE2018)*, Paris, FRANCE, pp. 245-253, 2018.
- (2) Ngoc Vinh PHAM, Takeshi MIYASHITA, Kazuo OHGAKI, Yusuke OKUYAMA, Yuya HIDEKUMA, and Takuya HARADA: Effectiveness of Repair Method Bonding CFRP Sheet on Corroded Gusset Plate Connection, *Proceedings of 5th International Conference on Smart Monitoring, Assessment and*

Rehabilitation of Civil Structures (SMAR 2019), pp. 1-9, 2019.

- (3) Takeshi MIYASHITA, Ngoc Vinh PHAM, Kazuo OHGAKI, Yusuke OKUYAMA, Yuya HIDEKUMA, and Takuya HARADA: Experimental and Analytical Study on Remaining Capacity of Corroded Gusset Plate Connection, *Proceedings of 5th International Conference on Smart Monitoring, Assessment and Rehabilitation of Civil Structures (SMAR 2019)*, pp. 1-9, 2019.
- (4) Takeshi MIYASHITA, Ngoc Vinh PHAM, Kazuo OHGAKI, Yusuke OKUYAMA, Yuya HIDEKUMA, and Takuya HARADA: CFRP Sheet Repair for Corroded Truss Gusset Plate, *Proceedings of 2019 IABSE Congress New York City*, pp. 1-8, 2019.

Conference Papers

- (1) Ngoc Vinh PHAM, Takeshi MIYASHITA, Kazuo OHGAKI: Experimental Study on Repair Method Using CFRP for Corroded Gusset Connection in Truss Bridges, 土木学会、第 72 回年次学術講演会, I-533, 2017 年 9 月.
- (2) Ngoc Vinh PHAM, Takeshi MIYASHITA, Kazuo OHGAKI: Repair Method for Gusset Plate Connection with Cross-sectional Loss of Gusset Plate by CFRP bonding, 土木学会、第 35 回関東支部新潟会研究調査発表会, I-1316, 2017 年 11 月.
- (3) Ngoc Vinh PHAM, Takeshi MIYASHITA, Kazuo OHGAKI: Method Evaluating Local Buckling Strength of Gusset Plate Connection with Cross-sectional Corrosion Section, 土木学会、第 73 回年次学術講演会, I-557, 2018 年 8 月.
- (4) Ngoc Vinh PHAM, Takeshi MIYASHITA, Kazuo OHGAKI: Study Remaining Load-carrying Capacity of Corroded Gusset Plate Connection by FEM Analysis, 土木学会、第 73 回年次学術講演会, I-559, 2018 年 8 月.
- (5) Ngoc Vinh PHAM, Takeshi MIYASHITA, Kazuo OHGAKI: Nonlinear Stress Analysis Steel Plate Bonding CFRP Sheet Under Uniaxial Tensile Loading, 土木学会、第 74 回年次学術講演会, 2019 年 9 月.